Electrolyte Design for Next-Generation Electrochemical Capacitors with High Power and High Energy Densities

Yu Chikaoka

Department of Applied Chemistry,

Institute of Engineering,

Tokyo University of Agriculture and Technology

2020

Contents

Section 1. Introduction

1.1 General introduction

Owing to the growing concern for environmental issues, the demand for high-power energy storage devices for smart grids that are required for a sustainable society is increasing. Among such devices, electrochemical capacitors with high power, safety, and reliability have attracted significant research attention, and numerous studies have been conducted to improve their low-energy density.[1-2] Electrochemical capacitors have been developed and improved over three generations, with strategies focused on "increasing cell voltage" and "increasing cell capacity" for increasing energy density.[3-5] As shown in Fig. 1-1, electric double-layer capacitors (EDLCs),[6] hybrid capacitors,[7] and SuperRedox capacitors [5] have been investigated as the first, second, and third-generation capacitors, respectively.

EDLCs, the first-generation capacitors, are electric double-layer devices that use activated carbon (AC) at positive and negative electrodes and physical adsorption-desorption (non-Faraday reactions) for charging and discharging processes.[8] EDLCs are characterized by high power density, high stability, and high cyclability owing to their charge–discharge mechanism. The energy density of EDLCs is calculated by multiplying the stored charge and the square root of the working voltage.[1] The above working voltage, based on the electrochemical stability of the electrode/electrolyte interface, is limited to approximately 3.0 V at the AC electrode. Replacing an AC electrode with a single-walled carbon nanotube (SGCNT) for higher voltages allows stable operation at 3.3 V while its energy density rise is only approximately two-fold.[9]

The second-generation capacitor (hybrid capacitors) is a device in which one electrode of EDLCs are replaced by a high-capacity lithium ion-based battery material,

thus exceeding the limits of the EDLC's energy density.[10] Some devices, such as graphite-based and lithium titanate ($Li_4Ti_5O_{12}$)-based hybrid capacitors, are already in use for practical applications.[9, 11-12] These devices use electrode materials capable of rapid Faraday reactions to achieve high cycle and power density comparable to those of EDLCs, while realizing an energy density that is more than three times as large as that of EDLCs.

The third-generation SuperRedox capacitors (SRCs) consist of ultrafast positive- and negative- electrodes in which Faraday reaction kinetics are raised to the EDLCs level.[5, 13] The third-generation capacitor is constructed using electrode materials with 1) EDLCs-class power performance, 2) high cyclability and safety, and 3) high energy density. The electrode materials exhibiting a rapid Faraday reaction achieved by ultracentrifugation nanohybrid technology,[5, 14] such as $LiFePO_4$ (LFP) [15] and $Li_3V_2(PO_4)_3$ (LVP) [16], $Li_4Ti_5O_{12}$ (LTO) [7], TiO_2(B) [17], and Li_3VO_4 (LVO) [18], have been proposed as either negative electrode or positive electrode materials for SRCs. SRCs are expected to increase the energy density to be 5–6 times higher than that of EDLCs, and full-cell construction is preferred for practical applications.[5]

Among the second- and third-generation electrochemical capacitors, I focused on the devices with high reliability and high cyclability. Firstly, I focused on LTO//AC hybrid capacitors using LTO as the negative electrode, which is one of the second-generation hybrid capacitors used in practical applications. The present study aimed to improve the energy density of these capacitors by changing electrolyte composition by increasing the electrode thickness (Section 2) and the high voltage operation (Section 3). Furthermore, I focused on the third-generation capacitors (SRCs), LVO//LVP full cell with LVO for the negative electrode and LVP for the positive electrode and proposed a cell design guideline and an electrolyte composition for the prolonged cycle (Section 4).

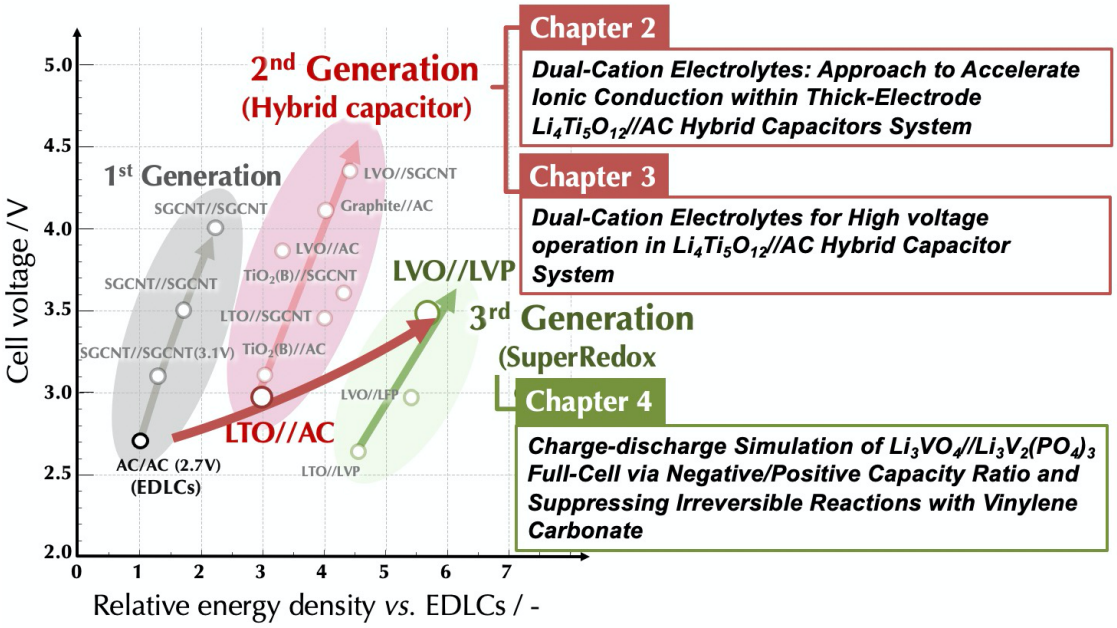

Fig. 1-1. Strategies for improving the energy density of electrical capacitors by increasing operating cell voltage and cell capacity.

1.2 Second-Generation Capacitors (Hybrid Capacitors)

Hybrid capacitors, in which one AC electrode is replaced by a high-power battery material, are expected to exhibit high power and energy density based on a combination reaction mechanism of physical adsorption (AC) and Faraday reaction (battery material).[10] Candidate negative electrode materials to be replaced include graphite, hard carbon, LTO, TiO_2(B), and LVO, while candidates for positive electrode materials are LFP and LVP.[5, 8, 19-20] Among these materials, a hybrid capacitor with graphite (Section 1.2.1) and LTO (Section 1.2.2) has been described in detail as a device with high cyclability.

1.2.1 Graphite negative electrode for hybrid capacitors (Lithium-ion capacitors)

The hybrid capacitor using graphite as the negative electrode has been widely investigated and is called as a lithium-ion capacitor (LIC).[12, 19, 21] Fig. 1-2 (a) shows the basic configuration and polarization diagram of LICs. The charge–discharge reaction equation of graphite is shown in equation (1-1).[22]

$$C_6 + xLi^+ + xe^- \rightleftarrows Li_xC_6 \qquad (1\text{-}1)$$

LICs have approximately three times the higher energy density than EDLCs owing to the use of graphite which has a high theoretical capacity (372 mAh g^{-1}) and a low reaction potential (0.2 V *vs.* Li/Li^+). A disadvantage of LICs is that the reaction potential is close to the lithium deposition potential (0 V *vs.* Li/Li^+), which may lead to lithium metal deposition and short circuit.[23] In addition, the formation of a solid electrolyte interface (SEI) occurs in the initial charge/discharge of the graphite negative electrode, which results in irreversible capacity.[24] Therefore, a process called lithium pre-doping is commonly used, which increases the manufacturing cost. Lithium pre-doping involves pre-charging of the negative electrode only to terminate or stabilize the side reactions related to SEI formation on the negative electrode side. Several methods for lithium pre-doping have been reported, such as the use of lithium metal,[25-26] transition metal oxides (Li_2MoO_3 and Li_2RuO_3),[27-28] and electrolyte additives (Li_2DHBN).[27]

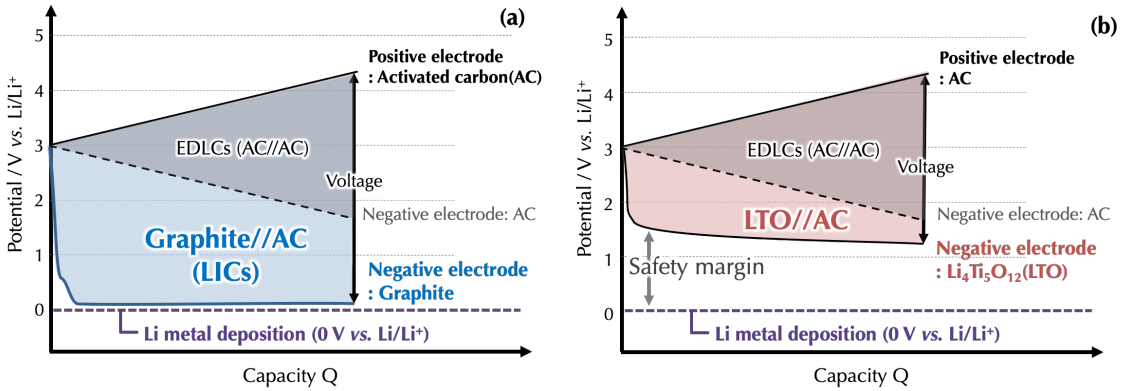

Fig. 1-2. Polarization diagram **(a)** Graphite//AC hybrid capacitor (positive electrode is AC and the negative electrode is graphite, LICs), **(b)** LTO//AC hybrid capacitor (positive electrode is AC and the negative electrode is LTO).

1.2.2 $Li_4Ti_5O_{12}$ (LTO) negative electrode for hybrid capacitors

As described in Section 1.2.1, a graphite-based hybrid capacitor has a high energy density, but its low reaction potential is close to the deposition potential of lithium metal, which results in the low safety and cyclability of the device. A hybrid capacitor with a $Li_4Ti_5O_{12}$ (LTO) negative electrode (LTO//AC Hybrid capacitor, Fig. 1-2 (b)) was developed for high-energy and high-power devices without compromising safety and cyclability. LTO has also been used in lithium-ion batteries for high safety and cyclability. Amatucci *et al.* firstly reported a hybrid capacitor using LTO for a negative electrode.[10] Although hybrid capacitors using TiO_2(B) [29] and $H_2Ti_{12}O_{25}$ [30] in the negative electrode have been reported, TiO_2(B) and $H_2Ti_{12}O_{25}$ do not have the same stability as LTO, and LTO is most suitable for use as a capacitor with high safety characteristics.

Spinel lithium titanate (LTO) with zero-strain characteristics was reported by Colbow *et al.* in 1989,[31] and its excellent charge–discharge behavior for lithium-ion battery material was reported by Ohzuku *et al.* in 1995.[32] The charge–discharge reaction of LTO is an intercalation reaction, and reaction equation can be expressed as follows:

$$Li_4Ti_5O_{12} + 3Li^+ + 3e^- \rightleftarrows Li_7Ti_5O_{12} \quad (1\text{-}2)$$

The reaction potential is 1.55 V *vs.* Li/Li^+, and the valence change in the oxidation state of Ti in this case is Ti^{4+} to Ti^{3+}. As shown in the reaction equation (1-2), not all Ti changes its valence; three Ti atoms become Ti^{3+} in the compositional formula $Li_4Ti_5O_{12}$, and the other two remain as Ti^{4+}, resulting in a theoretical capacity of 175 mAh g^{-1}. One of the main features is the very small volumetric change between $Li_4Ti_5O_{12}$ and $Li_7Ti_5O_{12}$ during the charge–discharge reaction. In general intercalation reactions, when lithium ions enter the active material, volume expansion occurs. For example, graphite is known to increase its volume by approximately 10%,[23] which can lead to device degradation. In contrast, LTO eliminates the distortion and reduces the overall volumetric change when lithium ions enter the material. Consequently, it exhibits a small volume change rate of 0.2%.[32]

The charge-discharge reaction potential of LTO (1.55 V *vs.* Li/Li^+) is higher than the general electrolyte decomposition potential (potential for SEI formation in graphite, ~ 1.0 V *vs.* Li/Li^+). Thus, LTO has attracted attention as an SEI-free electrode.[33] Without SEI formation owing to the side reaction, irreversible capacity disappears and stable charging/discharging is enabled, while resistance to lithium-ion diffusion by the SEI is eliminated. Furthermore, it can be used at a much higher potential than the potential for Li metal deposition (approximately 0 V *vs.* Li/Li^+). Accordingly, LTO is a suitable electrode material for high-safety devices with little risk of Li metal deposition even at high or low temperatures and high current operation.

1.2.3 Investigation of LTO//AC hybrid capacitors: toward higher energy density

As described in Section 1.2.2, the hybrid capacitor using LTO (LTO//AC) is a promising candidate for high-energy, high-power, long-lifetime, and high-safety devices.

However, the increasing energy density of LTO//AC hybrid capacitors is limited because of the higher reaction potential of LTO (1.55 V *vs.* Li/Li^+) compared to that of graphite (0.2 V *vs.* Li/Li^+). Several studies have addressed this challenge and focused on the doping of LTO,[34-35] the optimization of the LTO crystal structure,[36-37] optimization of surface area of AC,[37-38] and the use of pseudo capacitance,[39-40] which have been reported to increase energy density. Other strategies to increase the energy density of LTO//AC simply and effectively without changing the active material adjustment include increasing the electrode thickness and operating at high voltage (~ 3.2 V or higher). However, the former leads to a decrease in power performance owing to increased ionic resistance, while the latter leads to a decline in cyclability owing to electrolyte decomposition and H_2 gas generation. In this study, I investigated the optimization of the electrolyte design in LTO//AC hybrid capacitors to overcome the above challenges for high energy density. Section 2 discusses the improvement of the output performance by increasing the ionic conductivity, while Section 3 discusses the remedy of the cyclability at high-voltage operation by suppressing electrolyte decomposition.

1.3 Third-Generation Capacitors (SuperRedox Capacitors: SRCs)

SRCs, in which the EDLCs positive electrodes are replaced with fast battery materials, are expected to be high-power and high-energy-density devices using fast Faraday reaction as a reaction mechanism.[5, 13] The material requirements for SRCs are 1) high-power performance with EDLCs-class characteristics, 2) high cycle life and safety, and 3) high energy density. It is necessary to develop a synthetic method to fabricate nanoparticles of active electrode materials and a conductive agent to achieve these requirements. Among the above methods, Section 4 focuses on ultracentrifugation

technology (UC treatment)[13] and describes the materials prepared with a composite of active electrode materials and conductive agents groups *via* UC treatment. UC treatment enables the synthesis of metal oxide nanoparticles instantly in the presence of a nanocarbon matrix, and was applied to various intercalation materials such as LTO, TiO_2(B), and LVO as negative electrode materials and LFP and LVP as positive electrode materials.[5]

1.3.1 Negative electrode material for Super Redox capacitor

1.3.1.1 UC-treated $Li_4Ti_5O_{12}$ (LTO)

The UC-treated LTO has a composite morphology in which two-dimensional anisotropically controlled LTO nanocrystals are loaded in a uniform and highly dispersed state in a nanocarbon matrix with a highly specific surface area.[4] More specifically, the LTO and carbon nanotubes (CNTs) as conductive agents were synthesized by UC treatment as follows. 1) Unbundling of the strong bundle structure of CNTs is conducted in ultracentrifugal force field in a mixture of titanium source, lithium source, and CNTs. 2) The reaction between the titanium and lithium sources on the newly created CNT surface proceeds quickly, and LTO precursors are synthesized in situ on the CNT surface. 3) Finally, the precursors are sintered for a short time to produce LTO crystals with controlled crystal size and direction. Each of the LTO nanocrystals is directly bonded to the surface of the nanocarbons, and the unique crystal-composite morphology accelerates lithium de-insertion into the LTO, allowing for a charge/discharge rate in the range of 300–1200C (= 3–12 s). UC-treated LTO has been used as an LTO//AC hybrid capacitor, called "nano hybrid capacitor," which has demonstrated remarkable power and cyclability performance comparable to EDLCs.[11]

1.3.1.2 UC-treated Li_3VO_4 (LVO)

LVO negative electrodes have a lower reaction potential of less than 1 V (0.1–1.0 V *vs.* Li/Li^+) and a higher capacity of 394 mAh g^{-1} (equivalent to 2Li) than LTO negative electrodes (1.55 V and 175 mAh g^{-1}), leading to high energy densities.[41] The charge–discharge reaction of the LVO progresses as shown in equation (1-3), and a maximum of two lithium ions are available for insertion and deinsertion.

$$Li_{(3+x)}VO_4 \rightleftarrows Li_3VO_4 + xLi^+ + xe^- \ (0 \leq x \leq 2) \qquad (1\text{-}3)$$

According to the previous reports, LVO is limited in its output characteristics and energy consumption because of 1) low electrical conductivity (< 10^{-10} Ω^{-1} cm^{-1}) and 2) large charge–discharge potential hysteresis (< 500 mV).

In contrast, LVO nanoparticles with highly dispersed multi-walled carbon nanotube (MWCNT) prepared by UC treatment exhibited a reversible capacity of 330 mAh g^{-1} (2.5–0.1 V) per composite and reduced the hysteresis to 100 mV.[18] In addition, the capacity retention of over 50% (compared to 0.1 A g^{-1}) was achieved even at 20 A g^{-1} (50C per LVO, equivalent to 500C per AC). The long-term cycling characteristics of the LVO nanoparticles were observed in a cycle test (95% of the initial capacity was maintained after 1000 cycles). Moreover, in operand X-ray diffraction (XRD) and X-ray absorption fine structure analysis of LVO nanoparticles demonstrated an irreversible structural change (electrochemical activation) during the initial lithium insertion process. The electrochemical activation caused a shift in the charge–discharge mechanism of LVO from a "two-phase reaction" to a fast "solid solution reaction." By controlling the operating voltage after electrochemical activation (0.76–2.5 V *vs.* Li/Li^+), the potential hysteresis was reduced, and lithium insertion and deinsertion were accelerated. In this

study, I selected LVO as a suitable negative electrode material for SRCs.

1.3.2 Positive electrode material for Super Redox Capacitors

1.3.2.1 UC-treated $LiFePO_4$ (LFP)

Positive electrode materials for lithium-ion based batterie systems can be categorized as 1) layered rock-salt type, 2) spinel type, and 3) polyanion type.[42] The layered rock-salt type and spinel type are associated with the risk of ignition because of the release of oxygen from their crystal structures under abnormal conditions such as overcharging. In contrast, the polyanion type stabilizes the oxygen structure with strong AO_x bonds (A = B, P, and Si), which reduce the risk of oxygen release and provide superior safety. Among the polyanion-type materials, phosphoric acid-based positive electrode materials have a high reaction potential, making them attractive battery materials. Lithium iron phosphate ($LiFePO_4$: LFP) has a high capacity density (170 mAh g^{-1}), high crystal structure stability, and a reaction potential (~ 3.5 V *vs.* Li/Li^+) that prevents electrolyte decomposition. It is already in practical use as a positive electrode material for safety-oriented lithium batteries. The charge–discharge reaction equation of LFP is as follows:

$$LiFePO_4 \rightleftarrows FePO_4 + Li^+ + e^- \quad (1\text{-}4)$$

However, its low electrical conductivity (10^{-9}–10^{-11} Ω^{-1} cm^{-1}) and lithium-ion diffusion coefficient (10^{-13} cm^2 s^{-1}) hinders the use of high-speed charging and discharging.[43] In contrast, Naoi *et al.* prepared a composite UC-treated LFP in which 10–20 nm LFP nanoparticles were encapsulated in hollow carbon (30 nm) and achieved a high charge/discharge rate comparable to that of an AC electrode.[15]

1.3.2.2 UC-treated $Li_3V_2(PO_4)_3$ (LVP)

Among the candidates for polyanion-type positive electrode materials other than LFP, LVP has attracted attention as a high energy density material owing to its high reaction potential. LVP has a higher reaction potential (~ 4.3 V *vs.* Li/Li^+, two-electron reaction), electrical conductivity (10^{-7}–10^{-8} Ω^{-1} cm^{-1}), and lithium-ion diffusion coefficient (10^{-10} cm^2 s^{-1}) than those of LFP.[44-45] To achieve a very short charge/discharge time of 10 seconds comparable to EDLCs, LFP need to have a particle size of about 10 nm, whereas LVP have a sub-micron size of 600 nm.[46] Extremely small nanoparticles facilitate electrolyte decomposition during charging/discharging. Thus, LVP is an attractive positive electrode material that allows rapid charging/discharging without forming excessively small particles. LVP has high ionic diffusion properties similar to that of the sodium superionic conductor (NASICON) structure owing to the existence of wide diffusion paths in the *b*- and *c*-axes within the crystal. The theoretical capacity of LVP are 131 mAh g^{-1} for the two-electron reaction and 198 mAh g^{-1} for the three-electron reaction, and the charge–discharge reaction equation is as follows.

$$Li_3V_2(PO_4)_3 \leftrightarrows Li_{3-x}V_2(PO_4)_3 + xLi^+ + xe^- \quad (0 \le x \le 2) \quad (1\text{-}5)$$

Naoi *et al*. reported the formation of preferable connections between LVP, conductive agents, and the construction of ionic paths in the LVP composite electrodes by UC treatment.[16] The structure of the UC-treated LVP was examined by powder XRD and High-resolution transmission electron microscopy observations. The crystalline LVP with sizes in the range of 10–100 nm was highly dispersed in the nanocarbon without impurities. The capacity of this composite was more than twice as high as that of AC (96 mAh g^{-1}) at 300C (12 s discharge).

1.3.3 Cell design of Super Redox Capacitors: toward higher energy density

As achieving high voltage operation for high energy density, I selected Li_3VO_4 (LVO) as the negative electrode material, $Li_3V_2(PO_4)_3$ (LVP) as the positive electrode material, whose system is described as LVO//LVP full cells, among the high power and high cyclability materials as mentioned Section 1.3.2. However, LVO//LVP full cells have a potential problem of capacity decay because of the shift in the state of charge (SOC) balance. The SOC shift represents an imbalance between the positive electrode and the negative electrode and reduces the amount of available lithium for charge-discharge in a full cell, known as capacity decay phenomena in lithium-ion batteries.[47-48] The causes of the SOC shift are as follows: 1) the difference in coulombic efficiency between the positive- and negative- electrodes and 2) the degradation of the active material of the positive and negative electrodes and/or an increase in their resistance.[48] Capacity decay due to the SOC shift is an important factor for full-cell design, and it should be considered when establishing prolonged cyclability cell design. Although LVO and LVP have high cyclability in the half cell as mentioned in the Section 1.3.2, transition metal (vanadium) dissolution derived from the LVP positive electrode [49] can cause an imbalance between the positive and negative electrode coulombic efficiencies, leading to a SOC shift. The factors affecting the SOC shift of LVO//LVP full cells, the capacity ratio between negative and positive electrodes (N/P ratio) and the electrolyte composition (*e.g.*, electrolyte additives) have not been investigated, while those for graphite and silicon negative electrodes have been extensively examined.[50-53] It is necessary to 1) investigate the N/P ratio, 2) detecting degradation factor, and 3) determine an appropriate electrolyte composition to construct a highly stable LVO//LVP full cell with minimized SOC shifts.

1.4 Objectives

In this study, I optimized the electrolyte composition for second-generation LTO//AC hybrid capacitors (Section 2-3) and third-generation LVO//LVP SRCs (Section 4) to increase the energy density of energy storage devices with fast and stable cyclability such as EDLCs. In Section 2, I present an increase in energy density in the LTO//AC hybrid capacitors using 600-μm-thick electrodes by desinging of new electrolyte systems that exhibit high ionic conductivity. In this Section, dual-cation electrolytes, a conventional Li electrolyte mixed with quaternary ammonium salts and ionic liquids, have been demonstrated to enhance the power performance of the thick electrode (600 μm) LTO//AC hybrid capacitors. In Section 3, I present the improved cycle characteristics at high-voltage operation above 3.2 V to achieve high energy density in LTO//AC hybrid capacitors in terms of the electrolyte. In particular, for high-voltage operation, H_2 gas generation was a problem due to catalytic reductive decomposition of a solvent such as propylene carbonate (PC) and H_2O at the Lewis acid sites LTO surface.; this problem is remedied by passivating the LTO surface by the Lewis-based layer derived from additional supporting electrolytes, as introduced in Section 3. As discussed in Section 4, the cell design for the prolonged cyclability of LVO//LVP SRCs was investigated in terms of the N/P ratio and electrolyte additives. Furthermore, the degradation behavior of LVO and LVP negative electrodes was analyzed in detail by charge–discharge simulations to identify cycle degradation factors.

1.5 References

1. Simon, P.; Gogotsi, Y., Materials for electrochemical capacitors. *Nanoscience and technology: a collection of reviews from Nature journals* **2010**, 320-329.

2. Wang, Y.; Song, Y.; Xia, Y., Electrochemical capacitors: mechanism, materials, systems, characterization and applications. *Chemical Society Reviews* **2016,** *45* (21), 5925-5950.

3. Salanne, M.; Rotenberg, B.; Naoi, K.; Kaneko, K.; Taberna, P.-L.; Grey, C. P.; Dunn, B.; Simon, P., Efficient storage mechanisms for building better supercapacitors. *Nature Energy* **2016,** *1* (6), 1-10.

4. Naoi, K.; Ishimoto, S.; Miyamoto, J.-i.; Naoi, W., Second generation 'nanohybrid supercapacitor': evolution of capacitive energy storage devices. *Energy & Environmental Science* **2012,** *5* (11), 9363-9373.

5. Okita, N.; Iwama, E.; Naoi, K., Recent Advances in Supercapacitors: Ultrafast Materials Make Innovations. *Electrochemistry* **2020**, 20-H6301.

6. Simon, P.; Gogotsi, Y., Materials for electrochemical capacitors. *Nature Materials* **2008,** *7* (11), 845-854.

7. Naoi, K.; Ishimoto, S.; Isobe, Y.; Aoyagi, S., High-rate nano-crystalline $Li_4Ti_5O_{12}$ attached on carbon nano-fibers for hybrid supercapacitors. *Journal of Power Sources* **2010,** *195* (18), 6250-6254.

8. Kötz, R.; Carlen, M., Principles and applications of electrochemical capacitors. *Electrochimica Acta* **2000,** *45* (15-16), 2483-2498.

9. Kenji, T.; Satoru, T.; Shuzo, S.; Syuichi, I. In *Approach for Advanced Capacitors in Nippon Chemi-Con*, Abstract of 2016 International Conference on Advanced Capacitors, KL-09, 2016.

10. Amatucci, G. G.; Badway, F.; Du Pasquier, A.; Zheng, T., An asymmetric hybrid nonaqueous energy storage cell. *Journal of The Electrochemical Society* **2001,** *148* (8), A930-A939.

11. Naoi, K.; Naoi, W.; Aoyagi, S.; Miyamoto, J.-i.; Kamino, T., New generation "nanohybrid supercapacitor". *Accounts of chemical research* **2013,** *46* (5), 1075-1083.

12. Ronsmans, J.; Lalande, B. In *Combining energy with power: Lithium-ion capacitors*, 2015 International Conference on Electrical Systems for Aircraft, Railway, Ship Propulsion and Road Vehicles (ESARS), IEEE: 2015; pp 1-4.

13. Naoi, K., 'Nanohybrid capacitor': the next generation electrochemical capacitors. *Fuel cells* **2010,** *10* (5), 825-833.

14. Iwama, E.; Simon, P.; Naoi, K., Ultracentrifugation: An effective novel route to ultrafast nanomaterials for hybrid supercapacitors. *Current Opinion in Electrochemistry* **2017,** *6* (1), 120-126.

15. Naoi, K.; Kisu, K.; Iwama, E.; Nakashima, S.; Sakai, Y.; Orikasa, Y.; Leone, P.; Dupré, N.; Brousse, T.; Rozier, P., Ultrafast charge–discharge characteristics of a

nanosized core–shell structured $LiFePO_4$ material for hybrid supercapacitor applications. *Energy & Environmental Science* **2016,** *9* (6), 2143-2151.

16. Naoi, K.; Kisu, K.; Iwama, E.; Sato, Y.; Shinoda, M.; Okita, N.; Naoi, W., Ultrafast cathode characteristics of nanocrystalline-$Li_3V_2(PO_4)_3$/carbon nanofiber composites. *Journal of The Electrochemical Society* **2015,** *162* (6), A827.

17. Naoi, K.; Kurita, T.; Abe, M.; Furuhashi, T.; Abe, Y.; Okazaki, K.; Miyamoto, J.; Iwama, E.; Aoyagi, S.; Naoi, W., Ultrafast nanocrystalline-TiO_2(B)/carbon nanotube hyperdispersion prepared *via* combined ultracentrifugation and hydrothermal treatments for hybrid supercapacitors. *Advanced Materials* **2016,** *28* (31), 6751-6757.

18. Iwama, E.; Kawabata, N.; Nishio, N.; Kisu, K.; Miyamoto, J.; Naoi, W.; Rozier, P.; Simon, P.; Naoi, K., Enhanced electrochemical performance of ultracentrifugation-derived nc-Li_3VO_4/MWCNT composites for hybrid supercapacitors. *ACS nano* **2016,** *10* (5), 5398-5404.

19. Sivakkumar, S. R.; Nerkar, J.; Pandolfo, A., Rate capability of graphite materials as negative electrodes in lithium-ion capacitors. *Electrochimica Acta* **2010,** *55* (9), 3330-3335.

20. Cericola, D.; Kötz, R., Hybridization of rechargeable batteries and electrochemical capacitors: Principles and limits. *Electrochimica Acta* **2012,** *72*, 1-17.

21. Sivakkumar, S. R.; Pandolfo, A., Evaluation of lithium-ion capacitors assembled with pre-lithiated graphite anode and activated carbon cathode. *Electrochimica Acta* **2012,** *65*, 280-287.

22. Wang, C.; Wu, G.; Li, W., Lithium insertion in ball-milled graphite. *Journal of Power Sources* **1998,** *76* (1), 1-10.

23. Winter, M.; Besenhard, J. O.; Spahr, M. E.; Novak, P., Insertion electrode materials for rechargeable lithium batteries. *Advanced Materials* **1998,** *10* (10), 725-763.

24. Peled, E., Film forming reaction at the lithium/electrolyte interface. *Journal of Power Sources* **1983,** *9* (3), 253-266.

25. Yan, J.; Cao, W.; Zheng, J., Constructing high energy and power densities li-ion capacitors using Li thin film for pre-lithiation. *Journal of The Electrochemical Society* **2017,** *164* (9), A2164.

26. Yao, K.; Cao, W.; Liang, R.; Zheng, J., Influence of stabilized lithium metal powder loadings on negative electrode to cycle life of advanced lithium-ion capacitors. *Journal of The Electrochemical Society* **2017,** *164* (7), A1480.

27. Jeżowski, P.; Crosnier, O.; Deunf, E.; Poizot, P.; Béguin, F.; Brousse, T., Safe and recyclable lithium-ion capacitors using sacrificial organic lithium salt. *Nature Materials* **2018,** *17* (2), 167-173.

28. Park, M.-S.; Lim, Y.-G.; Park, J.-W.; Kim, J.-S.; Lee, J.-W.; Kim, J. H.; Dou, S. X.; Kim, Y.-J., Li_2RuO_3 as an additive for high-energy lithium-ion capacitors. *The Journal of Physical Chemistry C* **2013,** *117* (22), 11471-11478.
29. Aravindan, V.; Shubha, N.; Ling, W. C.; Madhavi, S., Constructing high energy density non-aqueous Li-ion capacitors using monoclinic TiO_2-B nanorods as insertion host. *Journal of Materials Chemistry A* **2013,** *1* (20), 6145-6151.
30. Lee, S.-H.; Kim, H.-K.; Lee, J. H.; Lee, S.-G.; Lee, Y.-H., Fabrication and electrochemical properties of cylindrical hybrid supercapacitor using $H_2Ti_{12}O_{25}$ as anode material. *Materials Letters* **2015,** *143*, 101-104.
31. Colbow, K.; Dahn, J.; Haering, R., Structure and electrochemistry of the spinel oxides $LiTi_2O_4$ and $Li_{4/3}Ti_{5/3}O_4$. *Journal of Power Sources* **1989,** *26* (3-4), 397-402.
32. Ohzuku, T.; Ueda, A.; Yamamoto, N., Zero - strain insertion material of Li $[Li_{1/3}Ti_{5/3}]O_4$ for rechargeable lithium cells. *Journal of The Electrochemical Society* **1995,** *142* (5), 1431.
33. Kang, E.; Jung, Y. S.; Kim, G. H.; Chun, J.; Wiesner, U.; Dillon, A. C.; Kim, J. K.; Lee, J., Highly improved rate capability for a lithium - ion battery nano - $Li_4Ti_5O_{12}$ negative electrode *via* carbon - coated mesoporous uniform pores with a simple self - assembly method. *Advanced Functional Materials* **2011,** *21* (22), 4349-4357.
34. Lee, B.; Yoon, J., Preparation and characteristics of $Li_4Ti_5O_{12}$ with various dopants as anode electrode for hybrid supercapacitor. *Current Applied Physics* **2013,** *13* (7), 1350-1353.
35. Lee, S.-H.; Kim, H.-K.; Yun, Y.-S.; Yoon, J. R.; Lee, S.-G.; Lee, Y.-H., A novel high-performance cylindrical hybrid supercapacitor with $Li_{4-x}Na_xTi_5O_{12}$/activated carbon electrodes. *International journal of hydrogen energy* **2014,** *39* (29), 16569-16575.
36. Deng, S.; Li, J.; Sun, S.; Wang, H.; Liu, J.; Yan, H., Synthesis and electrochemical properties of $Li_4Ti_5O_{12}$ spheres and its application for hybrid supercapacitors. *Electrochimica Acta* **2014,** *146*, 37-43.
37. Jain, A.; Aravindan, V.; Jayaraman, S.; Kumar, P. S.; Balasubramanian, R.; Ramakrishna, S.; Madhavi, S.; Srinivasan, M., Activated carbons derived from coconut shells as high energy density cathode material for Li-ion capacitors. *Scientific reports* **2013,** *3* (1), 1-6.
38. Puthusseri, D.; Aravindan, V.; Anothumakkool, B.; Kurungot, S.; Madhavi, S.; Ogale, S., From Waste Paper Basket to Solid State and Li - HEC Ultracapacitor Electrodes: A Value Added Journey for Shredded Office Paper. *Small* **2014,** *10* (21), 4395-4402.

39. Hu, X.; Deng, Z.; Suo, J.; Pan, Z., A high rate, high capacity and long life ($LiMn_2O_4$+ AC)/$Li_4Ti_5O_{12}$ hybrid battery–supercapacitor. *Journal of Power Sources* **2009,** *187* (2), 635-639.

40. Chen, S.; Hu, H.; Wang, C.; Wang, G.; Yin, J.; Cao, D., ($LiFePO_4$-AC)/$Li_4Ti_5O_{12}$ hybrid supercapacitor: The effect of $LiFePO_4$ content on its performance. *Journal of Renewable and Sustainable Energy* **2012,** *4* (3), 033114.

41. Li, H.; Liu, X.; Zhai, T.; Li, D.; Zhou, H., Li_3VO_4: a promising insertion anode material for lithium‐ion batteries. *Advanced Energy Materials* **2013,** *3* (4), 428-432.

42. Masquelier, C.; Croguennec, L., Polyanionic (phosphates, silicates, sulfates) frameworks as electrode materials for rechargeable Li (or Na) batteries. *Chemical reviews* **2013,** *113* (8), 6552-6591.

43. Chung, S.-Y.; Bloking, J. T.; Chiang, Y.-M., Electronically conductive phospho-olivines as lithium storage electrodes. *Nature Materials* **2002,** *1* (2), 123-128.

44. Qiao, Y.; Tu, J.; Wang, X.; Zhang, D.; Xiang, J.; Mai, Y.; Gu, C., Synthesis and improved electrochemical performances of porous $Li_3V_2(PO_4)_3$/C spheres as cathode material for lithium-ion batteries. *Journal of Power Sources* **2011,** *196* (18), 7715-7720.

45. Yamada, A.; Chung, S.-C., Crystal Chemistry of the Olivine-Type Li (Mn_yFe_{1-y})PO_4 and (Mn_yFe_{1-y})PO_4 as Possible 4 V Cathode Materials for Lithium Batteries. *Journal of The Electrochemical Society* **2001,** *148* (8), A960.

46. Morgan, D.; Ceder, G.; Saidi, M.; Barker, J.; Swoyer, J.; Huang, A. H.; Adamson, G., Experimental and Computational Study of the Structure and Electrochemical Properties of $Li_xM_2(PO_4)_3$ Compounds with the Monoclinic and Rhombohedral Structure. *Chemistry of Materials* **2002,** *14*, 4684-4693.

47. Christensen, J.; Newman, J., Cyclable lithium and capacity loss in Li-ion cells. *Journal of The Electrochemical Society* **2005,** *152* (4), A818.

48. Birkl, C. R.; Roberts, M. R.; McTurk, E.; Bruce, P. G.; Howey, D. A., Degradation diagnostics for lithium ion cells. *Journal of Power Sources* **2017,** *341*, 373-386.

49. Okita, N.; Iwama, E.; Tatsumi, S.; VÕ, T. N. H.; Naoi, W.; Reid, M. T. H.; Naoi, K., Prolonged Cycle Life for $Li_4Ti_5O_{12}$//[Li_3V_2 $(PO_4)_3$/Multiwalled Carbon Nanotubes] Full Cell Configuration *via* Electrochemical Preconditioning. *Electrochemistry* **2019,** *87* (3), 148-155.

50. Abe, Y.; Kumagai, S., Effect of negative/positive capacity ratio on the rate and cycling performances of $LiFePO_4$/graphite lithium-ion batteries. *Journal of Energy Storage* **2018,** *19*, 96-102.

51. Chen, Z.; Zhang, L.; Wu, X.; Song, K.; Ren, B.; Li, T.; Zhang, S., Effect of N/P ratios on the performance of $LiNi_{0.8}Co_{0.15}Al_{0.05}O_2$|| SiO_x/Graphite lithium-ion batteries. *Journal of Power Sources* **2019,** *439*, 227056.
52. Chen, L.; Wang, K.; Xie, X.; Xie, J., Effect of vinylene carbonate (VC) as electrolyte additive on electrochemical performance of Si film anode for lithium ion batteries. *Journal of Power Sources* **2007,** *174* (2), 538-543.
53. Jung, R.; Metzger, M.; Haering, D.; Solchenbach, S.; Marino, C.; Tsiouvaras, N.; Stinner, C.; Gasteiger, H. A., Consumption of fluoroethylene carbonate (FEC) on Si-C composite electrodes for Li-ion batteries. *Journal of The Electrochemical Society* **2016,** *163* (8), A1705.

Section 2. Dual-Cation Electrolytes: Approach to Accelerate Ionic Conduction within Thick-Electrode $Li_4Ti_5O_{12}$//AC Hybrid Capacitors System

2.1 Introduction

High-output/high-energy-density storage devices help to reduce CO_2 emissions with their applications in renewable energy storage. Electric double-layer capacitors (EDLCs) that consist of two activated carbon (AC) electrodes are promising high-power energy storage devices; however, there is scope for improving their low energy density.[1-2] Several studies have focused on enhancing the energy density of EDLCs by replacing the AC electrode with a lithium-ion battery-based (LIB-based) material.[1, 3-9] Among such hybrid capacitors, LTO//AC systems that consist of $Li_4Ti_5O_{12}$ (LTO, negative) and AC (positive) electrodes have attracted significant attention because of the high theoretical capacity (175 mAh g^{-1}), low volumetric expansion (0.2%), and high reaction potential of LTO (1.55 V *vs.* Li/Li^+, where electrolyte decomposition does not occur).[10-11] The use of thicker electrodes (> 200 μm) is a simple and effective approach to further increase the energy density in hybrid capacitor systems without changing the active material. In thick-electrode systems, the electrolyte composition plays an important role because of the high ionic resistance of thick electrodes owing to the presence of macropores, which is a limitation with respect to high-power applications.[12-13] The use of an electrolyte with high ionic conductivity is a traditional and effective approach to reduce ionic resistance. Although conventional $LiPF_6$-based electrolytes have a relatively high ionic conductivity (~ 6.0 mS cm^{-1}),[14] they are not suitable for use in LTO//AC hybrid capacitor systems because of the combination of the moisture-sensitive PF_6 anion and AC, which has high

water adsorption. Therefore, lithium tetrafluoroborate ($LiBF_4$) has been extensively employed in LTO//AC systems because of its adequate water resistance;[4, 11, 15] however, $LiBF_4$-based electrolytes exhibit a lower ionic conductivity (~ 3.4 mS cm^{-1}) than those of $LiPF_6$-based electrolytes. In the previous study, "dual-cation" electrolytes have been designed for use in LTO//AC thick-electrode hybrid capacitor systems to overcome this problem.[16] The dual-cation electrolyte consists of $LiBF_4$ and a spiro-(1,1')-bipyrrolidinium tetrafluoroborate ($SBPBF_4$) as additional supporting electrolytic salt dissolved in propylene carbonate (PC). The SBP-based dual-cation electrolyte [(1 M $LiBF_4$ + 2 M $SBPBF_4$)/PC] exhibits a higher ionic conductivity (7.7 mS cm^{-1}) than that of single-cation electrolytes (3.4 mS cm^{-1} for 1 M $LiBF_4$/PC), resulting in an improved power density of LTO//AC (Fig. 2-1).

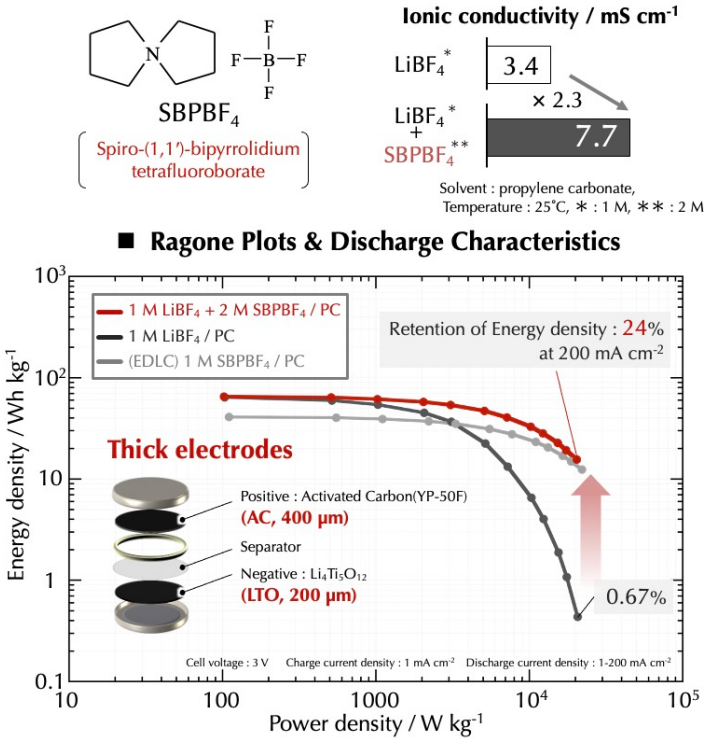

Fig. 2-1. Dual-cation electrolytes for LTO//AC hybrid capacitors.[16]

To further improve the ionic conductivity and power density of LTO//AC, new dual-cation electrolytes have been developed using various electrolytic salts other than $SBPBF_4$. The following characteristics are expected in supporting electrolytic salts: i) high solubility and high ionic conductivity, ii) high electrochemical stability (a wide electrochemical window), and iii) high durability against water, for example, with BF_4 as a counter anion. Therefore, 1-ethyl-3-methylimidazolium tetrafluoroborate ($EMIBF_4$), an aprotic ionic liquid, was selected as a replacement for $SBPBF_4$ in dual-cation electrolytes. $EMIBF_4$ exhibits high ionic conductivity, wide electrochemical window, and low vapor pressure, which facilitates its tremendous potential for EDLC- and LIB-based applications.[17] Given the excellent compatibility between $EMIBF_4$ and PC, the maximum molar concentration of $EMIBF_4$ in PC (~ 6.5 M) is higher than that of $SBPBF_4$ (~ 3.3 M).[17-18] Indeed, the addition of $EMIBF_4$ (> 3 M) facilitates an increase in the ionic conductivity of a 1 M $LiBF_4$/ PC electrolyte (~ 10 mS cm^{-1}) [19] compared to that of $SBPBF_4$ (~ 8 mS cm^{-1}).[16]

The present study reveals the superiority of the EMI-based dual-cation electrolyte in terms of the power performance of the resulting LTO//AC thick-electrode systems, compared to those based on $SBPBF_4$ and other quaternary ammonium salts such as triethylmethylammonium tetrafluoroborate ($TEMABF_4$) and tetraethylammonium tetrafluoroborate ($TEABF_4$). The factors contributing to the improved output characteristics were investigated in detail by dividing the reaction process into bulk electrolyte, ion transport within the electrode, and electrode/electrolyte interface reactions, and analyzing the substance transport parameters (Fig. 2-2). The electrochemical measurements and physicochemical analyses were combined to simulate the distribution of charge transfer resistance (R_{ct}) in the LTO macropores using the transmission-line

model (TLM), which was employed to elucidate the factors necessary for improving the discharge characteristics of EMI-based dual-cation electrolytes. Additionally, the importance of the balance between the total ionic conductivity of the electrolyte and individual Li^+ conductivity (σ_{Li+}) on the power performance of the LTO//AC thick-electrode was revealed. Therefore, these results and analyses provided new guidelines for effectively customizing dual-cation electrolyte compositions.

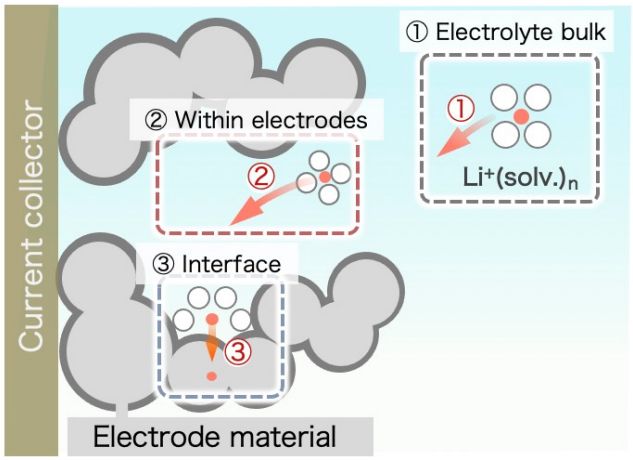

Fig. 2-2. Schematic diagram of analysis for elucidating the mechanism.

2.2 Experiments

2.2.1 Preparation of electrolytes

$LiBF_4$ (Morita Chemical Industries, Japan), $SBPBF_4$ (Carlit Holdings, Japan), $EMIBF_4$ (Kishida Chemicals, Japan), $TEMABF_4$ (Kishida Chemicals, Japan), and $TEABF_4$ (Kishida Chemicals, Japan) were used as supporting electrolytes. All electrolytic salts were dissolved in PC (Kishida Chemicals, Japan; moisture content < 20 ppm) in an Ar-filled glove box (Unico, dew point < −70 °C). The water content of the prepared electrolytes was maintained below 20 ppm using molecular sieves (5A, TOSOH, Japan).

2.2.2 Physicochemical properties of electrolytes

The ionic conductivities of the prepared electrolytes were measured at room temperature (T = 25 °C) using a conductivity meter (Mettler Toledo, S230) equipped with a 4-electrode Pt conductivity sensor (Mettler Toledo, InLab 710). The viscosities of the electrolytes were measured using a digital viscometer (Brookfield, DV-II+Pro) at T = 25 °C.

2.2.3 Self-diffusion coefficients and Raman spectra of electrolytes

Pulsed gradient spin-echo nuclear magnetic resonance (PGSE-NMR) was employed to measure the self-diffusion coefficients of all investigated ions (Li^+, SBP^+, EMI^+, and BF_4^-) using a 400 MHz NMR spectrometer (JEOL, JNM-ECZR). The self-diffusion coefficients were calculated using the following equation:[20]

$$\ln\left(\frac{S}{S_0}\right) = -\gamma^2 g^2 \delta^2 D\,(\Delta - \delta/3) \qquad (2\text{-}1)$$

where S/S_0 is the echo attenuation, γ ($s^{-1}\,T^{-1}$) is the gyromagnetic field, g ($T\,m^{-1}$) is the strength of the signal, δ (s) is the duration of the gradient pulse, and Δ (s) is the interval between the gradient pulses. The magnetic field gradient pulses were applied in the 1.0–13.5 $T\,m^{-1}$ range with an interval of 50 ms for each pulse. For the PGSE-NMR experiments, each symmetrical NMR microtube (5 mm diameter, Shigemi) was filled with an electrolyte up to a height of ~ 5 mm (70 μL) and sealed in a dry room (dew point < −40 °C). The self-diffusion coefficients were measured for Li^+ (^{7}Li), SBP^+ or EMI^+ (^{1}H), and BF_4^- (^{19}F) using the slopes of the intensity *versus* strength of the magnetic field gradient at room temperature (T = 25 °C).

Raman spectroscopy was conducted using neat PC, 0−3 M $LiBF_4$/PC, (1 M $LiBF_4$ + 1−3 M $SBPBF_4$)/PC, and (1 M $LiBF_4$ + 1−3.5 M $EMIBF_4$)/PC, to determine the solvation

environments and ionic pairs in $LiBF_4$/PC with or without the additional supporting electrolytic salts. Raman spectra were recorded on a Horiba Jobin Yvon LabRAM HR800 spectrometer at a resolution of 0.5 cm^{-1} using a 532 nm line from a semiconductor laser.

2.2.4 Electrode preparation

AC (YP-50F, Kuraray) and LTO (Toho Titanium) were employed as active materials in the positive and negative electrodes, respectively. Each active material was mixed with 10 wt.% of Ketjen Black (KB, ECD-600JD, Ketjen Black International) and 10 wt.% of a polytetrafluorethylene (PTFE) binder (Du Pont-Mitsui Fluorochemicals Company), and subsequently roll pressed at fixed thicknesses and densities (AC: 400 μm and 0.41 g cm^{-3}; LTO: 200 μm and 0.68 g cm^{-3}). The electrode thicknesses of AC and LTO were determined to maximize the energy densities of 2032 coin cells.[4] The pressed electrodes were pasted on 40-μm-thick etched Al foils using a conductive adhesive agent (Hitasol AB-1, Hitachi Chemical). The mass loadings of the electrodes (coin-type cell: $\phi = 16$ mm, laminate-type cell: 2 × 2 cm^2) were fixed at 12.8 and 16.8 mg cm^{-2} for LTO and AC, respectively (LTO//AC mass ratio: 0.76).[4]

2.2.5 Cell assembly and electrochemical measurements

Three types of cells were used for the electrochemical measurements, as shown in Fig. 2-3 (a–c). The 2032 coin-type cells (Fig. 2-3 (a)) were used to perform charge–discharge tests for the LTO//AC hybrid capacitors. Prior to the electrochemical measurements, the LTO and AC electrodes were dried overnight; a 35-μm-thick cellulose separator (75% porosity,[21] Nippon Kodoshi (NKK)) soaked with the prepared electrolytes was added between the electrodes. The soaked electrodes and separator were placed in a

vacuum (−70 kPa) for 10 min to guarantee electrolyte impregnation. The wet separator was sandwiched between the LTO and AC electrodes and sealed in a stainless-steel cell to construct the LTO//AC hybrid capacitor. A potentiostat unit (HJ 1001 SD 8, Hokuto) was used to perform constant-current (CC) charge–discharge cycles within a voltage range of 0–3.0 V. The discharge current densities were set from 1 to 200 mA cm^{-2} to obtain the discharge characteristics while maintaining a charge current of 1 mA cm^{-2}. Prior to the electrochemical measurements, the cells were pre-cycled twice in a voltage range of 0–3.0 V and a low current density of 0.1 mA cm^{-2}.

To obtain the ionic resistances of the AC and LTO electrode macropores, electrochemical impedance spectroscopy (EIS) was performed on the AC//AC or LTO//LTO symmetric laminate-type cells (Fig. 2-3 (b), 2-electrode cell, fully discharged with a state-of-charge (SOC) = 0%). Additionally, EIS was performed on SOC-controlled LTO//LTO symmetric laminate-type cells (Fig. 2-3 (c), 4-electrode cell, SOC = 25%) to obtain R_{ct} values of the LTO electrodes. The adopted 4-electrode cell has the advantage of not requiring unnecessary disassembly of the cells prior to the SOC-controlled EIS (Fig. 2-1 (c)).[16] The EIS was performed at T = 25 °C using a perturbation signal of ±10 mV in a frequency range of 0.01–65.5 kHz. The finite-length short-circuit terminus Warburg element was employed to fit the impedance spectra at an SOC of 25%.[13]

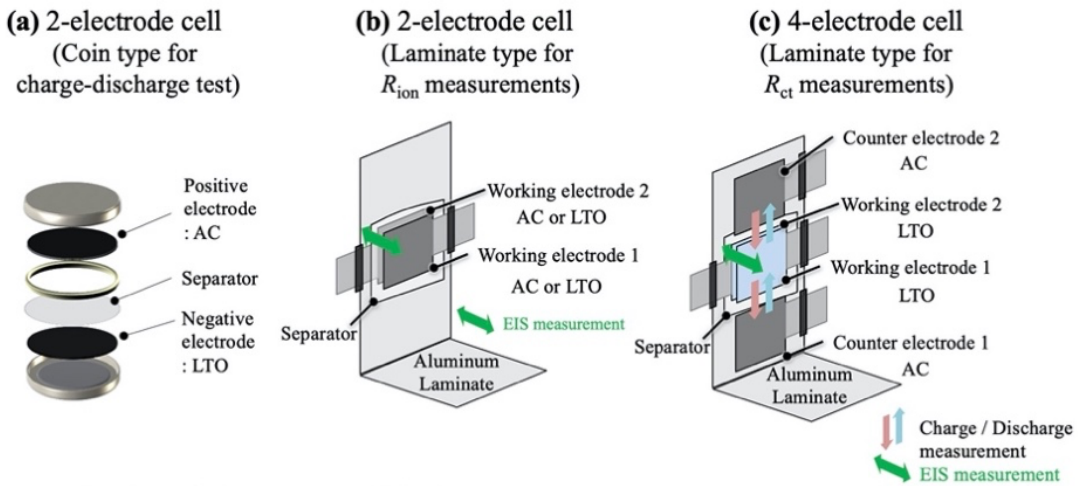

Fig. 2-3. (a)-(c) Schematics of the prepared cell configurations. **(a)** 2-electrode cell (coin-type for the charge–discharge test), **(b)** 2-electrode cell (laminate-type for the measurement of the ionic resistance (R_{ion}) in EIS), and **(c)** 4-electrode cell (laminate-type for the measurement of charge-transfer resistance (R_{ct}) in EIS).

2.2.6 Symmetric cell configuration

Fig. 2-4 (a) shows an LTO//LTO symmetric laminate-type cell configuration using two identical 200-μm-thick LTO negative electrodes with an area of 4 cm^2 (2 cm × 2 cm; a total of 8 cm^2), and two identical 400-μm-thick AC positive electrodes with an area of 4 cm^2 (2 cm × 2 cm; a total of 8 cm^2). As shown in the illustration and photograph in Fig. 2-4 (a), the LTO electrodes are placed in the center of the cell and sandwiched with a cellulose separator; the AC electrodes are placed on the top and bottom of the LTO electrodes. This configuration facilitates switching between the following two measurement modes: i) charge and discharge in the LTO//AC hybrid capacitor configuration and ii) EIS measurements in the LTO//LTO symmetric configuration; the cable connections could be easily changed without disassembling the cells, unlike in a previously reported symmetric cell configuration.[22]

Prior to the EIS, charge–discharge tests were performed on the symmetric cells in

the LTO//AC hybrid capacitor mode to confirm the proper functioning of the symmetric cell as a hybrid capacitor. To facilitate a comparison with respect to the charge–discharge tests, a normal cell configuration was assembled with LTO (8 cm^2) and AC (8 cm^2) being placed face-to-face and sandwiching a cellulose separator. The symmetric cells were charged at a low current density of 1 mA cm^{-2} *via* the constant-current and constant-voltage mode (CC-CV) at 2.7 V for 12 h (cut-off duration) and subsequently discharged at 0.05 mA cm^{-2} *via* the CC mode; the normal cell was charged at 1 mA cm^{-2} *via* the CC-CV mode at 2.7 V for 1 h only. Fig. 2-4 (b) shows the discharge curves obtained for the symmetric and normal cells. As shown in the figure, there is no significant difference in the exhibited cell capacity (4.3 and 4.1 mA h for the symmetric and normal cells, respectively); this demonstrates the validity of the assembled symmetric cells for controlling the charged state of LTO.

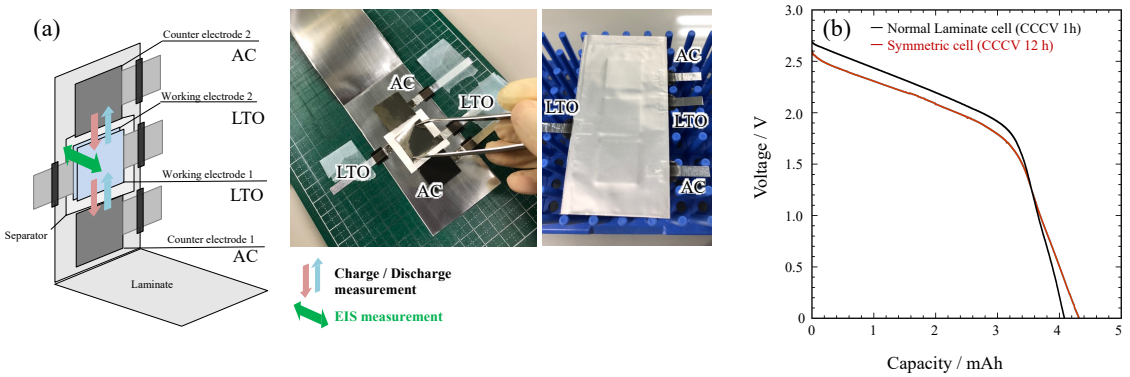

Fig. 2-4. (a) Configuration of LTO//LTO symmetric cells. (LTO: 4 cm^2 (2 cm × 2 cm) × 2 sheets (total: 8 cm^2), AC: 4 cm^2 (2 cm × 2 cm) × 2 sheets (total: 8 cm^2), laminate-type cell). **(b)** Discharge tests for the normal laminate-type cells and symmetric cells. Symmetric cells: charging at 1 mA cm^{-2} *via* the constant-current and constant-voltage mode (CC-CV) at 2.7 V for 12 h (cut-off duration) and subsequent discharging at 0.05 mA cm^{-2} *via* the CC mode; normal cell: charging at 1 mA cm^{-2} *via* the CC-CV mode at 2.7 V for 1 h.

2.2.7 Simulation of charge-transfer resistance within the LTO electrode macropores

To investigate the distribution of R_{ct} in the macropores of the 200-μm-thick LTO electrodes, TLM simulations were performed based on a previous study.[23] Fig. 2-5 depicts the equivalent circuit model of the electrode macropores and the electrode/electrolyte interface based on TLM. In this model, if the electrochemical reaction follows the Butler–Volmer equation and the LTO electrode potential is sufficiently high compared to its standard electrode potential, the LTO current density i (A cm^{-2}) can be expressed in the form of Equation (2-2); the contribution of the reduction current is ignored:

$$i = zFk^{\circ} \cdot C_R \cdot \exp\frac{(1-\alpha)zF(E-E^{\circ})}{RT_{abs}} \quad (2\text{-}2)$$

where z is the number of electrons involved in the electrode reaction, F (C mol^{-1}) is the Faraday constant, k° (cm s^{-1}) is the standard reaction rate constant, C_R (mol cm^{-3}) is the concentration of the reduction species, α is the transfer coefficient, E (V) is the electrode potential, E° (V) is the standard electrode potential, R (J K^{-1} mol^{-1}) is the gas constant, and T_{abs} (K) is the absolute temperature. E° is the only parameter in Equation (2-2) that varies depending on its position x within the LTO electrode ($0 \le x \le 200$ μm), where x = 0 corresponds to the current collector side. Using Equation (2-2), the distribution of the reaction current density along x [$i(x)$; A cm^{-3}] can be expressed as the following:

$$i(x) = zFk^{\circ} \cdot C_R \cdot \exp\frac{E(x)}{B} \quad (2\text{-}3)$$

where B is a constant that corresponds to the Tafel gradient (B = 51 mV at α = 0.5 and T_{abs} = 298 K).[23] Therefore, the distribution of R_{ct} in the electrode [$R_{ct}(x)$, Ω cm^3] can be expressed as the following:

$$R_{ct}(x) = \frac{\partial E(x)}{\partial i(x)} = \frac{B}{i(x)} \quad (2\text{-}4)$$

Because the total ionic current $i(x)$ passes through the electrolyte as an ionic conductor

with ionic resistance R_{ion} (Ω cm), the potential gradient within the electrode macropores, $d\phi_{ion}(x)/dx$, can be expressed as follows:

$$\frac{d\emptyset_{ion}(x)}{dx} = -R_{ion} \cdot \int_0^{\lambda} i(x)\, dx \qquad (2\text{-}5)$$

where λ is the LTO electrode thickness. Assuming that the electronic resistance is negligible, that is, the potential gradient within an electrical conductor ($d\varphi_e(x)/dx$) is zero,[23] the electrode potential gradient $dE(x)/dx$ can be obtained as the negative form of $d\varphi_{ion}(x)/dx$, which corresponds to the following equation:

$$\frac{dE(x)}{dx} = -\frac{d\emptyset_{ion}(x)}{dx} = R_{ion} \cdot \int_0^{\lambda} i(x)\, dx \qquad (2\text{-}6)$$

By simultaneously solving equations (2-3) and (2-6),[23] $i(x)$ can be rewritten as follows:

$$i(x) = \frac{2B}{R_{ion}\,\lambda^2} \cdot \frac{\theta}{\cos^2\left(\frac{x}{\lambda}\theta\right)} \qquad (2\text{-}7)$$

where θ is a dimensionless parameter ($0 < \theta < \pi/2$) [24] which is expressed as the following:

$$\theta \tan\theta = \frac{R_{ion}\lambda}{2B} \cdot I_{app} \qquad (2\text{-}8)$$

where I_{app} (mA cm^{-2}) is the applied current. Finally, the substitution of $i(x)$ from Equation (2-7) into Equation (2-4) results in the following equation for $R_{ct}(x)$:

$$R_{ct}(x) = \frac{R_{ion}\,\lambda^2}{2} \cdot \frac{\cos^2\left(\frac{x}{\lambda}\theta\right)}{\theta} \qquad (2\text{-}9)$$

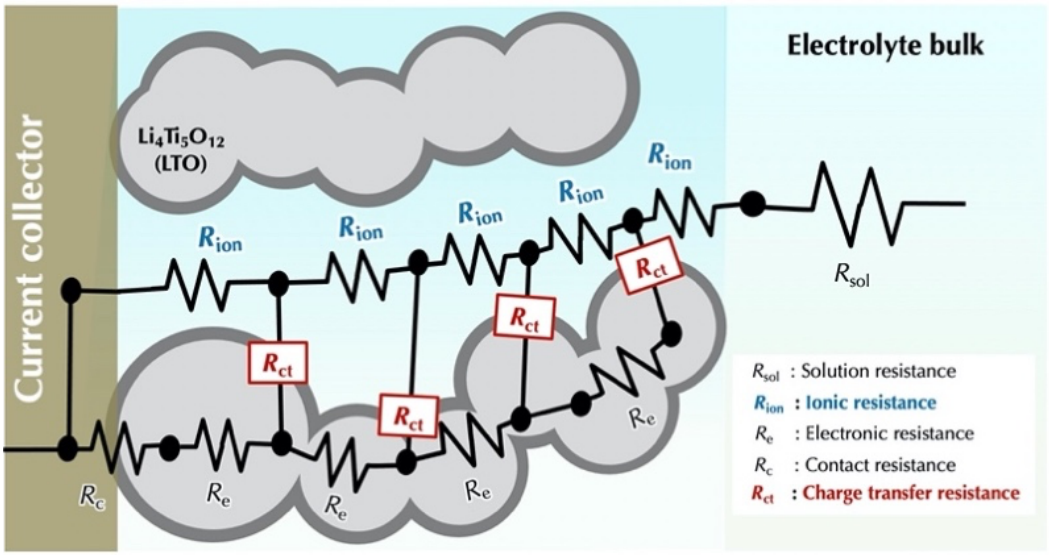

Fig. 2-5. Simulation model for the distribution of R_{ct} within the LTO electrode macropores based on TLM. R_e, R_c, and R_{sol} represent the electronic, contact, and solution resistances, respectively.

2.3 Results and discussion

2.3.1 Ionic conductivities of various dual-cation electrolytes

Fig. 2-6 presents the ionic conductivities of 1 M $LiBF_4$/PC as a function of concentrations of different species of the supporting electrolytic salts ($SBPBF_4$, $EMIBF_4$, $TEMABF_4$, and $TEABF_4$). The ionic conductivity of the SBP-based dual-cation electrolyte [(1 M $LiBF_4$ + x M $SBPBF_4$)/PC, $0 \leq x \leq 3$] peaks at $x = 2$ (7.7 mS cm^{-1}).[16] This value is 2.3 times greater than that of the single-cation system (1 M $LiBF_4$/PC, 3.4 mS cm^{-1}); the maximum values for the TEMA- and TEA-based dual-cation electrolytes are 7.0 and 6.7 mS cm^{-1}, respectively. Notably, the concentrations of the added $TEMABF_4$ and $TEABF_4$ in 1 M $LiBF_4$/PC are restricted to 2 M and 1 M, respectively, owing to their maximum solubility in PC (2.2 and 1.1 M for $TEMABF_4$ and $TEABF_4$, respectively).[18] The EMI-based dual-cation electrolyte [(1 M $LiBF_4$ + x M $EMIBF_4$)/PC, $0 \leq x \leq 4.5$]

exhibits a higher ionic conductivity than that of the $SBPBF_4$-based electrolyte at all concentrations, and increases to 10.9 mS cm^{-1} at x = 3.5 before plateauing. Using these results, four different dual-cation electrolyte compositions were selected for the subsequent experiments, with values of x corresponding to their maximum ionic conductivities [x = 2, 3.5, 2, and 1 for $SBPBF_4$, $EMIBF_4$, $TEMABF_4$, and $TEABF_4$, respectively]. The discharge characteristics of the four selected electrolytes were investigated in the thick LTO//AC hybrid systems, as described in Section 2.3.2.

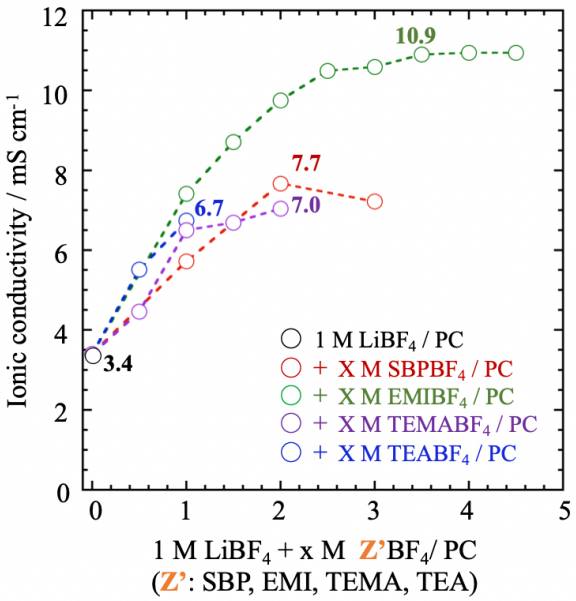

Fig. 2-6. Comparison of the ionic conductivities of the single-cation (1 M $LiBF_4$/PC, 3.4 mS cm^{-1}), SBP-based [(1 M $LiBF_4$ + x M $SBPBF_4$)/PC, $1 \le x \le 3$], EMI-based [(1 M $LiBF_4$ + x M $EMIBF_4$)/PC, $1 \le x \le 4.5$], TEMA-based (1 M $LiBF_4$ + x M $TEMABF_4$)/PC, $0.5 \le x \le 2$], and TEA-based dual-cation electrolytes (1 M $LiBF_4$ + x M $TEABF_4$)/PC, $0.5 \le x \le 1$].

2.3.2 Discharge characteristics of various dual-cation electrolytes

Fig. 2-7 shows the discharge characteristics of the thick-electrode LTO//AC hybrid capacitors (200-μm-thick LTO and 400-μm-thick AC) obtained using the single-cation [1 M $LiBF_4$/PC, Fig. 2-7 (a)] and the other investigated dual-cation electrolytes, such as 1 M $LiBF_4$/PC with 2 M $SBPBF_4$ (Fig. 2-7 (b)), 3.5 M $EMIBF_4$ (Fig. 2-7 (c)), 2 M $TEMABF_4$ (Fig. 2-7 (d)), and 1 M $TEABF_4$ (Fig. 2-7 (e)). The discharge curves at 1 mA cm^{-2} for all investigated electrolytes (Fig. 2-7 (a–e)) show a sloping profile based on the combination of a constant potential discharge (LTO negative electrode) and a capacitive incline (AC positive electrode).[4, 16] As shown in Fig. 2-7 (a), the capacity exhibited by the single-cation electrolyte starts to decrease at current densities above 20 mA cm^{-2} with an increase in the ohmic drops and polarization in the discharge potential profiles, resulting in low capacity retention. The addition of 2 M $SBPBF_4$ to the single-cation electrolyte (Fig. 2-7 (b)) is noted to improve the capacity retention at discharge currents greater than 20 mA cm^{-2}, with smaller ohmic drops and polarization due to the enhanced ionic conductivity.[16] The EMI-based dual-cation electrolyte (Fig. 2-7 (c)) showcases an even higher capacity retention and smaller degree of polarization compared to those of the SBP-based electrolyte, thereby demonstrating the effectiveness of the increase in ionic conductivity. The TEMA-based (Fig. 2-7 (d)) and TEA-based (Fig. 2-7 (e)) dual-cation electrolytes exhibit improvements in discharge characteristics that are similar to those of the SBP-based electrolyte. The summarized results in Fig. 2-7 (f) reveal that at a high discharge current of 200 mA cm^{-1}, all investigated dual-cation electrolytes exhibit a higher discharge capacity retention (≥ 36%) than that of the single-cation electrolyte (4.4%). The capacity retention of the EMI-based electrolyte is the highest (64%) among the parepared dual-cation electrolytes, followed by the SBP-based (48%), TEMA-based

(41%), and TEA-based dual-cation electrolytes (36%); this trend agrees well with that corresponding to their ionic conductivities (Fig. 2-6). To investigate the reasons behind the improved discharge characteristics, the bulk transport parameters of the EMI- and SBP-based dual-cation electrolytes were subsequently analyzed; these systems were selected because they exhibited higher power performances than those of the other dual-cation systems.

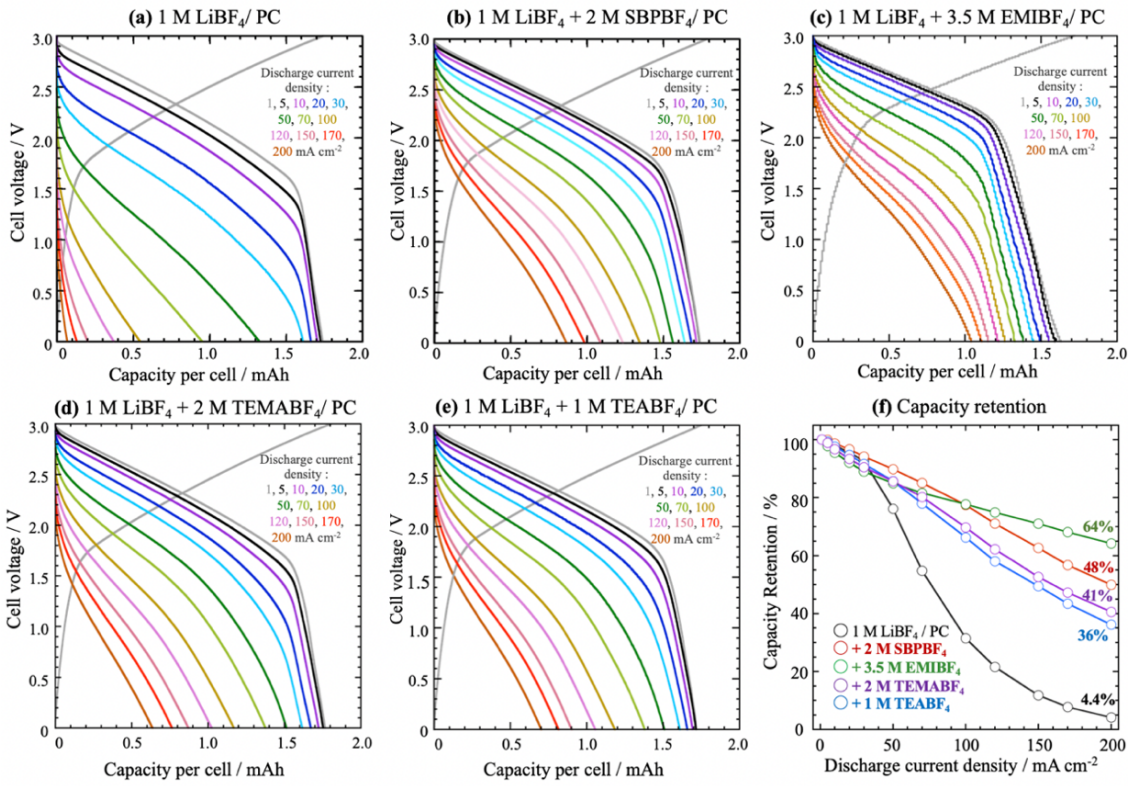

Fig. 2-7. Discharge characteristics of the **(a)** single-cation (1 M $LiBF_4$/PC), **(b)** SBP-based [(1 M $LiBF_4$ + 2 M $SBPBF_4$)/PC], **(c)** EMI-based [(1 M $LiBF_4$ + 3.5 M $EMIBF_4$)/PC], **(d)** TEMA-based [(1 M $LiBF_4$ + 2 M $TEMABF_4$)/PC], and **(e)** TEA-based [(1 M $LiBF_4$ + 1 M $TEABF_4$)/PC] dual-cation electrolytes at discharge current densities ranging from 1 to 200 mA cm^{-2} and a fixed charge current density of 1 mA cm^{-1}. **(f)** Discharge capacity retention of all investigated electrolytes, normalized by the capacity at a discharge current density of 1 mA cm^{-2}.

To determine the dependence of power performance on the concentration of the added supporting electrolyte in the dual-cation system, electrolyte compositions with various concentrations of $SBPBF_4$ [(1 M $LiBF_4$ + x M $SBPBF_4$)/PC; $0 \leq x \leq 3$] were prepared and tested. The procedure employed for the rate-capability tests was the same as that described for experiments whose results are shown in Fig. 2-7. Fig. 2-8 reveals that the optimal discharge performance is obtained for $SBPBF_4$ concentrations above 2 M due to higher capacity retention than below 1 M. The obtained results are in good agreement with the ionic conductivities shown in Fig. 2-6. Accordingly, the $SBPBF_4$ concentration was fixed at 2 M to take advantage of the dual-cation system while minimizing the concentration of $SBPBF_4$.

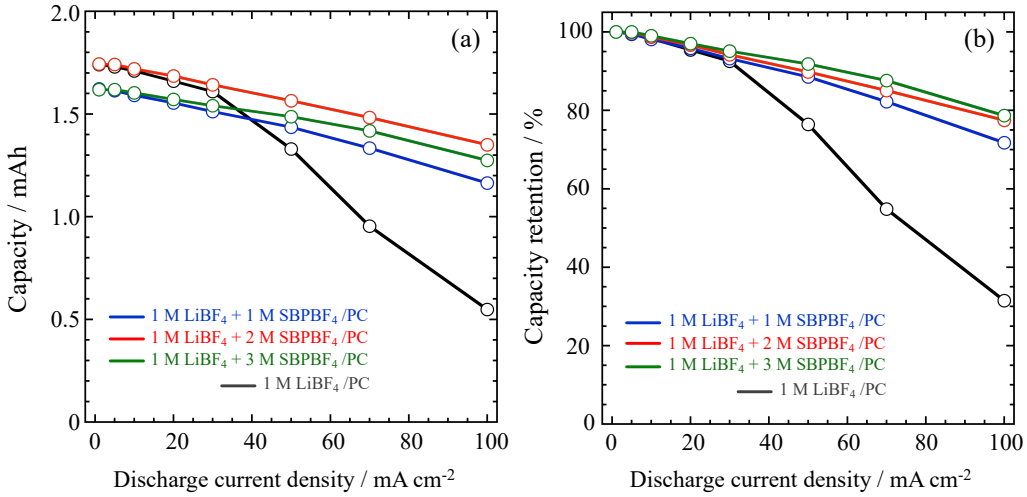

Fig. 2-8. Results of performance tests corresponding to (a) capacity and (b) capacity retention of the 2-electrode cells with single-cation (1 M $LiBF_4$/PC) and dual-cation [(1 M $LiBF_4$ + x M $SBPBF_4$)/PC; $0 \leq x \leq 3$)] electrolytes at discharge current densities ranging from 1 to 100 mA cm^{-2} and an applied charge current density of 1 mA cm^{-2}.

After comparing the rate capability of LTO//AC systems with the single-cation (1 M $LiBF_4$/PC) and dual-cation electrolytes (1 M $LiBF_4$ + 2 M $SBPBF_4$/PC), as shown in Fig. 2-7, the dependency of the electrochemical performance of LTO//AC systems on their electrode thicknesses was subsequently investigated. First, LTO and AC electrodes with different thicknesses compared to that of the standard electrode (LTO: 200 μm, 0.68 g cm^{-3}; AC: 400 μm, 0.41 g cm^{-3}) were prepared. Thin (LTO: 40 μm, 0.85 g cm^{-3}; AC: 80 μm, 0.53 g cm^{-3}) and thick (LTO: 300 μm, 0.65 g cm^{-3}; AC: 600 μm, 0.40 g cm^{-3}) electrodes were fabricated. The thin LTO (40 μm) and AC (80 μm) electrodes were prepared by coating either an LTO or AC slurry containing 80 wt.% of LTO or AC powders, respectively, 10 wt.% of KB as a conductive agent, and 10 wt.% of a polyvinylidene fluoride (PVDF) binder dissolved in 1-methyl-2-pyrrolidone (NMP), on a 20-μm-thick etched aluminum foil. The thick LTO and AC electrodes were prepared by adjusting the pressing pressure on the electrode pastes. The rate-capability results for three LTO//AC systems with and without $SBPBF_4$ are shown in Fig. 2-9. It is to be noted that the current density mentioned in Fig. 2-9 is normalized by the weight of LTO (g^{-1}) instead of cm^{-2} (see Fig. 2-7), because of the variation in electrode masses. The results of the thin electrodes in Fig. 2-9 do not indicate significant differences in the rate capability of electrolytes with or without $SBPBF_4$, compared to electrodes with standard thicknesses (Fig. 2-9 (b)). In contrast to the thin system, the results of the thick electrodes shown in Fig. 2-9 (c) indicate that the difference between the two electrolytes becomes pronounced as the dual-cation system is observed to maintain 70% of its capacity (1.28 mAh) at 3.3 mA g^{-1}; the capacity of the single-cation system decreases to only 14% of its capacity (0.23 mAh).

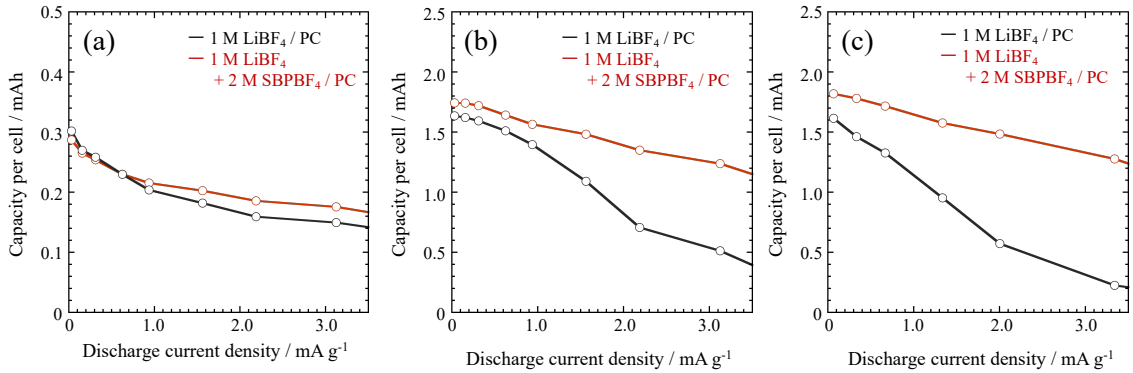

Fig. 2-9. Dependence of the rate capability on electrode thickness at a charge current density of 0.03 mA g^{-1}. **(a)** LTO: 40 μm, AC: 80 μm, **(b)** LTO: 200 μm, AC: 400 μm, **(c)** LTO: 300 μm, AC: 600 μm.

2.3.3 Physical properties of the SBP- and EMI-based dual-cation electrolytes

Table 2-1 shows the physical properties of the single-cation and dual-cation electrolytes at various concentrations of $SBPBF_4$ and $EMIBF_4$. As mentioned in Section 2.3.1, the ionic conductivity increases significantly as the concentrations of $SBPBF_4$ and $EMIBF_4$ increase up to 2 and 3.5 M, respectively; however, their viscosities also increase by two to seven times that of the single-cation electrolyte. Meanwhile, the self-diffusion coefficients of all investigated ionic species (Li^+, BF_4^-, and SBP^+ or EMI^+), which were evaluated *via* PGSE-NMR, decrease with an increase in the concentration of $SBPBF_4$ or $EMIBF_4$ owing to the increase in their viscosity.

Table 2-1 Ionic conductivities, viscosities, self-diffusion coefficients, transport numbers, and individual ionic conductivities for the single-cation and dual-cation electrolytes at various concentrations of $SBPBF_4$ and $EMIBF_4$.

	Ionic conductivity / mS cm^{-1}	Viscosity / cP	Self-diffusion coefficient / 10^{-10} m^2 s^{-1}			Transport number / -			Individual ionic conductivity / mS cm^{-1}		
			Li^+	SBP^+ / EMI^+	BF_4^-	Li^+	SBP^+ / EMI^+	BF_4^-	Li^+	SBP^+ / EMI^+	BF_4^-
1 M $LiBF_4$ / PC	3.40	6.77	0.88	-	1.26	0.41	-	0.59	1.40	-	2.00
1 M $LiBF_4$ + 1 M $SBPBF_4$ / PC	5.72	11.4	0.56	1.03	0.92	0.16	0.30	0.54	0.94	1.72	3.06
1 M $LiBF_4$ + 2 M $SBPBF_4$ / PC	7.67	18.4	0.30	0.62	0.52	0.10	0.40	0.50	0.75	3.07	3.85
1 M $LiBF_4$ + 3 M $SBPBF_4$ / PC	7.22	30.7	0.16	0.35	0.30	0.07	0.43	0.50	0.48	3.13	3.61
1 M $LiBF_4$ + 1 M $EMIBF_4$ / PC	7.41	9.73	0.61	1.20	0.93	0.17	0.33	0.51	1.23	2.43	3.75
1 M $LiBF_4$ + 2 M $EMIBF_4$ / PC	8.71	13.9	0.49	1.00	0.77	0.10	0.42	0.48	0.89	3.61	4.21
1 M $LiBF_4$ + 3.5 M $EMIBF_4$ / PC	10.9	24.3	0.26	0.62	0.42	0.06	0.50	0.44	0.65	5.48	4.76
1 M $LiBF_4$ + 4.5 M $EMIBF_4$ / PC	10.5	48.7	0.13	0.38	0.22	0.04	0.56	0.40	0.40	5.93	4.19

Note: "Ionic conductivity" in this table refers to the ionic conductivity obtained from the conductivity meter and "Individual ionic conductivity" refers to the observed ionic conductivity multiplied by the transport number of each ion species.[16]

To elucidate the role of the supporting electrolytes on changes in ionic conductivities and self-diffusion coefficients, Raman spectroscopy was employed to analyze the single-cation and dual-cation electrolytes with different concentrations. The Raman spectra of the single-cation electrolyte between 680 and 790 cm^{-1} (Fig. 2-9 (a)) indicate that as the $LiBF_4$ concentration increases, the peak intensity attributed to the symmetric ring deformation of solvated PC at ~ 721 cm^{-1} increases; a corresponding decrease in the peak intensity of "free" PC at ~ 712 cm^{-1} is also observed.[25-26] These results are consistent with those obtained in previous studies,[25-26] and indicate enhanced Li^+–PC interactions, which lead to an increase in the Li^+ solvation number and thereby a decrease in the Li^+ diffusion coefficients. Similarly, the peak at ~ 766 cm^{-1} attributed to the BF_4^- stretching (free BF_4^-) varies with increasing $LiBF_4$ concentration. The new peak at a higher wavenumber of ~ 773 cm^{-1}, which can be attributed to the contact ion pairs (CIP) between Li^+ and BF_4^-, clearly appears at a $LiBF_4$ concentration above 2 M,[26] which results in a decrease in the

BF_4^- diffusion coefficients. For the dual-cation electrolytes (Figs. 2-9 (b) and (c)), the peak intensity ratios between those corresponding to the solvated (721 cm^{-1}) and free PC (712 cm^{-1}) barely change compared to those of $LiBF_4$/PC, even upon the addition of 3 M $SBPBF_4$ or 3.5 M $EMIBF_4$; this indicates that the interaction between Li^+ and PC is significantly stronger than that between the added cation (SBP^+ or EMI^+) and PC. The peak intensity corresponding to free BF_4^- (766 cm^{-1}) increases with an increase in the concentration of $SBPBF_4$ or $EMIBF_4$. The peak intensity corresponding to CIP (773 cm^{-1}) also increases; however, its extent is considerably less than that of the peak corresponding to free BF_4^- stretching. The highly dissociative nature of $SBPBF_4$ and $EMIBF_4$ are possibly responsible for this slight change in the peaks corresponding to PC and CIP upon the addition of SBP^+ or EMI^+. However, the differences between the obtained Raman spectra of the SBP-based and EMI-based dual-cation electrolytes are not sufficiently clear.

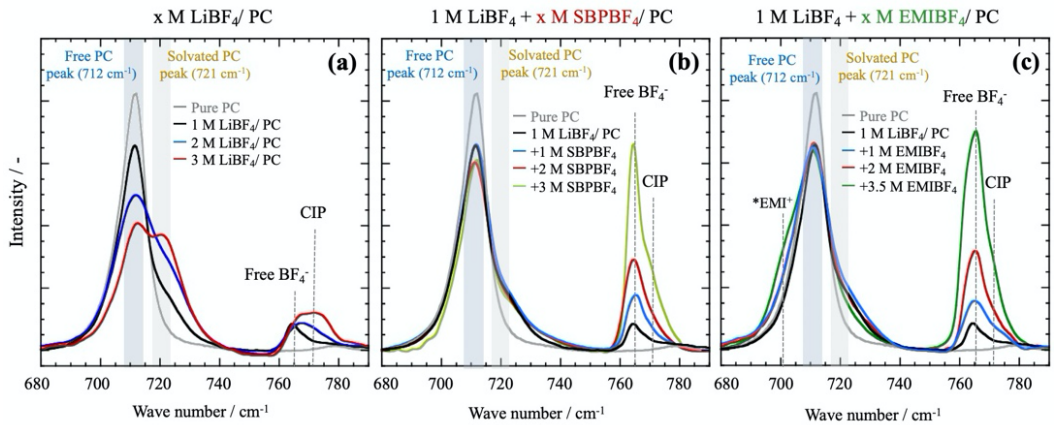

Fig. 2-9. Raman spectra of **(a)** single-cation (0–3 M $LiBF_4$/PC), **(b)** SBP-based [(1 M $LiBF_4$ + 0–3 M $SBPBF_4$)/PC], and **(c)** EMI-based [(1 M $LiBF_4$ + 0–3.5 M $EMIBF_4$)/PC] dual-cation electrolytes in the range of 680–790 cm^{-1}. The "Free BF_4^-" peak is attributed to a dissociated BF_4^- stretching peak observed at 766 cm^{-1} and the "CIP" peak corresponds to the shifted BF_4^- stretching peak (773 cm^{-1}) attributed to a contact ion pair.

To complement the Raman spectra results and further elucidate the difference between the self-diffusion coefficients of $SBPBF_4$ and $EMIBF_4$, the ratio of R_{ion} and R_{PC}, which is referred to as R-value,[27] was considered. This parameter represents the ratio between the Stokes radius of an ion (R_{ion}) and the radius of the PC solvent (R_{PC}), and is estimated using the obtained self-diffusion coefficients D as follows:

$$D = k_B T / 6\pi\eta R \quad (2\text{-}10)$$

$$R_{ion}/R_{PC} = D_{PC}/D_{ion} \quad (2\text{-}11),$$

where Equation 2-10 is known as the Stokes–Einstein equation, k_B is the Boltzmann's constant (1.38×10^{-23} J K^{-1}), T is the temperature (K), and η is the viscosity of the electrolyte (Pa s^{-1}). Equation 2-10 has been derived for hard spherical particles diffusing in a uniform medium.[27] The introduction of R_{ion}/R_{PC} in Equation 2-11 facilitates the discussion of the change in D_{ion}, independent of T and η. The estimated R-values are plotted in Figs. 2-10 (a)–(b). As shown in Fig. 2-10 (a), R_{BF4-}/R_{PC} for the single-cation electrolyte showcases a steep increase with increasing electrolyte concentration, whereas gentle inclines are observed for the dual-cation electrolytes. The R_{Li+}/R_{PC} results in Fig. 2-10 (b) indicate only slight differences among the three electrolytes. These results suggest that, for the dual-cation electrolytes, CIP between Li^+ and BF_4^- increases with the addition of $SBPBF_4$ or $EMIBF_4$, whereas the increase in the overall sum of CIP is significantly restrained owing to the highly dissociative supporting electrolytic salts. These results are also consistent with the Raman spectra shown in Figs. 2-9 (b)–(c). The obtained values of R_{EMI+}/R_{PC} (1.4–1.5) are smaller compared to those of R_{SBP+}/R_{PC} (1.2–1.3), probably owing to the smaller Van der Waals volume of EMI^+ (116 $Å^3$) [28] than that of SBP^+ (141 $Å^3$);[29] this results in higher EMI^+ diffusion coefficients than that of SBP^+ at similar values of added concentration.

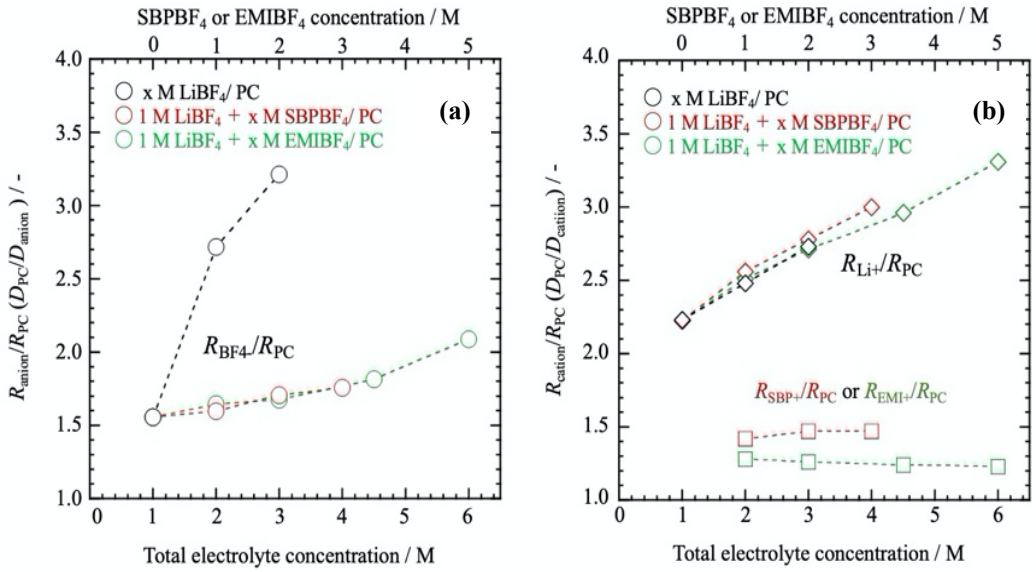

Fig. 2-10. Plots of R-value (R_{ion}/R_{PC}: ratio of ionic radius and that corresponding to PC solvation) of single-cation, SBP-, and EMI-based dual-cation electrolytes. **(a)** R_{BF4-}/R_{PC} and **(b)** R_{cation}/R_{PC} are shown. All Raman spectra are normalized by the peak corresponding to the ethyl group vibration of the PC molecule (848 cm^{-1}), which is independent of the electrolytic salt concentration.[25]

To further support the results obtained *via* Raman spectroscopy, NMR was conducted with different electrolyte compositions: x M $LiBF_4$ in PC (x = 0–3) and 1 M $LiBF_4$ + x M $SBPBF_4$ in PC (x = 1–3). To follow the resonance shifts of PC that were attributed to the change in Li^+ solvation, the chemical shifts of the carbonyl group of PC were focused on in the ^{13}C-NMR analyses,[30] which were conducted on a JEOL 400 MHz NMR spectrometer. The results are presented in Fig. 2-11. Upon dissolution of the Li salt in the solvent, the solvent coordination of Li^+ shifts the carbonyl carbon resonances upfield. Indeed, the ^{13}C-NMR shifts for x M $LiBF_4$ in PC (x = 0–3) show a linear relationship with the concentration of $LiBF_4$. In contrast to these results, no obvious changes are observed in the spectra obtained for the system with 1 M $LiBF_4$ + x M

$SBPBF_4$ in PC (x = 1–3); this suggests the solvation structure is not drastically changed upon the addition of $SBPBF_4$ in the electrolyte. These results are consistent with those obtained *via* Raman spectroscopy (Fig. 2-9).

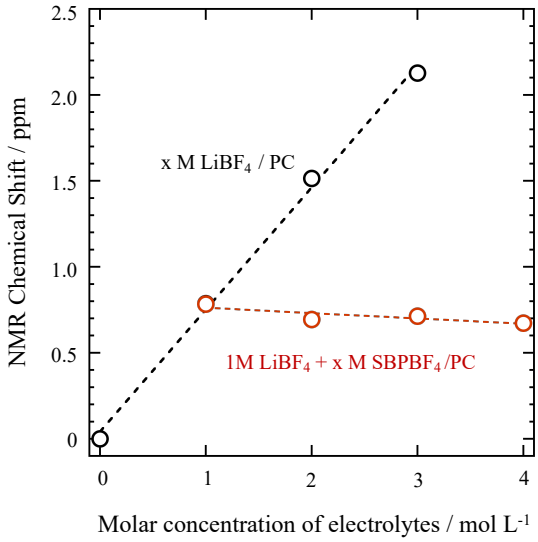

Fig. 2-11. Chemical shifts of the PC carbonyl peak in ^{13}C-NMR spectra plotted against the total molar concentration of two electrolytes: x M $LiBF_4$ in PC (x = 0–3; colored in black) and 1 M $LiBF_4$ + x M $SBPBF_4$ in PC (x = 1–3; colored in red).

The transport numbers, t_x, corresponding to the ion species x in the dual-cation electrolytes (x = Li^+, SBP^+ or EMI^+, and BF_4^-) were determined using the following equation:[16]

$$t_x = \frac{N_x D_x}{N_{[Li+]} D_{[Li+]} + N_{[BF4-]} D_{[BF4-]} + N_{[SBP+ or\ EMI+]} D_{[SBP+ or\ EMI+]}} \quad (2\text{-}12)$$

where N_x and D_x are the carrier number and self-diffusion coefficient of the ion species x, respectively. To compare the contribution of each ion to the overall electrolyte conductivity, the ionic conductivities of individual ionic species were estimated

[individual ionic conductivity, σ_x, (x = Li^+, SBP^+ or EMI^+, and BF_4^-)] using the following equation:[16]

$$\sigma_x = \sigma_{electrolyte} \times t_x \quad (2\text{-}13)$$

where $\sigma_{electrolyte}$ is the ionic conductivity of the electrolyte obtained using the conductivity meter.

Table 2-1 shows that with increasing concentrations of SBP^+ or EMI^+, both t_{Li+} and σ_{Li+} decrease, whereas t_x and σ_x for SBP^+/EMI^+ increase and are greater than those of lithium ions for all electrolyte compositions. Notably, σ_{Li+} for the 1 M $LiBF_4$ + 3.5 M $EMIBF_4$ (0.65 mS cm^{-1}) electrolyte is less than half of that of the single-cation (1 M $LiBF_4$, 1.4 mS cm^{-1}) electrolyte; however, the former outperforms the latter in terms of discharge characteristics, as shown in Fig. 2-7. These results highlight the importance of the presence of $EMIBF_4$ as a supporting electrolytic salt for the thick-electrode LTO//AC system, where the sum of σ_{EMI+} and σ_{BF4-} reaches 94% of the electrolyte conductivity of the 1 M $LiBF_4$ + 3.5 M $EMIBF_4$/PC system. To further analyze the impact of the enhanced ionic conductivity of dual-cation electrolytes on the electrochemical characteristics of LTO//AC, the ionic resistance (R_{ion}) was separately evaluated within the electrode structures and the charge-transfer resistance (R_{ct}) was attributed to the lithiation/delithiation of LTO based on the EIS.

2.3.4 Impedance experiments on symmetric cells and simulations

EIS was performed to obtain detailed insights into the transport properties of the electrolytes. Symmetric cells (Fig. 2-3 (b)) were designed to determine the ionic resistance (R_{ion}) within the macropores of the thick AC (positive) or LTO (negative) electrodes. Figs. 2-12 (a)–(b) show the EIS spectra of the AC//AC and LTO//LTO

symmetric cells (SOC = 0%), respectively. As shown in the inset of Fig. 2-12 (a), R_{ion} is calculated by subtracting R_{start} from R_{end}, and enables the comparison of pure R_{ion} values for electrolytes with different ionic conductivities.[31] The R_{ion} calculated for the AC positive electrode yields a lower value for the EMI-based dual-cation electrolyte (68 Ω cm^2) than those for the SBP-based (93 Ω cm^2) and single-cation (187 Ω cm^2) electrolytes. Similar results are observed for the LTO//LTO symmetric cells (Fig. 2-12 (b)); R_{ion} of the EMI-based dual-cation electrolyte (11 Ω cm^2) is lower than those of the SBP-based (14 Ω cm^2) and single-cation (27 Ω cm^2) electrolytes. The difference in the magnitudes of R_{ion} between AC and LTO is due to the difference in their inherent porous structures and electrode thicknesses (200 μm in LTO and 400 μm in AC). Nevertheless, the obtained results indicate that the ionic transport within the macropores attributed to the LTO or AC thick-electrode structures occurs more readily in the EMI- and SBP-based dual-cation electrolytes. The enhanced ionic transport of the dual-cation electrolytes significantly suppresses the ohmic drops (IR drops) in the charge–discharge curves of the LTO//AC systems. Fig. 2-12 (c) shows the EIS spectra of the LTO//LTO symmetric cells in the lithiated state (SOC = 25%). In contrast to the spectra at SOC = 0%, a semicircle corresponding to the R_{ct} of LTO lithiation/delithiation[32] appears in the middle-frequency region (10–20 Hz). Interestingly, the diameters of R_{ct} in the dual-cation electrolytes are smaller than that in the single-cation electrolyte, although lithium-ion transport in the bulk electrolyte becomes slower in the presence of SBP^+ or EMI^+. The R_{ct} values are estimated by fitting the EIS spectra with an equivalent circuit, as shown in the inset of Fig. 2-12 (c). The R_{ct} estimated for the EMI-based dual-cation electrolyte (1.7 Ω cm^2) is the lowest compared to the SBP-based (2.3 Ω cm^2) and single-cation electrolytes (3.6 Ω cm^2). This decrease in R_{ct} is possibly owing to the suppression of the ionic potential distribution

within the macropores of the thick electrode, where the ionic conduction is accelerated by the presence of the supporting electrolytic salt.[16] To obtain detailed information on the distribution of R_{ct} at each position within the electrode macropores, a TLM-based simulation of the R_{ct} distribution was conducted.

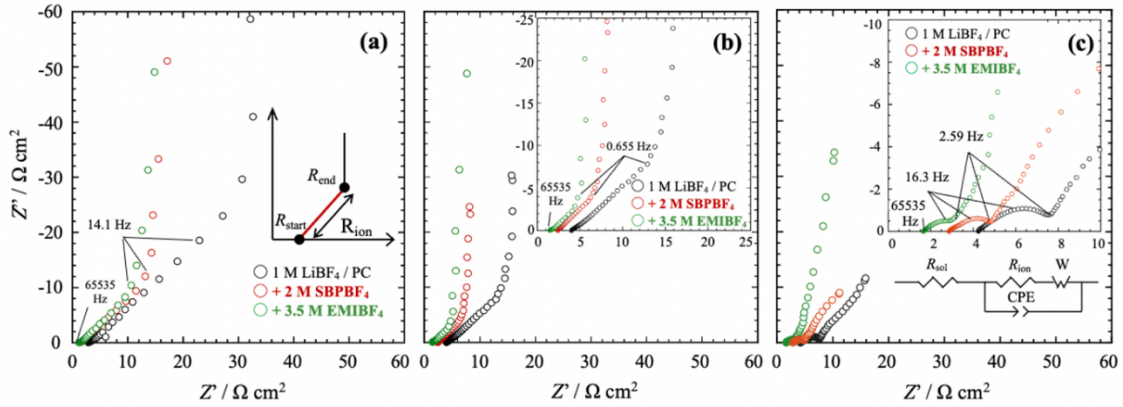

Fig. 2-12. EIS spectra for the single-cation (1 M $LiBF_4$/PC), SBP-based [(1 M $LiBF_4$ + 2 M $SBPBF_4$)/PC], and EMI-based [(1 M $LiBF_4$ + 3.5 M $EMIBF_4$)/PC] dual-cation electrolytes using **(a)** fully discharged AC//AC symmetric cells (SOC = 0%), **(b)** delithiated LTO//LTO symmetric cells (SOC = 0%), and **(c)** lithiated LTO//LTO symmetric cells (SOC = 25%).

To investigate the decrease in R_{ct} corresponding to the LTO lithiation/delithiation, the distribution of R_{ct} within the electrode macropores, $R_{ct}(x)$, was simulated using TLM (upper part in Fig. 2-13) and Equation (2-9). For the simulations, $R_{ct}(x)$ was assumed to vary depending on the position (x) along the direction of electrode thickness, where $x = 0$ and 200 μm correspond to the current collector and bulk electrolyte sides, respectively. Note that in Equations (2-9), the values of R_{ion} corresponding to each electrolyte composition were calculated using the reciprocals of their ionic conductivities. The corresponding simulation results are shown in the lower part of Fig. 2-13. Among the

three investigated electrolytes, there are no significant differences in the $R_{ct}(x)$ values (0.03–0.04 Ω cm^3) at the electrolyte bulk side (x = 200 μm). Conversely, near the current collector side (x = 0 μm), the gap between the single-cation and the other dual-cation electrolytes is increased. The $R_{ct}(x = 0)$ values for the single-cation, SBP-based, and EMI-based dual-cation electrolytes are 0.078 Ω cm^3, 0.049 Ω cm^3, and 0.040 Ω cm^3, respectively. The mean $R_{ct}(x)$ within the LTO electrode ($0 \leq x \leq 200$ μm) with the single-cation electrolyte (0.064 Ω cm^3) corresponds to an R_{ct} of 3.2 Ω cm^2, which is in good agreement with the R_{ct} obtained *via* EIS (3.6 Ω cm^2). Similarly, the R_{ct} values converted from the mean $R_{ct}(x)$ for the SBP-based and EMI-based electrolytes are 2.2 and 1.9 Ω cm^2, respectively; these values are also in good agreement with those obtained *via* EIS (2.3 and 1.7 Ω cm^2, respectively). These results indicate that the increase in $R_{ct}(x)$ from the bulk electrolyte (x = 200 μm) to the current collector side (x = 0 μm) was mitigated in the dual-cation electrolytes compared to that in the single-cation electrolyte, owing to their enhanced ionic conductivities; the mean R_{ct} values also agreed with those experimentally obtained *via* EIS. In particular, the high ionic conductivity associated with EMI^+ significantly mitigated the increase in $R_{ct}(x)$, which therefore resulted in a lower value of the observed R_{ct} and led to the enhancement of LTO kinetics and thereby the power densities of the thick LTO//AC hybrid capacitors. This configuration facilitates switching between the following two measurement modes: i) charge and discharge in the LTO//AC hybrid capacitor configuration and ii) EIS measurements in the LTO//LTO symmetric configuration; the cable connections could be easily changed without disassembling the cells, unlike in a previously reported symmetric cell configuration.

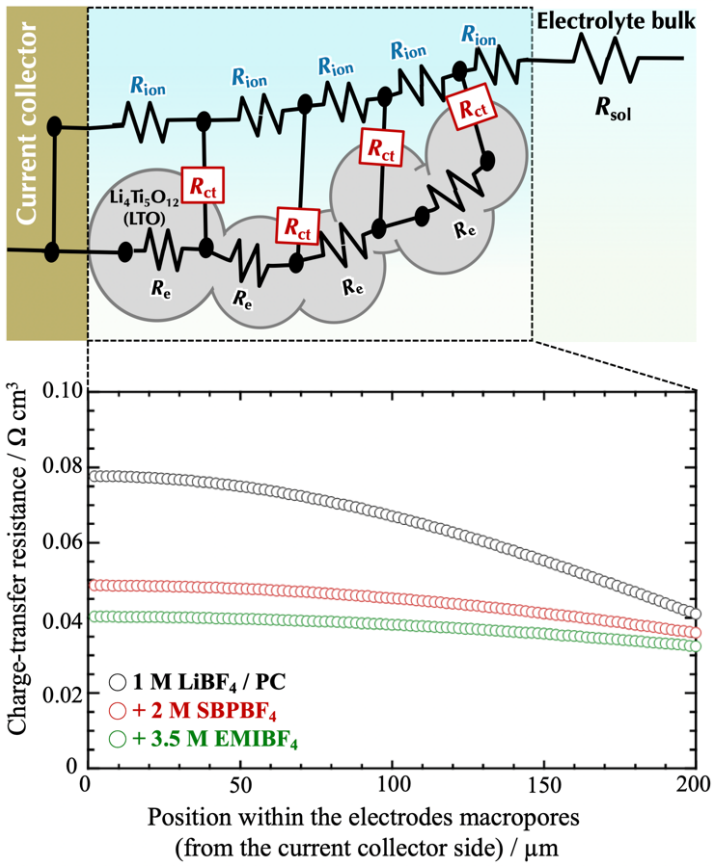

Fig. 2-13. [Upper part] Schematic of the simulation model for the distribution of R_{ct} within the macropores of the LTO thick electrodes. **[Lower part]** Simulated R_{ct} distribution within the macropores of the 200-μm-thick LTO electrode with the single-cation (1 M $LiBF_4$/PC), SBP-based [(1 M $LiBF_4$ + 2 M $SBPBF_4$)/PC], and EMI-based [(1 M $LiBF_4$ + 3.5 M $EMIBF_4$)/PC] dual-cation electrolytes. The length of the calculation stage for the simulation was set to 2 μm (divided into 100 stages). I_{app} in Equation (2-9) is set to 0.125 mA.

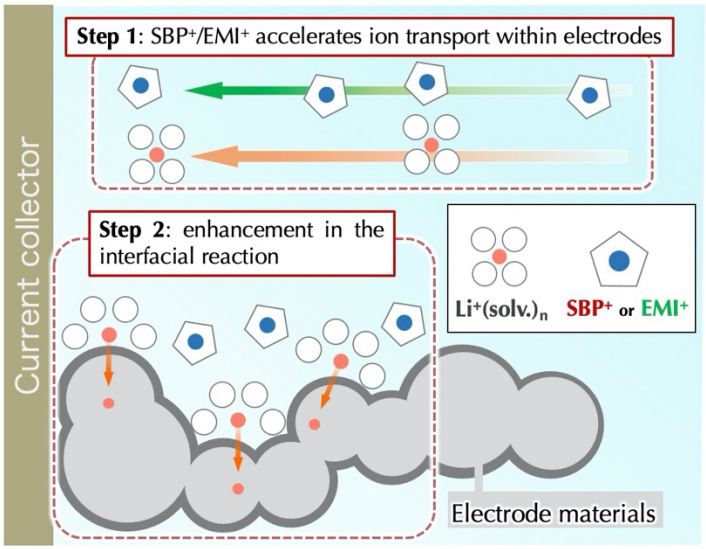

Fig. 2-14. Mechanism for accelerating the interfacial reaction in the LTO electrode.

2.3.5 Optimization of electrolyte compositions based on total ionic and individual Li^+ conductivities

The discussions presented in the earlier sections revealed that the presence of highly dissociative supporting electrolytic salts such as $EMIBF_4$ increased the overall ionic conductivity, resulting in reduced R_{ion} and R_{ct} for the lithiation/delithiation of LTO and in turn the enhanced power performance of LTO//AC; however, the σ_{Li+} in the bulk electrolyte decreased with the addition of $EMIBF_4$. To determine the effect of the balance between the total ionic conductivity of the electrolyte and σ_{Li+} on the power performance of thick-electrode LTO//AC cells, charge–discharge tests with different $LiBF_4$ concentrations in the single (x M $LiBF_4$/PC, $0 \le x \le 1.5$) and dual-cation electrolytes [(x M $LiBF_4$ + 2 M $SBPBF_4$ or 3.5 M $EMIBF_4$)/PC, $0 \le x \le 1.5$] were performed at different current densities. The results are plotted in Figs. 2-15 and 2-16. As shown in Fig. 2-15 (a), the capacity exhibited by the 0.5 M $LiBF_4$/PC system is lower than those exhibited by other $LiBF_4$ concentrations [x = 1.0 and 1.5 M, Figs. 2-15 (b)-(c)]. The overvoltage of the charge curve becomes pronounced from the middle of the SOC, whereas its inflection

point at ~ 2 V does not change (Fig. 2-16(a)). This overvoltage behavior is possibly because of the decrease in electrolyte conductivity when the concentrations of both Li^+ and BF_4^- decrease from 0.5 M (Fig. 2-15 (d), grey curve) during the charging mode (insertion of Li^+ into the LTO electrode and adsorption of BF_4^- on the surface of the AC electrode). Upon the addition of 2 M $SBPBF_4$ or 3.5 M $EMIBF_4$, the inflection points in the charging curve shift toward higher voltages above 2 V (Fig. 2-16 (b–c)), leading to a reduced capacity of almost half that of the electrolyte without the supporting electrolytes (Fig. 2-16 (a)). This shift in the inflection point voltages is possibly owing to the hindrance caused by Li^+ insertion into LTO *via* a decrease in σ_{Li+} below 0.5 mS cm^{-1} during charging (Fig. 2-15 (d)), and the presence of excess SBP^+ or EMI^+ *versus* Li^+ at the LTO/electrolyte interface. When the $LiBF_4$ concentration is increased to 1.5 M in the dual-cation electrolyte systems (Fig. 2-15 (c)), the exhibited capacity and rate capability appear significantly better compared to those of the 0.5 M electrolyte system; however, the rate capability is less pronounced than that of the 1.0 M electrolyte system (Fig. 2-15 (b)). Interestingly, the rate capability of the SBP-based dual-cation electrolyte is superior to that of the EMI-based dual-cation electrolyte, although the total ionic conductivity of the electrolyte for the former is inferior to that of the latter. The shift of the inflection point voltage in the presence of $EMIBF_4$ (Figs. 2-16 (d)–(f)) indicates that the insertion of Li^+ into LTO crystals is possibly hindered as the value of σ_{Li+} becomes too low (< 0.5 mS cm^{-1}) after the addition of 3.5 M EMI, compared to that with 2 M $SBPBF_4$. These results indicate the importance of the minimum value of σ_{Li+} (> 0.5 mS cm^{-1}) in dual-cation electrolytes; thus, a good balance between the total ionic conductivity and σ_{Li+} can be determined by controlling the concentration ratio between Li-based and supporting electrolytic salts to extract optimal performances from thick-electrode LTO//AC systems.

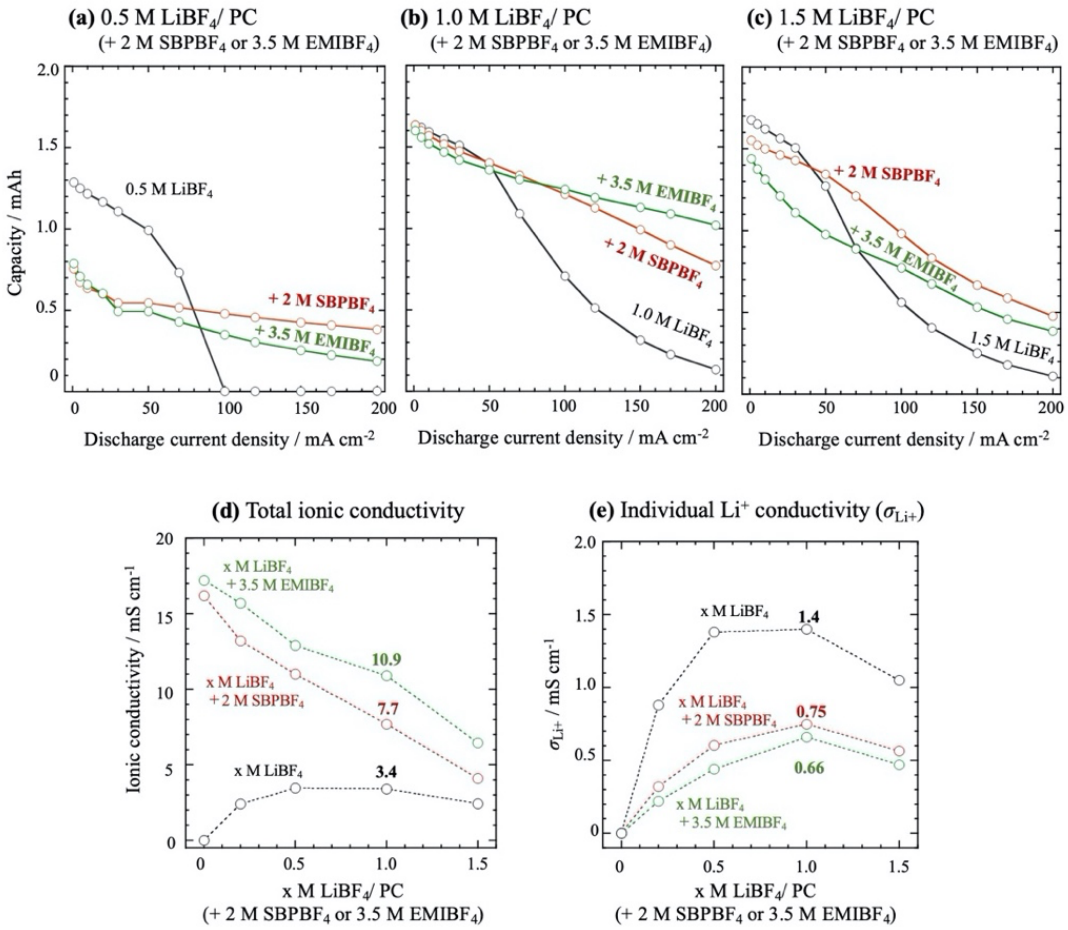

Fig. 2-15. Discharge characteristics of the **(a)** 0.5 M $LiBF_4$/PC, **(b)** 1.0 M $LiBF_4$/PC, and **(c)** 1.0 M $LiBF_4$/PC with or without 2 M $SBPBF_4$ or 3.5 M $EMIBF_4$ at discharge current densities ranging from 1 to 200 mA cm^{-2} and a fixed charge current density of 1 mA cm^{-1}. Comparison of the **(d)** total ionic and **(e)** individual Li^+ conductivities of the single-cation (0–1.5 M $LiBF_4$/PC), SBP-based [(0–1.5 M $LiBF_4$ + 2 M $SBPBF_4$)/PC], and EMI-based [(0–1.5 M $LiBF_4$ + 3.5 M $EMIBF_4$)/PC]. "Total ionic conductivity" refers to the measured ionic conductivity of the electrolytic solution and "individual Li^+ conductivity (σ_{Li+})" refers to the product of the total ionic conductivity and transport number of Li^+ (t_{Li+}).

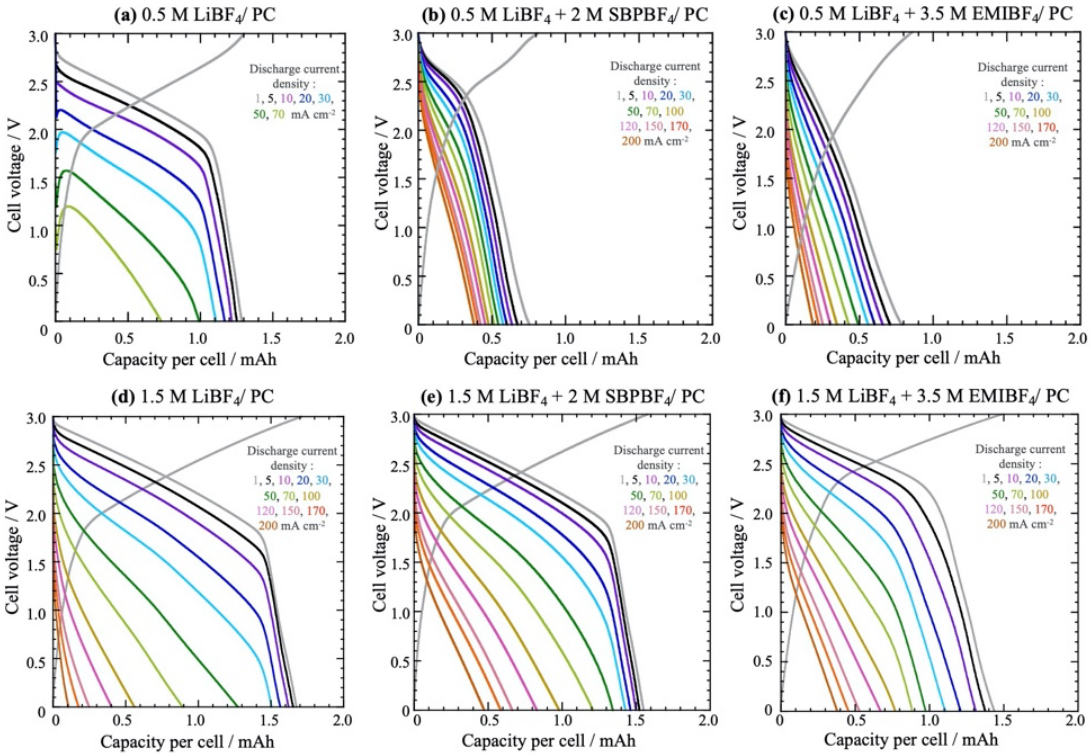

Fig. 2-16. Discharge characteristics of the **(a)** 0.5 M $LiBF_4$/PC, **(b)** (0.5 M $LiBF_4$ + 2 M $SBPBF_4$)/PC, **(c)** (0.5 M $LiBF_4$ + 3.5 M $EMIBF_4$)/PC, **(d)** 1.5 M $LiBF_4$/PC, **(e)** (1.5 M $LiBF_4$ + 2 M $SBPBF_4$)/PC, and **(f)** (1.5 M $LiBF_4$ + 3.5 M $EMIBF_4$)/PC electrolyte systems at discharge current densities ranging from 1 to 200 mA cm^{-2} and a fixed charge current density of 1 mA cm^{-1}.

2.4 Conclusion

Various dual-cation electrolytes featuring combinations of $LiBF_4$ with $SBPBF_4$, $EMIBF_4$, $TEMABF_4$, or $TEABF_4$ were prepared to increase the ionic conductivity and discharge performance of 600-μm-thick LTO//AC hybrid capacitors. All investigated dual-cation electrolytes exhibited higher ionic conductivities and discharge capabilities than that of the single-cation electrolyte (1 M $LiBF_4$/PC). In particular, the EMI-based dual-cation electrolyte [(1 M $LiBF_4$ + 3.5 M $EMIBF_4$)/PC] exhibited an optimal performance (64% capacity retention at 200 mA cm^{-2}) among all the electrolyte compositions. Detailed analysis of the transport parameters of the bulk electrolyte

combined with EIS measurements on symmetric electrode cells revealed that the presence of highly conductive cations, such as EMI^+, reduced both R_{ion} and R_{ct} during the lithiation/delithiation of LTO owing to the increase in overall ionic conductivity, despite the slowed lithium-ion transport in the bulk electrolyte. The TLM-based simulation of R_{ct} distribution within the 200-μm-thick LTO electrode supported the experimental EIS data; the increase in R_{ct} from the bulk electrolyte to the current collector side was mitigated in the EMI-based dual-cation electrolyte (an increase of 30%), compared to that of the single-cation electrolyte (an increase of 90%). The minimum value of σ_{Li+} (> 0.5 mS cm^{-1}) in dual-cation electrolytes was revealed to be an important factor for ensuring improved electrochemical performance in thick-electrode LTO//AC systems. These findings may provide a guideline for the design of high-energy-density Li-based energy storage devices employing thick electrodes without sacrificing the power density, and clarify the benefits of increasing the total ionic conductivity rather than focusing only on the acceleration of lithium-ion diffusion.

2.5 References

1. Amatucci, G. G.; Badway, F.; Du Pasquier, A.; Zheng, T., An asymmetric hybrid nonaqueous energy storage cell. *Journal of The Electrochemical Society* **2001,** *148* (8), A930-A939.
2. Long, J. W.; Bélanger, D.; Brousse, T.; Sugimoto, W.; Sassin, M. B.; Crosnier, O., Asymmetric electrochemical capacitors—Stretching the limits of aqueous electrolytes. *Mrs Bulletin* **2011,** *36* (7), 513-522.
3. Naoi, K.; Ishimoto, S.; Miyamoto, J.-i.; Naoi, W., Second generation 'nanohybrid supercapacitor': evolution of capacitive energy storage devices. *Energy & Environmental Science* **2012,** *5* (11), 9363-9373.
4. Iwama, E.; Ueda, T.; Ishihara, Y.; Ohshima, K.; Naoi, W.; Reid, M. T. H.; Naoi, K., High-voltage operation of $Li_4Ti_5O_{12}$/AC hybrid supercapacitor cell in carbonate and

sulfone electrolytes: Gas generation and its characterization. *Electrochimica Acta* **2019,** *301*, 312-318.

5. Wang, G.; Liu, Z.; Wu, J.; Lu, Q., Preparation and electrochemical capacitance behavior of TiO_2-B nanotubes for hybrid supercapacitor. *Materials Letters* **2012,** *71*, 120-122.

6. Wang, Q.; Wen, Z.; Li, J., A hybrid supercapacitor fabricated with a carbon nanotube cathode and a TiO_2–B nanowire anode. *Advanced Functional Materials* **2006,** *16* (16), 2141-2146.

7. Ma, S.-B.; Nam, K.-W.; Yoon, W.-S.; Yang, X.-Q.; Ahn, K.-Y.; Oh, K.-H.; Kim, K.-B., A novel concept of hybrid capacitor based on manganese oxide materials. *Electrochemistry Communications* **2007,** *9* (12), 2807-2811.

8. Sivakkumar, S. R.; Nerkar, J.; Pandolfo, A., Rate capability of graphite materials as negative electrodes in lithium-ion capacitors. *Electrochimica Acta* **2010,** *55* (9), 3330-3335.

9. Sivakkumar, S. R.; Pandolfo, A., Evaluation of lithium-ion capacitors assembled with pre-lithiated graphite anode and activated carbon cathode. *Electrochimica Acta* **2012,** *65*, 280-287.

10. Yuan, T.; Tan, Z.; Ma, C.; Yang, J.; Ma, Z. F.; Zheng, S., Challenges of Spinel $Li_4Ti_5O_{12}$ for Lithium‐Ion Battery Industrial Applications. *Advanced Energy Materials* **2017,** *7* (12), 1601625.

11. Naoi, K.; Naoi, W.; Aoyagi, S.; Miyamoto, J.-i.; Kamino, T., New generation "nanohybrid supercapacitor". *Accounts of chemical research* **2013,** *46* (5), 1075-1083.

12. Zheng, H.; Li, J.; Song, X.; Liu, G.; Battaglia, V. S., A comprehensive understanding of electrode thickness effects on the electrochemical performances of Li-ion battery cathodes. *Electrochimica Acta* **2012,** *71*, 258-265.

13. Ogihara, N.; Itou, Y.; Sasaki, T.; Takeuchi, Y., Impedance Spectroscopy Characterization of Porous Electrodes under Different Electrode Thickness Using a Symmetric Cell for High-Performance Lithium-Ion Batteries. *The Journal of Physical Chemistry C* **2015,** *119* (9), 4612-4619.

14. Kondo, K.; Sano, M.; Hiwara, A.; Omi, T.; Fujita, M.; Kuwae, A.; Iida, M.; Mogi, K.; Yokoyama, H., Conductivity and solvation of Li^+ ions of $LiPF_6$ in propylene carbonate solutions. *The Journal of Physical Chemistry B* **2000,** *104* (20), 5040-5044.

15. Yang, J.-J.; Kim, Y.-R.; Jeong, M.-G.; Yuk, Y.-J.; Kim, H.-J.; Park, S.-G., Synthesis and electrochemical characteristics of spherical $Li_4Ti_5O_{12}$/CNT composite materials for hybrid capacitors. *Journal of Electrochemical Science and Technology* **2015,** *6* (2), 59-64.

16. Chikaoka, Y.; Iwama, E.; Ueda, T.; Miyashita, N.; Seto, S.; Sakurai, M.; Naoi, W.; Reid, M. T. H.; Simon, P.; Naoi, K., Dual-Cation Electrolytes for High-Power and High-Energy LTO//AC Hybrid Capacitors. *The Journal of Physical Chemistry C* **2020**.
17. Ohno, H., Ionic Conductivity. In *Electrochemical Aspects of Ionic Liquids*, 2011; pp 87-93.
18. Chiba, K.; Ueda, T.; Yamamoto, H., Performance of electrolyte composed of spiro-type quaternary ammonium salt and electric double-layer capacitor using it. *Electrochemistry* **2007,** *75* (8), 664-667.
19. Shestakov, A.; Yudina, A.; Tulibaeva, G.; Shul'ga, Y. M.; Ignatova, A.; Yarmolenko, O., Effect of adding ionic liquid 1-ethyl-3-methylimidazolium tetrafluoroborate on the coordination environment of Li^+ ions in propylene carbonate, according to data from IR spectroscopy and quantum chemical modeling. *Russian Journal of Physical Chemistry A* **2017,** *91* (8), 1444-1450.
20. Hayamizu, K.; Aihara, Y.; Nakagawa, H.; Nukuda, T.; Price, W. S., Ionic conduction and ion diffusion in binary room-temperature ionic liquids composed of [emim][BF_4] and $LiBF_4$. *The Journal of Physical Chemistry B* **2004,** *108* (50), 19527-19532.
21. Azais, P.; Tamic, L.; Huitric, A.; Paulais, F.; Rohel, X. Separator film, its fabrication method, supercapacitor, battery and capacitor provided with said film. US. Patent 9,461,288., Oct. 4, 2016.
22. Ogihara, N.; Kawauchi, S.; Okuda, C.; Itou, Y.; Takeuchi, Y.; Ukyo, Y., Theoretical and experimental analysis of porous electrodes for lithium-ion batteries by electrochemical impedance spectroscopy using a symmetric cell. *Journal of the Electrochemical Society* **2012,** *159* (7), A1034-A1039.
23. Zyun, S.; Susumu, K.; Hajime, M., *Electrochemical impeadance*. Tokyo kagaku dojin: Kyoto, 2019.
24. Neyerlin, K.; Gu, W.; Jorne, J.; Clark Jr, A.; Gasteiger, H. A., Cathode catalyst utilization for the ORR in a PEMFC: Analytical model and experimental validation. *Journal of The Electrochemical Society* **2007,** *154* (2), B279.
25. Tsunekawa, H.; Narumi, A.; Sano, M.; Hiwara, A.; Fujita, M.; Yokoyama, H., Solvation and ion association studies of $LiBF_4$— propylenecarbonate and $LiBF_4$— propylenecarbonate— trimethyl phosphate solutions. *The Journal of Physical Chemistry B* **2003,** *107* (39), 10962-10966.
26. Hwang, S.; Kim, D.-H.; Shin, J. H.; Jang, J. E.; Ahn, K. H.; Lee, C.; Lee, H., Ionic Conduction and Solution Structure in $LiPF_6$ and $LiBF_4$ Propylene Carbonate Electrolytes. *The Journal of Physical Chemistry C* **2018,** *122* (34), 19438-19446.

27. Hayamizu, K.; Akiba, E.; Bando, T.; Aihara, Y., ^{1}H, ^{7}Li, and ^{19}F nuclear magnetic resonance and ionic conductivity studies for liquid electrolytes composed of glymes and polyetheneglycol dimethyl ethers of $CH_3O(CH_2CH_2O)_nCH_3$ (n= 3–50) doped with $LiN(SO_2CF_3)_2$. *The Journal of chemical physics* **2002,** *117* (12), 5929-5939.
28. Ue, M.; Murakami, A.; Nakamura, S., A convenient method to estimate ion size for electrolyte materials design. *Journal of The Electrochemical Society* **2002,** *149* (10), A1385.
29. Nguyen, H. V. T.; Kwak, K.; Lee, K.-K., 1, 1-Dimethylpyrrolidinium tetrafluoroborate as novel salt for high-voltage electric double-layer capacitors. *Electrochimica Acta* **2019,** *299*, 98-106.
30. Chapman, N.; Borodin, O.; Yoon, T.; Nguyen, C. C.; Lucht, B. L., Spectroscopic and density functional theory characterization of common lithium salt solvates in carbonate electrolytes for lithium batteries. *The Journal of Physical Chemistry C* **2017,** *121* (4), 2135-2148.
31. Conway, B. E., *Electrochemical supercapacitors : scientific fundamentals and technological applications*. Kluwer Academic : Plenum Press: New York, 1999.
32. Ishihara, Y.; Miyazaki, K.; Fukutsuka, T.; Abe, T., Kinetics of lithium-ion transfer at the interface between $Li_4Ti_5O_{12}$ thin films and organic electrolytes. *ECS Electrochemistry Letters* **2014,** *3* (8), A83-A86.

Section 3. Dual-Cation Electrolytes for High voltage operation in $Li_4Ti_5O_{12}$//AC Hybrid Capacitor System

3.1 Introduction

Owing to the growing concern for environmental issues, there is increasing demand for high-power devices for grid storage of electrical energy, something that is required for a sustainable society. Although electric-double-layer capacitors (EDLCs) have attracted research attention as high-power storage devices, their energy density is lower than that of batteries, and consequently, a large number of cells are required to achieve high energy density while using limited space for stationary storage. One common strategy for increasing the energy density involves replacing one of the electrodes of an EDLC with a lithium-ion battery electrode, yielding a device structure referred to as an asymmetric hybrid capacitor.[1-2] Among the various materials considered for hybrid-capacitor electrodes, spinel $Li_4Ti_5O_{12}$ (LTO) has attracted particular interest because of its many advantages, including high theoretical capacity (175 mAh g^{-1}), high reaction potential (1.55 V *vs.* Li/Li^+, a value at which electrolyte decomposition does not occur), and insignificant volume expansion (0.2%) during lithiation, all of which make it a promising candidate material for hybrid-capacitor negative electrodes.[3-4] By contrast, one drawback of LTO//activated carbon (AC) cells is that their operating voltages are typically restricted to the vicinity of 3.0 V because of the high reaction potential of the LTO negative electrode, and this limits their energy density.

To achieve higher energy density, operating voltages above 3.0 V are preferred (Fig. 3-1). However, I encountered here a second drawback of LTO//AC hybrids: when they

are operated at voltages above 3.0 V, irreversible oxidative decomposition occurs at the AC positive electrode, which leads to the release of H_2O adsorbed on the AC and the oxidation of propylene carbonate (PC). Moreover, H_2O and PC also diffuse to the LTO negative electrode, promoting their catalytic reductive decomposition on the LTO surface, which generates H_2 gas and dramatically degrades the performance of the cell.[5-6] Various strategies have been pursued to address this degradation problem during high-voltage operation, including replacing PC with a stable solvent such as ethyl isopropyl sulfone (EiPS) [6] or with an ionic liquid.[7] However, the above-mentioned electrolyte systems have high viscosity and low power density, and hence, no comprehensive practical solution has yet been developed to achieve high power density and low H_2 gas generation in the LTO//AC system.

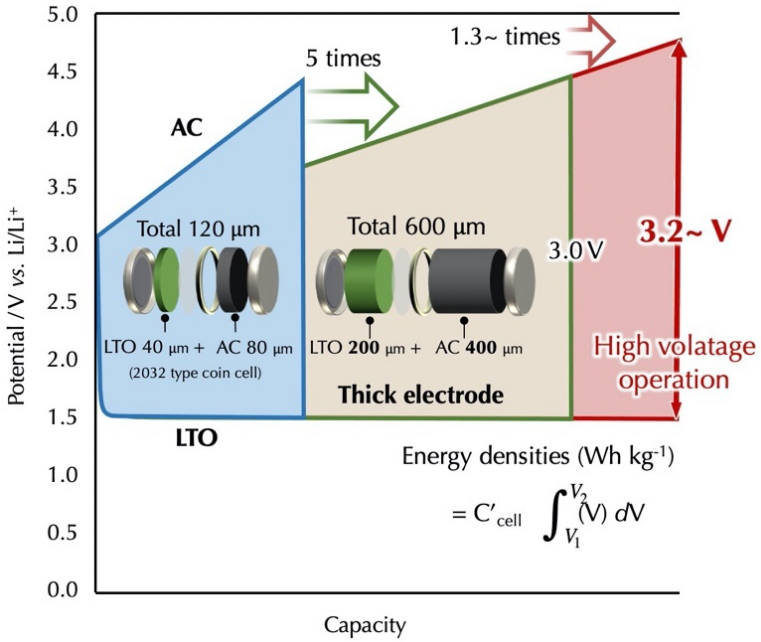

Fig. 3-1. Strategy for enhancing the energy density of an LTO//AC hybrid capacitor by operation at high voltage.

This study investigated the possibility of blending spiro(1,1′)-bipyrrolidinium tetrafluoroborate ($SBPBF_4$), a quaternary ammonium salt used in EDLCs, into a standard $LiBF_4$/PC electrolytic solution to yield a dual-cation electrolyte for use in LTO//AC hybrid capacitors.[8] Dual-cation electrolytes were originally introduced to improve ionic conductivity, and a significant improvement in output performance was observed for LTO//AC hybrid capacitors with dual-cation electrolytes, compared with those using conventional single-cation electrolytes. Along with the enhancement of power performance, the dual-cation electrolytes improved cyclability at a cell voltage of 3.0 V (Fig. 3-2).[8] Upon further investigation using dual-cation electrolytes, similar cyclability improvement was obtained even at 3.2 V, as well as the suppression of H_2 gas evolution under high-voltage floating conditions (3.5 V, 60 °C). The aim of this study was to elucidate the key mechanisms responsible for the H_2 gas-suppressing properties of dual-cation electrolytes in an LTO//AC system.

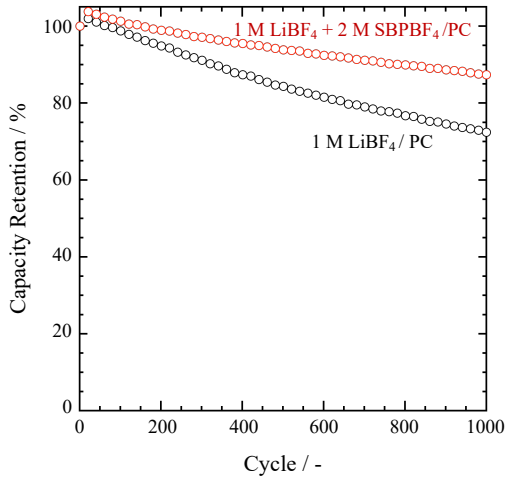

Fig. 3-2. Comparison of cyclability tests for the LTO/AC system at a cell voltage of 3.0 V using single-cation (1 M $LiBF_4$/PC) and dual-cation electrolytes (1 M $LiBF_4$ + 2 M $SBPBF_4$/PC) at a constant charge/discharge current of 5 mA cm^{-2}.

3.2 Experiments

3.2.1 Electrolyte preparation

All the electrolytes used in this study were prepared using lithium tetrafluoroborate ($LiBF_4$, Morita Chemical Industries, Japan) as the main electrolytic salt and PC (Kishida Chemicals, Japan, < 20 ppm water) as the solvent. The following three substances were used as additional supporting electrolytic salts: $SBPBF_4$ (Carlit Holdings, Japan), triethylmethylammonium tetrafluoroborate ($TEMABF_4$, Kishida Chemicals, Japan), and tetraethylammonium tetrafluoroborate ($TEABF_4$, Kishida Chemicals, Japan). All the electrolytes were prepared in an argon-filled glove box (Unico) with a dew point below −70 °C. Molecular sieves (5Å, TOSOH, Japan) were used to ensure that the water content of the prepared electrolytes did not exceed 20 ppm.

3.2.2 Electrode preparation

Activated carbon (AC, YP-50F, Kuraray) and $Li_4Ti_5O_{12}$ (LTO, Toho Titanium) were used as active materials for the positive and negative electrodes, respectively. Each active material was mixed with 10 wt.% of Ketjen Black (KB, ECD-600JD, Ketjen Black International) and 10 wt.% of polytetrafluorethylene binder (PTFE, Du Pont-Mitsui Fluorochemicals Company), then roll-pressed to prepare electrodes with fixed thicknesses and densities (400 μm and 0.41 g cm^{-3} for AC, 200 μm and 0.68 g cm^{-3} for LTO) with the aim to maximize the energy density for 2032 coin-type cells.[6] After roll-pressing, the electrodes were pasted on 40-μm-thick etched aluminum foils using Hitasol AB-1 (Hitachi Chemical). The mass loadings of punched-out electrodes (coin-type cell: diameter 16 mm; laminate-type cell: 4 × 2 cm^2) were 12.8 mg cm^{-2} (LTO) and 16.8 mg

cm^{-2} (AC), resulting in an LTO/AC mass ratio of 0.76. The LTO/AC mass ratio corresponds to the LTO/AC capacity ratio, which was calculated, from the mass and measured capacity of LTO (168 mAh g^{-1}) and AC (38 mAh g^{-1}), to have a value of 3.36 at a cell voltage of 3.0 V. The excess capacity of LTO (2.15 mAh cm^{-2}) versus AC (0.64 mAh cm^{-2}) retained a sufficient capacity margin even at the high cell voltage of 3.5 V, where the capacity of AC increases to *ca*. 1.71 mAh.[6]

3.2.3 Cycling tests using coin-type cells

The 2032 coin-type LTO//AC hybrid capacitors were assembled for cycling tests at 3.2 V. After drying overnight, the prepared electrodes and cellulose separator (35 μm thickness with 75% porosity,[9] Nippon Kodoshi (NKK)) were soaked in the electrolyte and then placed under vacuum (pressure = 70 kPa) for 10 min to ensure electrolyte impregnation. The wet separator was placed between the LTO and AC electrodes in the stainless-steel cases, and the coin cells were then sealed using a crimping machine. Constant-current (CC) charge–discharge cycles were conducted over the voltage range 0 to 3.2 V by means of a potentiostat unit (HJ 1001 SD 8, Hokuto). All the cells were placed in a climatic chamber to maintain the temperature at 25 °C. The discharge and charge current densities were maintained at 5 mA cm^{-2}. Prior to the cycling tests, the cells were pre-cycled twice at a low current density, 0.1 mA cm^{-2}, within a voltage window from 0 to 3.0 V.

3.2.4 Floating tests and gas analysis using laminate-type cells

Laminate cells were assembled to conduct floating tests at a constant voltage of 3.5 V to quantify the gas generated. The LTO negative and AC positive electrodes were pasted

on 40 μm thick etched aluminum foils using conductive carbon paste (Hitasol AB-1, Hitachi Chemical). Prior to cell assembly and vacuum sealing, the electrodes (surface area: 4 × 2 cm^2) were immersed in the electrolyte under vacuum (70 kPa) for 10 min. The weight of the electrolyte was fixed at 2 g. The laminate cell bags were seven times the size of the electrodes (55 cm^2) to mitigate the impact of the internal pressure increase due to gas generation. All laminate cells were assembled in a dry room (dew point below −40 °C). First, the assembled laminate cells were charged to 3.5 V at a current density of 1 mA cm^{-2} and then maintained at 3.5 V for 200 h at 60 °C. The volume of the gaseous compounds generated was quantified *via* Archimedean water displacement measurements before and after floating. For composition analysis by gas chromatography (GC, Shimadzu GC-2014 AT), 250 μL of the gaseous compounds was collected in a gas syringe and injected into the apparatus. The temperatures of the thermal detector and column were set at 200 °C and 180 °C, respectively, and the injection temperature was 170 °C.

3.2.5 Electrode surface characterization (SEM, XPS, and EIS)

Following the floating tests conducted at 3.5 V, the surface morphologies of the AC positive and LTO negative electrodes were observed by scanning electron microscopy (SEM, Hitachi High-Technologies HD5500). Prior to SEM observation, the LTO and AC electrodes used in the floating tests were rinsed with 10 drops of dimethyl carbonate and dried under vacuum for 15 min. To avoid air exposure of the SEM samples, all processes, including cell disassembly and electrode rinsing, were conducted in an argon -filled glove box, and the samples were transferred from the glove box to the SEM sample chamber using a transfer vessel. X-ray photoelectron spectroscopy (XPS, ULVAC-PHI Ltd., PHI X-tool) was used to analyze the changes in the electrode surface components of the LTO

and AC electrodes before and after the floating tests. The Al Kα line was used as an X-ray source, and the XPS spectra were calibrated assuming a C 1s binding energy of 284.9 eV.

The degraded LTO negative and AC positive electrodes after cycling at 3.2 V were characterized by electrochemical impedance spectroscopy (EIS) on symmetric LTO//LTO and AC//AC coin cells. The LTO//AC laminate-type cells were first pre-cycled (see Section 3.2.3) and then cycled between 0 and 3.2 V for 10 cycles. Charge–discharge cycling was conducted in constant current–constant voltage (CC-CV) mode at a current density of 1 mA cm^{-2}. The holding time during the CV mode was set to be within 1 h. After cell disassembly, the electrodes were punched into two pieces in the form of 15-mm-diameter discs. The punched-out discs and the newly soaked separator were then reassembled into 2032 coin cells with LTO//LTO or AC//AC symmetric configurations. EIS measurements (Solartron 1260/1287) were conducted on the prepared coin cells at open circuit voltage (OCV) and 25 °C with an amplitude of 10 mV over the frequency range 100 Hz to 65.5 kHz.

3.3 Results and discussion

3.3.1 LTO//AC cyclability at 3.2 V

High-voltage cyclability of the LTO//AC hybrid supercapacitor at 3.2 V up to 100 cycles was tested for both single-cation (1 M $LiBF_4$/ PC) and dual-cation (1 M $LiBF_4$ + 2 M $SBPBF_4$/ PC) electrolytes. The representative charge–discharge curves are shown in Fig. 3-3 (a) and (b), respectively. Overall, the shapes of the charge–discharge curves obtained are typical for LTO//AC hybrid capacitors, with a charge inflection point around 2.0 V corresponding to the start of the LTO voltage plateau. The slight difference in the

discharge flexion point voltage between the two electrolytes (~ 200 mV) is consistent with previous results.[8] Note that, for both electrolytes, the initial 5–10 cycles were required to reach the maximum cell capacity, mainly due to irreversible reactions such as electrolyte oxidative decomposition at the AC positive electrode.[6] Starting from the 10th cycle, the discharge cell capacity for both electrolytes gradually decreased without any obvious change in inflection points, while the capacity decrease gradient was less for the dual-cation electrolyte. Consequently, as shown in Fig. 3-3 (c), the dual-cation electrolyte showed better capacity retention after 100 cycles (96.4%) and slightly higher coulombic efficiency during cycling (92.7–99.4%) compared with the values for the single-cation electrolyte (capacity retention 92.9% and coulombic efficiency 92.2–99.2%). Fig. 3-3 (d) shows plots of the voltage (IR) drops in the discharge curves at the 10th, 25th, 50th, 75th, and 100th cycles, which indicate increased cell internal resistance during high-voltage cycling. The difference between two electrolytes in the IR drop at initial cycles (*ca*. 190 mV and 80 mV for the single-cation and dual-cation electrolytes, respectively) reflects the difference in their ionic conductivities (3.57 and 7.79 mS cm^{-1}, respectively). Up to the 100th cycle, the difference increased continuously; the slope obtained from the IR plots for the dual-cation electrolyte (0.14 mV per cycle) was less than that of the single-cation electrolyte by a factor of 0.4 (0.36 mV per cycle). According to a previous report, gaseous compounds, mainly H_2, generated by LTO//AC hybrid capacitors, play a critical role in enhancing the internal resistance of the cell.[6] To clarify the reason for the improvements in high-voltage cycling for the dual-cation electrolyte, gaseous compound analysis was performed after the high-voltage (3.5 V) floating tests.

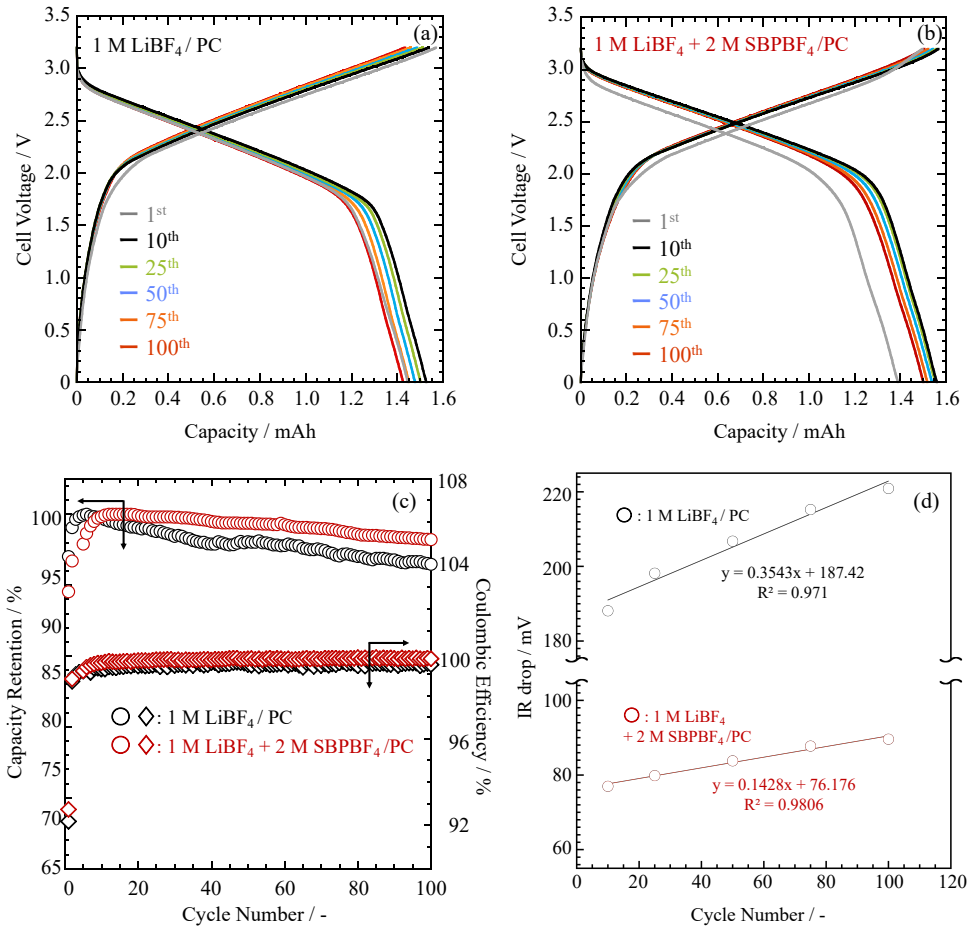

Fig. 3-3. Comparison of cyclability tests for the LTO//AC system at a cell voltage of 3.2 V and a constant charge–discharge current of 5 mA cm^{-2}: Charge–discharge curves of **(a)** single-cation (1 M $LiBF_4$/ PC) and **(b)** dual-cation electrolytes (1 M $LiBF_4$ + 2 M $SBPBF_4$/ PC). Plots of **(c)** capacity retention and coulombic efficiency and **(d)** IR drops at different cycles between the 10^{th} and 100^{th} cycles in single-cation and dual-cation electrolytes.

3.3.2 Quantifying gas emissions after high-voltage floating tests

High-voltage floating tests and GC were conducted to investigate gas generation from LTO//AC hybrid capacitors, both qualitatively and quantitatively. To accelerate gas generation, I chose a higher voltage (3.5 V) and temperature (60 °C) than the conditions used in the cycling tests. After 200 h of floating tests for the single-cation electrolyte (1

M $LiBF_4$/ PC), *ca*. 33 mL of gaseous compounds was generated. The generated gases were composed of 31 mL of H_2, 0.5 mL of CO_2, 1 mL of CO, and 0.1 mL of other compounds, including CH_4, C_2H_4, and C_2H_6. The variations in the main gas species (H_2, CO_2, CO) and the volume ratios were consistent with those mentioned in a previous report.[6] When the dual-cation electrolyte (*i.e.*, the single-cation electrolyte with the addition of 2 M $SBPBF_4$) was used, the generated gas volume decreased to 22 mL, a *ca.* 35% volume reduction, with all gas species reduced equally. The generation of these gases, especially H_2, from LTO//AC hybrid capacitors operated at a high voltage (over 3.0 V) could be attributed to a continuous PC solvent reductive decomposition at the LTO negative electrode surface, as well as to reduction of H_2O released from the AC positive electrode.[3, 6] Such a reduction in gas volume accompanying use of the dual-cation electrolyte indicates that the presence of $SBPBF_4$ in the electrolyte inhibits the reduction of PC and H_2O at the LTO surface. To examine the role of $SBPBF_4$, I investigated other electrolyte compositions in addition to the two electrolytes tested above, with the $LiBF_4$ concentration fixed at 1 M and varying $SBPBF_4$ concentrations, obtaining electrolytes with the formula 1 M $LiBF_4$ + *x* M $SBPBF_4$/ PC, where x = 0.0, 0.1, 0.5, 1.0, 2.0, or 3.0. The results summarized in Fig. 3-4 show that the addition of even small amounts of $SBPBF_4$ (0.1 M) produced an immediate reduction in the gas volume, which then decreased with increasing $SBPBF_4$ concentration in the electrolyte. The gaseous species and volume ratios remained almost the same with and without $SBPBF_4$; H_2 was the main component (> 90 vol.%) of the generated gases, while less than 10 vol.% of carbon oxides (CO and CO_2) and small amounts (< 1 vol.% in sum) of other gaseous species (CH_4, C_2H_4, and C_2H_6) were detected. These results strongly suggest that the presence of $SBPBF_4$ may hinder PC/H_2O reduction at the LTO/electrolyte interface.

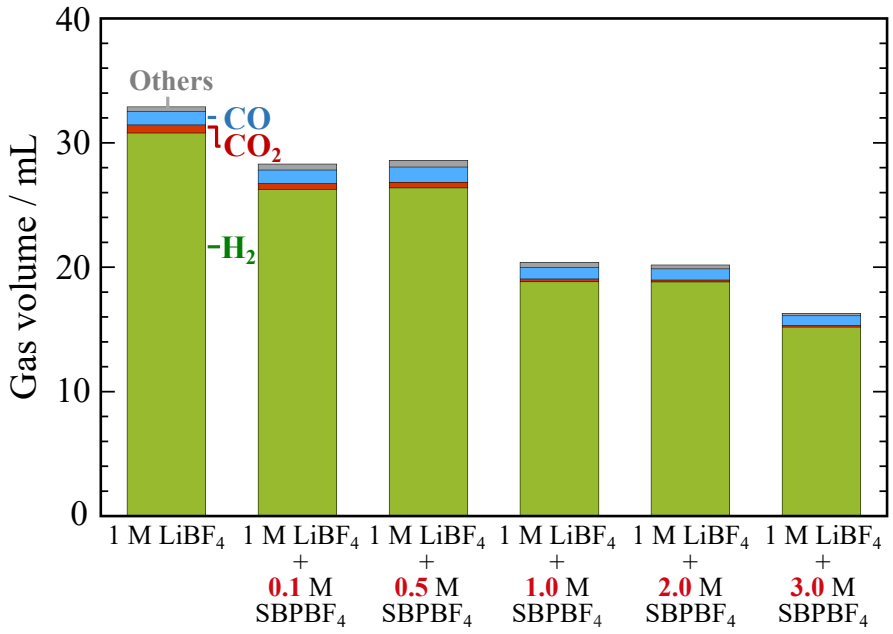

Fig. 3-4. Gas volumes generated from LTO//AC cells after floating tests at 3.5 V and 60 °C for 200 h using electrolyte compositions with various $SBPBF_4$ concentrations (1 M $LiBF_4$ + *x* M $SBPBF_4$/ PC; *x* = 0.0-3.0). "Others" represents small amounts of minority gas species, including CH_4, C_2H_4 and C_2H_6.

3.3.3 Surface characterization

Surface characterization, including SEM, XPS, and EIS analysis of LTO and AC electrodes, revealed the events occurring at the electrode/electrolyte interfaces during high-voltage operation (Figs. 3-5, 3-6, and 3-7). For the single-cation electrolyte (1 M $LiBF_4$/ PC), a comparison of the SEM images of the LTO negative electrodes before (Fig. 3-5 (a)) and after (Fig. 3-5 (b)) the floating tests revealed a significant change in their surface morphology. After the floating tests, the LTO surface was completely covered by a polymeric surface film, and the strings of the PTFE binders became thicker and less well defined owing to the adhesion of similar films on their surroundings. The results are consistent with those mentioned in a previous report and indicate drastic PC decomposition during the floating tests.[6] Little change is observed for the dual-cation

electrolyte (Fig. 3-5 (c)); the edges of the LTO particles and the PTFE strings remained readily discernible. The results of XPS analysis of the LTO electrodes, conducted before and after the floating tests, supported the SEM observations. As seen in the carbon 1s XPS spectra (Fig. 3-6 (a)), the contribution from C=O bonding (at 287.3 eV),[10-11] which originates from the decomposition of PC,[6, 12] was suppressed for the dual-cation electrolyte compared with that for the single-cation electrolyte. Minimal changes in the AC surface morphology could be observed in the SEM images (Fig. 3-5 (d)–(f)) for both electrolytes before and after floating tests; the XPS spectra (Fig. 3-6 (b)) are consistent with the SEM results. EIS analysis of the electrodes after high-voltage cycling was conducted to support the results of the surface characterization experiments. For the EIS measurements, LTO//LTO and AC//AC symmetric cells were reassembled from cycled LTO//AC cells. Note that a lower cell voltage (3.2 V) was applied for cycling than that for the floating tests (3.5 V), owing to electrode exfoliation from the attached current collectors during the floating tests. The EIS spectra are shown in Fig. 3-7. Overall, the spectra obtained before the floating tests were consistent with those shown in a previous result: the dual-cation electrolyte showed smaller ionic resistance within the macropores of thick electrodes (R_{ion}) for both LTO and AC electrodes, owing to its high ionic conductivity.[8] For LTO//LTO systems, semicircles corresponding to the accumulated SEI layer [13] appeared for both electrolytes after cycling (Fig. 3-7 (a)-(b)), but their diameters and corresponding frequencies at the top were different: 3.8 and 1.4 Ω cm^2 at 521 Hz and 6.6 kHz, respectively, for the single- and dual-cation electrolytes. These results indicate less degradation of the LTO surface (a smaller resistance increase after floating tests) for the dual-cation electrolyte because of the different nature of the LTO surface in the presence of $SBPBF_4$, and this is consistent with the SEM observation and XPS results.

However, there was no change in the overall EIS spectra and their knee frequencies[14] for the AC positive electrodes before and after cycling, showing unchanged electrochemical characteristics at the AC/electrolyte interfaces.

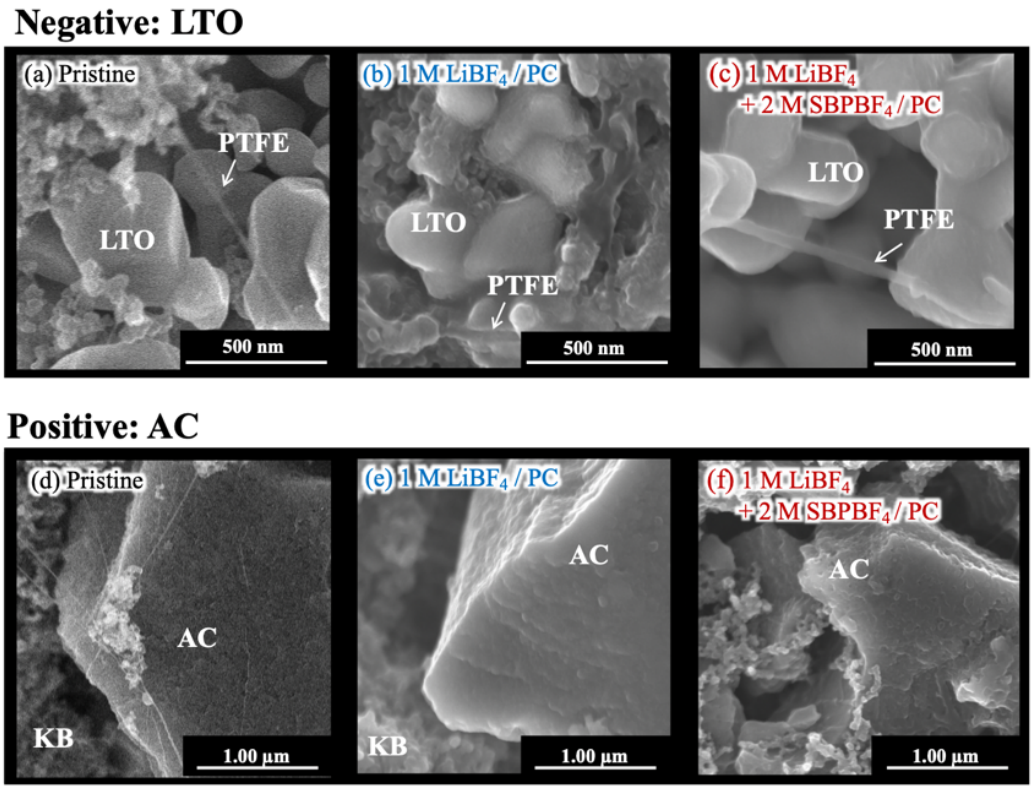

Fig. 3-5. (a)-(c) SEM images of LTO negative electrodes: **(a)** pristine LTO (before floating), and LTO after floating in **(b)** single-cation (1 M $LiBF_4$/ PC) and **(c)** dual-cation electrolytes (1 M $LiBF_4$ + 2 M $SBPBF_4$/ PC). **(d)-(f)** SEM images of AC positive electrodes: **(d)** pristine AC (before floating), and AC after floating in **(e)** single-cation and **(f)** dual-cation electrolytes.

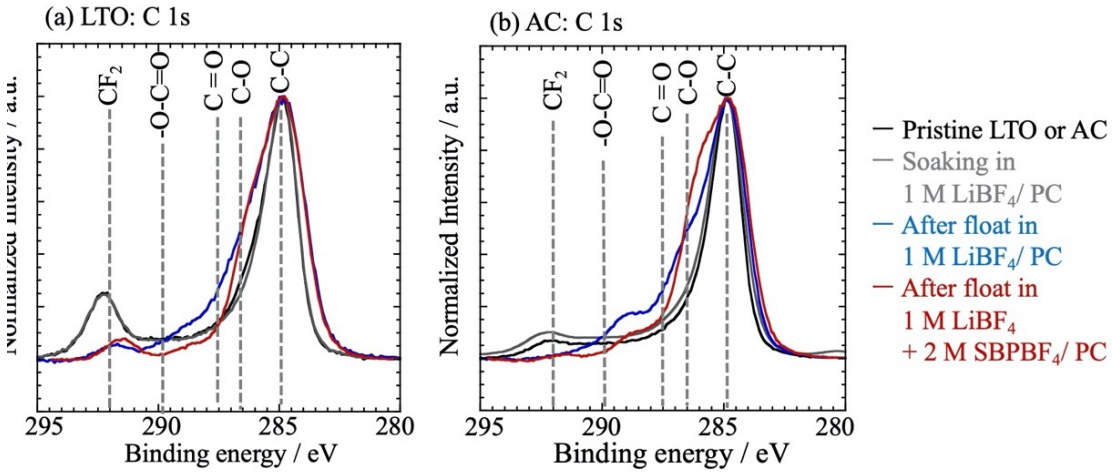

Fig. 3-6. XPS analysis of **(a)** LTO and **(b)** AC electrodes. "Soaking" refers to LTO electrodes immersed overnight in single-cation electrolyte (1 M $LiBF_4$/ PC), while "After float" refers to LTO electrodes subjected to high-voltage floating tests in single-cation or dual-cation electrolytes, as described for Fig. 3-4.

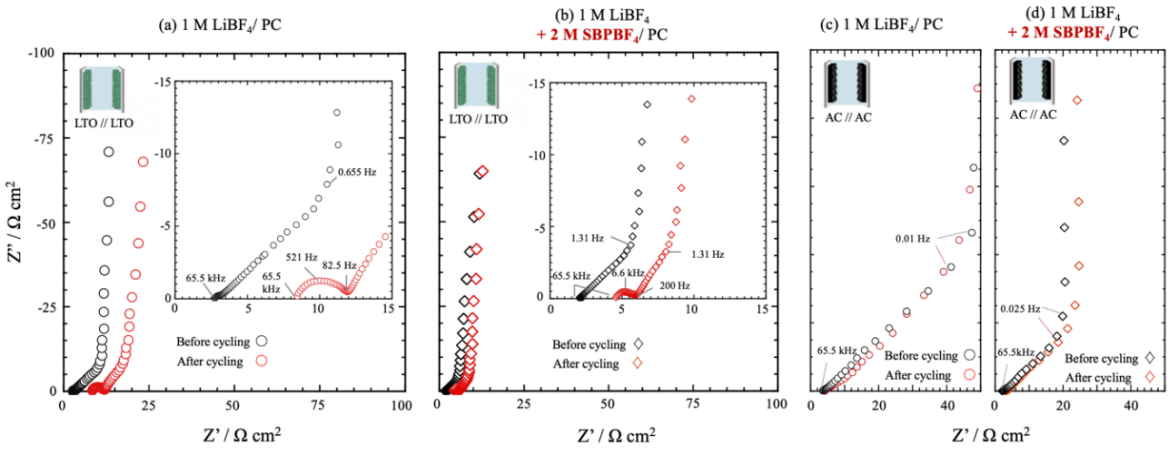

Fig. 3-7. Electrochemical impedance (EIS) spectra of symmetric cells before and after 3.2 V cycling tests; LTO//LTO for **(a)** single-cation (1 M $LiBF_4$/ PC) and **(b)** dual-cation (1 M $LiBF_4$ + 2 M $SBPBF_4$/ PC) electrolytes, and AC//AC for **(c)** single-cation and **(d)** dual-cation electrolytes. EIS measurements were carried out at OCV (fully discharged state) using a perturbation signal of +/– 10 mV within frequency ranges 0.01 Hz to 65.5 kHz and 0.001 Hz to 65.5 kHz for LTO//LTO and AC//AC, respectively.

As shown in Figs. 3-7 (a)–(b), for LTO//LTO symmetric cells, a semicircle corresponding to the accumulated SEI layer appeared for both single-cation and dual-cation electrolytes after cycling. To quantitatively compare the resistance corresponding to the accumulated SEI layer (R_{SEI}), data fitting of the EIS spectra for LTO//LTO symmetric cells obtained after cycling tests was performed, based on the equivalent circuit model shown in the inset of Fig. 3-8 (a). As shown in Fig. 3-8 and Table 3-1, the diameters of R_{SEI} and the corresponding frequencies at the top were different for the single- and dual-cation electrolytes: 3.11 and 1.31 Ω cm^2, at 521 Hz and 6.6 kHz, respectively.

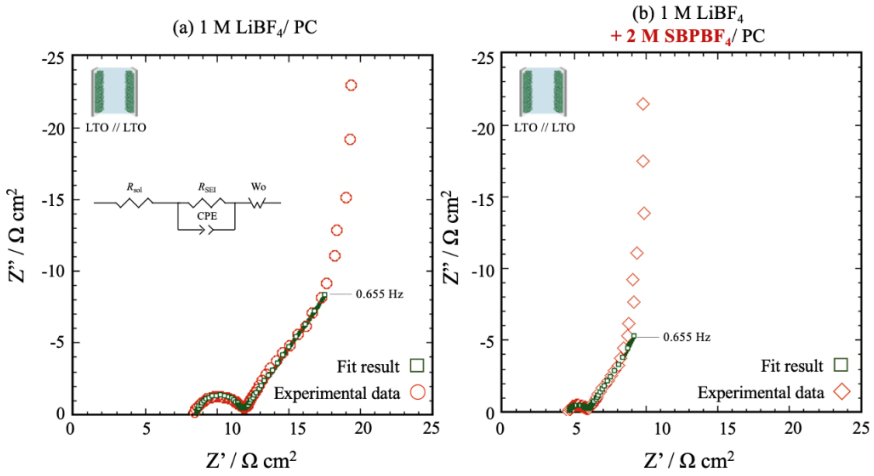

Fig. 3-8. Experimental and fitted EIS spectra for the LTO//LTO symmetric cells after cycling for **(a)** single-cation (1 M $LiBF_4$/ PC) and **(b)** dual-cation (1 M $LiBF_4$ + 2 M $SBPBF_4$/ PC) electrolytes. Inset: the equivalent circuit model used for fitting the EIS spectra of LTO//LTO symmetric cells, incorporating the bulk resistance of the solution (R_{sol}), the resistance of the SEI (R_{SEI}), a constant phase element (CPE), and a Warburg element with open terminus (Wo).

Table 3-1. EIS fitting parameters of LTO//LTO symmetric cells (after cycling tests) for single-cation (1 M $LiBF_4$/ PC) and dual-cation (1 M $LiBF_4$ + 2 M $SBPBF_4$/ PC)

electrolytes. Here, R_{sol} is the solution resistance, R_{SEI} is the SEI resistance, CPE-T has a physical meaning similar to capacitance, CPE-P (-) is a fitting parameter with no physical meaning, Wo-R (Ω cm^2) is the Warburg diffusion impedance, Wo-T (s) is a diffusion parameter (time for diffusion), and Wo-P (-) is a fitting parameter with no physical meaning.

	single-cation electrolyte (1 M $LiBF_4$/ PC)	dual-cation electrolyte (1 M $LiBF_4$ + 2 M $SBPBF_4$/ PC)
R_{sol} (Ω cm^2)	8.55	4.61
R_{SEI} (Ω cm^2)	3.11	1.31
CPE-T (F cm^{-2})†	3.81×10^{-5}	1.84×10^{-4}
CPE-P (-)	0.903	0.818
Wo-R (Ω cm^2)	52.8	26.9
Wo-T (s)	3.60	2.46
Wo-P (-)	0.609	0.638

†The CPE-T value depends on the value of CPE-P according to the definition CPE = 1/[CPE-T*(j*ω)^CPE-P]

3.3.4 Mechanism of H_2 gas suppression in the presence of $SBPBF_4$

The above-mentioned results clearly demonstrate the inhibitory effect of the dual-cation electrolyte (1 M $LiBF_4$ + 2 M $SBPBF_4$/ PC) on the reductive decomposition of PC and H_2O at the LTO negative electrode, resulting in less H_2 gas generation in LTO//AC during high-voltage operation. One may consider various candidates for the mechanism of such phenomena with the dual-cation electrolyte, including (1) the reduced molar concentration (mol dm^{-3}) of PC in the electrolyte with increasing $SBPBF_4$ concentration, and (2) the effect of $SBPBF_4$ at the LTO/electrolyte interface in slowing the decomposition of PC and H_2O. To exclude candidate mechanism (1), I complemented the experiments described in Section 3.3.2, by conducting a similar gas volume/composition analysis on LTO//AC hybrid-capacitor cells, but using three different electrolyte compositions, with the $SBPBF_4$ concentration fixed at 2.0 M and three different $LiBF_4$

concentrations (0.8, 1.0, and 2.0 M). If the inhibitory effect of $SBPBF_4$ on gas generation in the dual-cation electrolyte is based on mechanism (1), the H_2 gas volume should decrease with increasing $LiBF_4$ concentration, since the PC molar concentration then decreases. As shown in Fig. 3-9 (a), the PC molar concentration decreased from 11 to 5 mol dm^{-3} with an increase in $SBPBF_4$ concentration from 0 to 3 M in 1 M $LiBF_4$/ PC. In the case of electrolyte compositions with the $SBPBF_4$ concentration fixed at 2.0 M and different $LiBF_4$ concentrations (0.8, 1.0, and 2.0 M), the PC molar concentration decreased from 7.3 to 6.7 M with an increase of $LiBF_4$ concentration. The results are shown in Fig. 3-10: the volume of generated H_2 gas increased from 17 mL to 24 mL as the $LiBF_4$ concentration increased from 0.8 to 2.0 M, despite the reduced volume of PC solvent. Based on these findings, the effect of the reduced PC solvent volume on the suppression of H_2 gas suppression by the dual-cation electrolyte was negligible. The candidate mechanism (1) can be rejected, based on these findings; instead, mechanism (2) appears favorable, emphasizing the role of $SBPBF_4$ in inhibiting PC decomposition at the LTO/electrolyte interface.

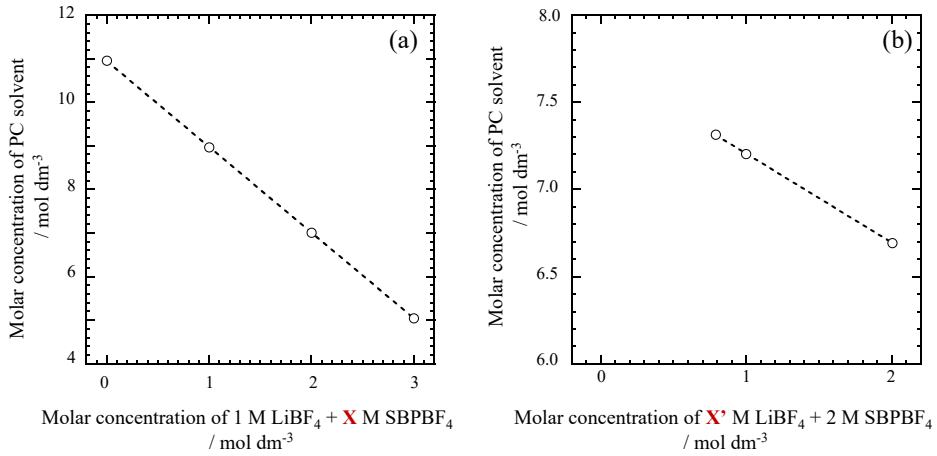

Fig. 3-9. Molar concentration of PC solvent **(a)** against progressively increased $SBPBF_4$ concentration (X M) in the electrolyte, with the $LiBF_4$ concentration fixed at 1 M; and **(b)**

against increasing $LiBF_4$ concentration (X′ M) in the electrolyte, with the $SBPBF_4$ concentration fixed at 2 M.

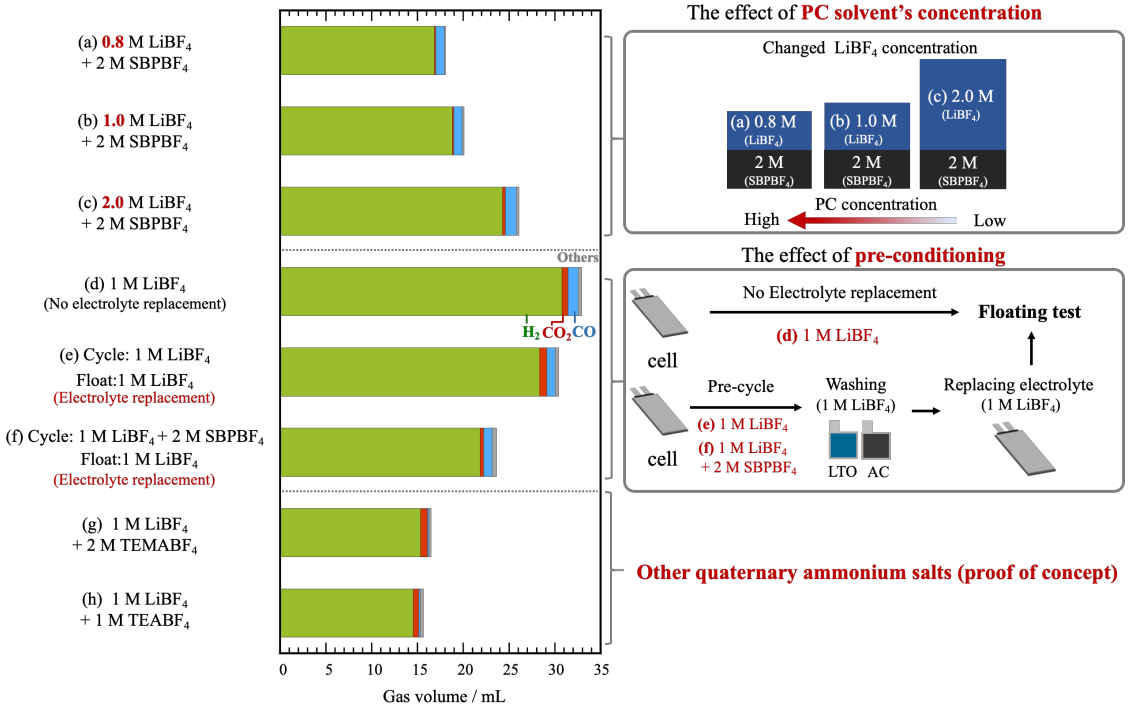

Fig. 3-10. Generated gas volumes from LTO//AC cells after floating tests under different conditions. **(a)-(c)** Different molar concentrations of PC solvent; tests on different electrolyte compositions with a fixed $SBPBF_4$ concentration (2 M) and three different $LiBF_4$ concentrations (**(a)** 0.8, **(b)** 1.0, and **(c)** 2.0 M). **(d)** and **(e)** Tests with different pre-conditions: **(d)** in 1 M $LiBF_4$/ PC without preconditioning; **(e)** pre-cycled in 1 M $LiBF_4$/ PC for 2 cycles, and floating tests then conducted after replacing the electrolyte with a fresh one; **(f)** pre-cycled in 1 M $LiBF_4$ + 2 M $SBPBF_4$ / PC for 2 cycles, and floating tests then conducted after replacing the electrolyte with 1 M $LiBF_4$/ PC. Prior to the electrolyte replacement, the pre-cycled cells were opened and washed with 1 M $LiBF_4$/ PC several times before re-sealing. **(g)** and **(h)** Tests with alternative quaternary ammonium salts: **(g)** 1 M $LiBF_4$ + 2 M $TEMABF_4$/ PC and **(h)** 1 M $LiBF_4$ + 1 M $TEABF_4$/ PC.

Regarding mechanism (2), it has been reported that the catalytic effect of the Lewis acid sites on the LTO surface, which are dangling bonds or surface hydroxy groups, promotes the decomposition of PC solvent molecules at the LTO electrode/electrolyte interfaces, resulting in H_2 gas generation.[6, 15] Physically blocking or neutralizing such Lewis acid sites by applying a coating (carbon,[16] ZnO,[17] or AlF_3 [18]), adjusting the electrolyte composition,[12] or using electrolyte additives (vinylene carbonate,[19] succinonitrile,[20] or Schiff base compounds [21]) has been investigated as a means to suppress their reactivity and thereby reduce H_2 gas generation. Taking as a hypothesis the passivation effect of $SBPBF_4$ on the Lewis acid sites on the LTO surface in the dual-cation electrolyte, I conducted another model floating test on LTO//AC hybrid capacitors, using three different preconditioning approaches, as shown in Fig. 3-10 (d)-(f): i) using no preconditioning (no electrolyte replacement, Fig. 3-10 (d)); ii) replacing the electrolyte with a fresh single-cation electrolyte after pre-cycling in the single-cation electrolyte (Fig. 3-10 (e)); and iii) replacing the electrolyte with a fresh single-cation electrolyte after pre-cycling in the dual-cation electrolyte (Fig. 3-10 (f)). Note that a gas volume reduction of ~ 3 mL was observed after simply replacing of the electrolyte with a fresh one, as shown in Figs. 3-10 (d) and (e). Nevertheless, a considerable reduction in the gas volume from ~ 9 mL was observed for the cells pre-cycled in the dual-cation electrolyte, as shown in Fig. 3-10 (f). The retention of the passivation effect even after electrolyte replacement with the single-cation electrolyte indicates the formation of an $SBPBF_4$-derived film on the LTO surface during pre-cycling in the dual-cation electrolyte. The possible formation mechanism of the $SBPBF_4$-derived film, based on electrochemically induced Hofmann elimination, is described in Scheme 3-1 and Fig. 3-11. During lithiation, impurity-level H_2O released from the AC positive electrode is easily reduced on the LTO surface to

produce H_2 and OH^-. Then, OH^- may chemically react with SBP^+, which is a quaternary ammonium cation, resulting in decomposition to a Lewis-base amine [1-(3-butenyl)pyrrolidine].

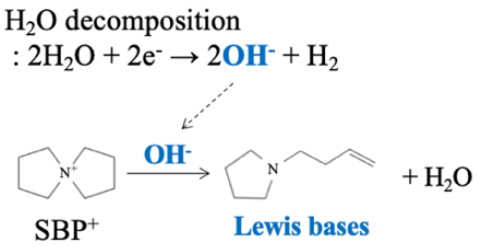

Scheme 3-1: Possible mechanism of Hofmann elimination of SBP^+.

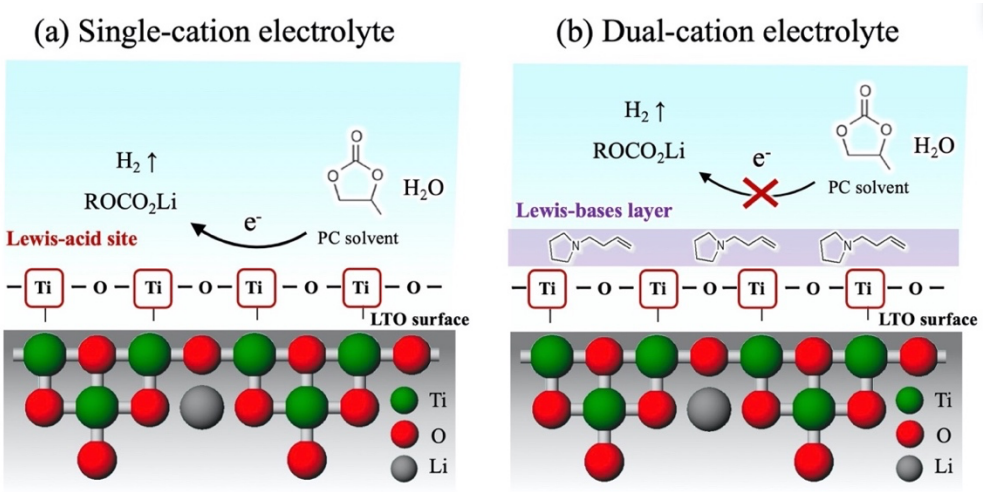

Fig. 3-11. Schematic illustrations of **(a)** gas-generation mechanism at the LTO surface for the single-cation electrolyte (1 M $LiBF_4$/ PC), and **(b)** passivation mechanism of the catalytic LTO surface in the dual-cation electrolyte (1 M $LiBF_4$ + 2 M $SBPBF_4$/ PC).

I further used XPS to investigate the surface composition change before and after preconditioning with $SBPBF_4$. The detailed experimental conditions for the XPS measurements are described in the experimental section (Section 3.2.5). Fig. 3-12 shows the nitrogen 1s XPS spectra of the LTO surface before and after two pre-cycles using the dual-cation electrolyte (1 M $LiBF_4$ + 2 M $SBPBF_4$ in PC). A clear peak attributed to the

amine group $N(C)_3$ [22] appeared around 402.5 eV on the LTO surface after pre-cycling, in contrast to the pristine LTO electrodes. The results indicate the formation of a Lewis-base layer composed of amine compounds, such as 1-(3-butenyl)pyrrolidine, derived from the decomposition of SBP^+ on the LTO surface, which may effectively passivate the Lewis acid sites on the LTO surface and suppress its activity in the reductive decomposition of PC.

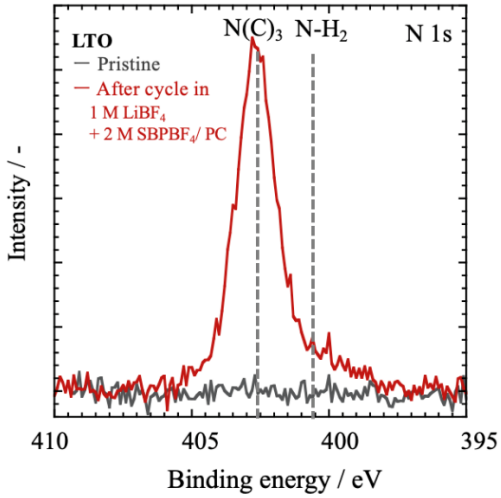

Fig. 3-12. XPS spectra of the N1s on the LTO surface before (pristine) and after pre-cycling in LTO//AC cells using the dual-cation electrolyte (1 M $LiBF_4$ + 2 M $SBPBF_4$/ PC). The pre-cycling was conducted at a current density of 0.1 mA cm^{-2} with a cell voltage range between 0 and 3 V for two cycles.

Aside from the suppression of PC decomposition, passivation of the LTO may also hinder the reductive decomposition of H_2O, which is another resource for H_2 production. To investigate the suppression of the reductive decomposition of H_2O in the dual-cation electrolyte, another high-voltage floating test was conducted by adding an excess amount of H_2O into the single-cation (1 M $LiBF_4$/ PC) and dual-cation (1 M $LiBF_4$ + 2 M $SBPBF_4$/ PC) electrolytes. The H_2O content of the electrolyte was maintained at 6000 ppm, and the

same experimental conditions as those described in Section 3.2.4 were used in the floating tests. The addition of excess H_2O brought about an increase in the generated gas volume for both electrolytes, from 32.9 to 38.5 mL for the single-cation and from 21.2 mL to 24.5 mL for the dual-cation electrolyte, as shown in Fig. 3-13. Evidently, the additional gas component was derived from the reductive decomposition of excess H_2O, as the additional gas was composed of more than 98% H_2. The changes in gas volume before and after adding excess H_2O were different between the two electrolytes: 5.6 mL for the single-cation and 3.3 mL for the dual-cation electrolyte, showing that the dual-cation electrolyte reduced *ca*. 40% of H_2O reductive decomposition compared to the single-cation electrolyte. Accordingly, the remaining H_2O content in the electrolytes after the floating tests was larger for the dual-cation electrolyte (3342 ppm) than for the single-cation electrolyte (2377 ppm).

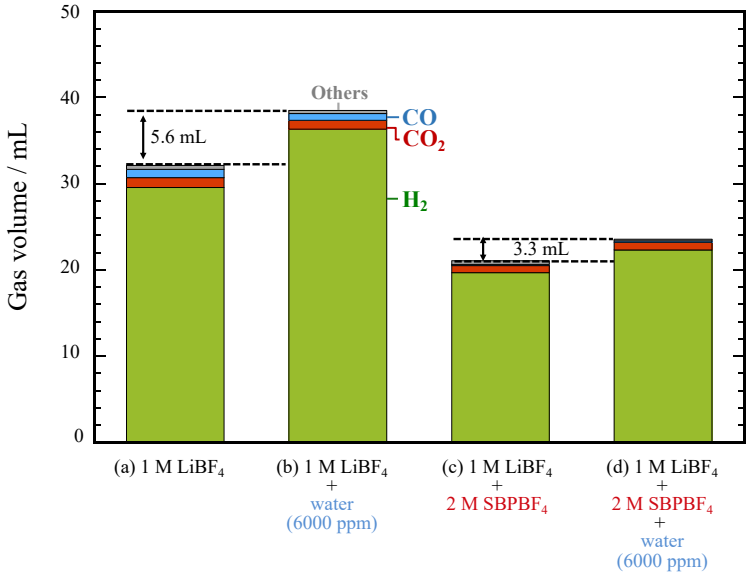

Fig. 3-13. Generated gas volumes from LTO//AC cells after floating tests. **(a)** and **(b)** Single-cation electrolyte (1 M $LiBF_4$/ PC): **(a)** before and **(b)** after addition of excess water (6000 ppm); **(c** and **d)** dual-cation electrolyte (1 M $LiBF_4$ + 2 M $SBPBF_4$/ PC): **(c)**

before and **(d)** after addition of excess water (6000 ppm). The floating conditions were the same as those described for Fig. 3-4.

3.3.5 Effect of the Lewis-base component to suppress H_2 gas generation

The possible formation mechanism of the $SBPBF_4$-derived film, based on electrochemically induced Hofmann elimination, is described in Scheme 3-1 and Fig. 3-6. Here, I propose the passivation of the LTO surface by the Lewis-base amine compound [1-(3-butenyl)pyrrolidine] derived from the decomposition of SBP^+. The passivation compound neutralized the Lewis acid sites on the LTO surface and thereby slowed the catalytic PC decomposition. If this hypothesis is correct, it should be possible to reproduce the effect of adding $SBPBF_4$ to an electrolyte by directly adding appropriate Lewis-base molecules instead. Thus, we prepared a test electrolyte by adding 1 wt.% of triethylamine (Et_3N, Kishida Chemicals, Japan), a compound analogous to 1-(3-butenyl)pyrrolidine, to the single-electrolyte (1 M $LiBF_4$/ PC), then repeated the floating test of Section 3.3.2 for the cells, using the prepared electrolyte. Note that the addition of Et_3N did not affect the ionic conductivity (single-cation electrolyte: 3.4 mS cm^{-1}; test electrolyte with the addition of 1 wt.% Et_3N: 3.2 mS cm^{-1}), in contrast to the dual-cation case (1 M $LiBF_4$ + 2 M $SBPBF_4$/ PC: 7.8 mS cm^{-1}). Fig. 3-14 shows the measured volume of gas generated from such a cell after a floating test at 3.5 V; for comparison, the figure also replots the data of Fig. 3-4 for the single-cation electrolyte (1 M $LiBF_4$/ PC). When Et_3N was added to the single-cation electrolyte, the generated gas volume (18 mL) was nearly half of that for the system without Et_3N (33 mL). These findings confirm that the addition of Lewis bases significantly reduces gas generation, validating our hypothesis. However, the dependence of the gas-generation inhibitory effect on the $SBPBF_4$ concentration, shown in Fig. 3-4, indicates that the continuous presence of SBP^+ in the

electrolyte also plays an important role in the gas reduction. This may be because SBP^+ in the bulk electrolyte 1) continuously restores the SBP^+-derived passivation layer on the LTO surface, similarly to reported additives such as fluoroethylene carbonate, which is continuously consumed to protect the surface of silicon-based electrodes in lithium-ion battery systems;[23] 2) blocks the approach of impurities and oxidative-decomposition compounds arising from the AC positive electrode by trapping them.[24]

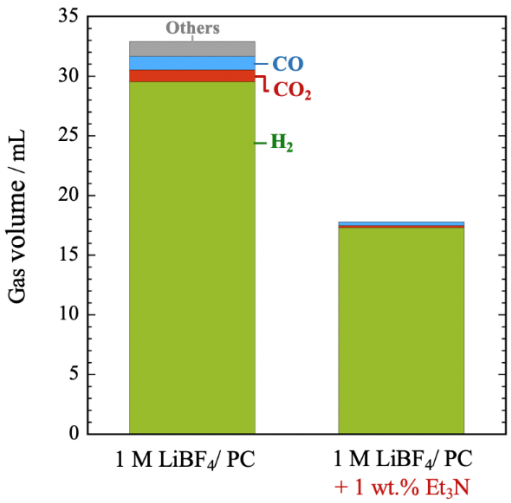

Fig. 3-14. Generated gas volumes from LTO//AC cells using the single-cation electrolyte (1 M $LiBF_4$/ PC) with and without 1 wt.% of the Lewis basis Et_3N after floating tests at 3.5 V for 200 hours at 60 °C (Others: CH_4, C_2H_4, and C_2H_6).

To support the proposed gas-inhibition mechanism, alternative quaternary ammonium-based electrolytic salts were investigated to determine whether the same effect could be observed. $TEMABF_4$ and $TEABF_4$ were chosen to prepare alternative dual-cation electrolytes, as both salts have been used in conventional EDLC devices.[25-26] The results (Figs. 3-10 (g) and (h)) indicate that cells prepared using the two alternative electrolytes exhibit gas-reduction properties comparable to or even greater than those

observed for $SBPBF_4$. This difference could be attributed to variation in the stability of the quaternary ammonium salts presenting varying steric barriers to the Hofmann elimination, making $TEMA^+$ and TEA^+ more susceptible to decomposition than SBP^+ and thus enriching the LTO surface with Lewis-base amine compounds. Nevertheless, the results show another example of gas inhibition by dual-cation electrolytes containing quaternary ammonium salts.

3.4 Conclusion

In this work, I have investigated the application of $SBPBF_4$-based dual-cation electrolytes in the design of LTO//AC hybrid capacitors. In comparison with conventional cells based on single-cation electrolytes, fuel cells made with dual-cation electrolytes exhibited significantly reduced H_2 gas generation after floating tests at 3.5 V and 60 °C. A series of detailed experimental analyses revealed that the addition of $SBPBF_4$ inhibited decomposition of the PC solvent and reduced sediment deposits, thereby reducing H_2 gas generation. I have proposed a mechanism for this reduction, in which Lewis-base molecules produced by decomposition of $SBPBF_4$ inhibit the decomposition of PC and H_2O at the LTO negative electrode. Dual-cation electrolytes solve simultaneously the problems of gas generation at high output power density and of high-voltage operation, making them highly promising new electrolytes for LTO//AC.

3.5 References

1. Amatucci, G. G.; Badway, F.; Du Pasquier, A.; Zheng, T., An asymmetric hybrid nonaqueous energy storage cell. *Journal of The Electrochemical Society* **2001,** *148* (8), A930-A939.
2. Muzaffar, A.; Ahamed, M. B.; Deshmukh, K.; Thirumalai, J., A review on recent advances in hybrid supercapacitors: Design, fabrication and applications. *Renewable and Sustainable Energy Reviews* **2019,** *101*, 123-145.
3. Yuan, T.; Tan, Z.; Ma, C.; Yang, J.; Ma, Z. F.; Zheng, S., Challenges of Spinel $Li_4Ti_5O_{12}$ for Lithium‐Ion Battery Industrial Applications. *Advanced Energy Materials* **2017,** *7* (12), 1601625.
4. Naoi, K.; Naoi, W.; Aoyagi, S.; Miyamoto, J.-i.; Kamino, T., New generation "nanohybrid supercapacitor". *Accounts of chemical research* **2013,** *46* (5), 1075-1083.
5. Yang, J.-J.; Choi, C.-H.; Seo, H.-B.; Kim, H.-J.; Park, S.-G., Voltage characteristics and capacitance balancing for $Li_4Ti_5O_{12}$/activated carbon hybrid capacitors. *Electrochimica Acta* **2012,** *86*, 277-281.
6. Iwama, E.; Ueda, T.; Ishihara, Y.; Ohshima, K.; Naoi, W.; Reid, M. T. H.; Naoi, K., High-voltage operation of $Li_4Ti_5O_{12}$/AC hybrid supercapacitor cell in carbonate and sulfone electrolytes: Gas generation and its characterization. *Electrochimica Acta* **2019,** *301*, 312-318.
7. Fleischmann, S.; Widmaier, M.; Schreiber, A.; Shim, H.; Stiemke, F. M.; Schubert, T. J.; Presser, V., High voltage asymmetric hybrid supercapacitors using lithium-and sodium-containing ionic liquids. *Energy Storage Materials* **2019,** *16*, 391-399.
8. Chikaoka, Y.; Iwama, E.; Ueda, T.; Miyashita, N.; Seto, S.; Sakurai, M.; Naoi, W.; Reid, M. T. H.; Simon, P.; Naoi, K., Dual-Cation Electrolytes for High-Power and High-Energy LTO//AC Hybrid Capacitors. *The Journal of Physical Chemistry C* **2020**.
9. Azais, P.; Tamic, L.; Huitric, A.; Paulais, F.; Rohel, X. Separator film, its fabrication method, supercapacitor, battery and capacitor provided with said film, U.S. Patent 9,461,288. 4 Oct. U.S. Patent 9,461,288., 2016.
10. Okita, N.; Iwama, E.; Tatsumi, S.; VÕ, T. N. H.; Naoi, W.; Reid, M. T. H.; Naoi, K., Prolonged Cycle Life for $Li_4Ti_5O_{12}$//[$Li_3V_2(PO_4)_3$/Multiwalled Carbon Nanotubes] Full Cell Configuration *via* Electrochemical Preconditioning. *Electrochemistry* **2019,** *87* (3), 148-155.
11. Qiao, L.; Cui, Z.; Chen, B.; Xu, G.; Zhang, Z.; Ma, J.; Du, H.; Liu, X.; Huang, S.; Tang, K., A promising bulky anion based lithium borate salt for lithium metal batteries. *Chemical science* **2018,** *9* (14), 3451-3458.

12. Wu, K.; Yang, J.; Liu, Y.; Zhang, Y.; Wang, C.; Xu, J.; Ning, F.; Wang, D., Investigation on gas generation of $Li_4Ti_5O_{12}$/$LiNi_{1/3}Co_{1/3}Mn_{1/3}O_2$ cells at elevated temperature. *Journal of Power Sources* **2013,** *237*, 285-290.
13. Ding, M.; Liu, H.; Zhao, X.; Pang, L.; Deng, L.; Li, M., Composite with TiO_2 and extension of discharge voltage range for capacity enhancement of a $Li_4Ti_5O_{12}$ battery. *RSC Advances* **2017,** *7* (69), 43894-43904.
14. Brevnov, D. A.; Olson, T. S., Double-layer capacitors composed of interconnected silver particles and with a high-frequency response. *Electrochimica Acta* **2006,** *51* (7), 1172-1177.
15. Wang, Y.; Zhao, J.; Qu, J.; Wei, F.; Song, W.; Guo, Y.-G.; Xu, B., Investigation into the surface chemistry of $Li_4Ti_5O_{12}$ nanoparticles for lithium ion batteries. *ACS applied materials & interfaces* **2016,** *8* (39), 26008-26012.
16. Wen, L.; Wu, Z.; Luo, H.; Song, R.; Li, F., Dual functions of carbon in $Li_4Ti_5O_{12}$/C microspheres. *Journal of The Electrochemical Society* **2014,** *162* (2), A3038.
17. Han, C.; He, Y.-B.; Li, H.; Li, B.; Du, H.; Qin, X.; Kang, F., Suppression of interfacial reactions between $Li_4Ti_5O_{12}$ electrode and electrolyte solution *via* zinc oxide coating. *Electrochimica Acta* **2015,** *157*, 266-273.
18. Li, W.; Li, X.; Chen, M.; Xie, Z.; Zhang, J.; Dong, S.; Qu, M., AlF_3 modification to suppress the gas generation of $Li_4Ti_5O_{12}$ anode battery. *Electrochimica Acta* **2014,** *139*, 104-110.
19. Bouayad, H.; Wang, Z.; Dupre, N.; Dedryvère, R.; Foix, D.; Franger, S.; Martin, J.-F.; Boutafa, L.; Patoux, S.; Gonbeau, D., Improvement of electrode/electrolyte interfaces in high-voltage spinel lithium-ion batteries by using glutaric anhydride as electrolyte additive. *The Journal of Physical Chemistry C* **2014,** *118* (9), 4634-4648.
20. Gao, J.; Gong, B.; Zhang, Q.; Wang, G.; Dai, Y.; Fan, W., Study of the surface reaction mechanism of $Li_4Ti_5O_{12}$ anode for lithium-ion cells. *Ionics* **2015,** *21* (9), 2409-2416.
21. Daigle, J.-C.; Asakawa, Y.; Hovington, P.; Zaghib, K., Schiff base as additive for preventing gas evolution in $Li_4Ti_5O_{12}$-based lithium-ion battery. *ACS applied materials & interfaces* **2017,** *9* (47), 41371-41377.
22. Yang, C.-H.; Huang, P.-L.; Luo, X.-F.; Wang, C.-H.; Li, C.; Wu, Y.-H.; Chang, J.-K., Holey graphene nanosheets with surface functional groups as high-performance supercapacitors in ionic-liquid electrolyte. *ChemSusChem* **2015,** *8* (10), 1779-1786.
23. Jung, R.; Metzger, M.; Haering, D.; Solchenbach, S.; Marino, C.; Tsiouvaras, N.; Stinner, C.; Gasteiger, H. A., Consumption of fluoroethylene carbonate (FEC) on Si-

C composite electrodes for Li-ion batteries. *Journal of The Electrochemical Society* **2016,** *163* (8), A1705.

24. Sugihara, R.; Watanabe, K.; Tsumeda, S.; Ishimoto, S. Power storage device composition, power storage device separator using power storage device composition, and power storage device, U.S. Patent 20200203691, 26 Jun. 2018.

25. Chiba, K.; Ueda, T.; Yamamoto, H., Performance of electrolyte composed of spiro-type quaternary ammonium salt and electric double-layer capacitor using it. *Electrochemistry* **2007,** *75* (8), 664-667.

26. Nambu, N.; Takahashi, R.; Takehara, M.; Ue, M.; Sasaki, Y., Electrolytic characteristics of fluoroethylene carbonate for electric double-layer capacitors at high concentrations of electrolyte. *Electrochemistry* **2013,** *81* (10), 817-819.

Section 4. Charge–discharge Simulation of Li_3VO_4//$Li_3V_2(PO_4)_3$ Full-Cell via Negative/Positive Capacity Ratio and Suppressing Irreversible Reactions with Vinylene Carbonate

4.1 Introduction

In response to growing concerns over environmental problems and to service a sustainable society, the demand for high-power electric energy storage (EES) devices for grid storage continues to increase. An example of high-power EES devices is the electric double-layer capacitor (EDLC) or supercapacitor (SC), which is characterized by its safety and extremely long cycle life. However, compared with batteries, the energy density and cell voltage of EDLCs are limited because their charge-storage mechanism entails ionic adsorption on the surface of activated carbon (AC) electrodes.[1-2] Hybrid/asymmetric capacitors are 2nd generation (2nd gen.) SCs and were developed to improve the voltages and energy densities of EDLCs; specifically, one of the AC electrodes is replaced with battery materials (prominently lithium-ion battery (LIB) materials) that exhibit high power and high cyclability.[3-5] To further improve the energy densities of hybrid capacitors while maintaining their high power and cyclability, it is inevitable that the remaining AC electrode is replaced with another battery material exhibiting ultrafast electrochemical characteristics; thus, LIBs with capacitor-like characteristics are constructed, which are herein denoted as SuperRedox Capacitors (SRCs), a 3rd gen. SC.[6] Depending on the combination of active materials,[6] SRC may achieve different maximum cell voltages (2.8−3.5 V) and energy densities (fold-change of 5.4−5.7 from EDLC, Fig. 4-1).

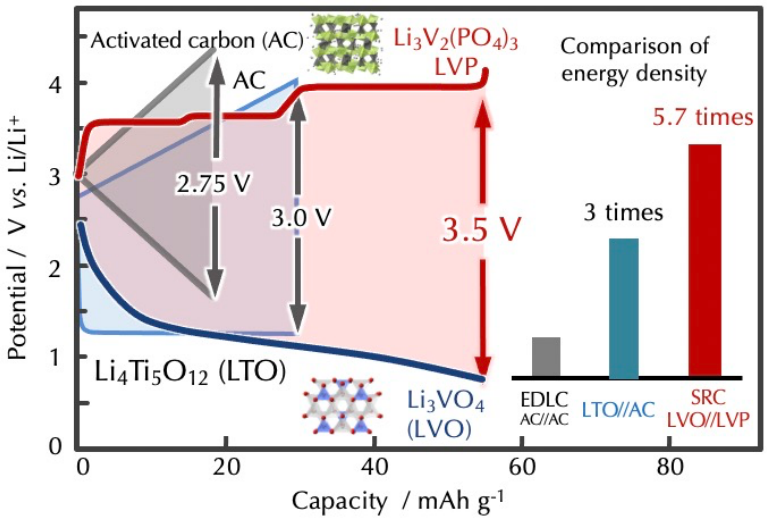

Fig. 4-1. Comparison of energy density of each capacitor (EDLC: AC//AC, hybrid capacitor: LTO//AC, and SuperRedox Capacitor: LVO//LVP)

One of the promising combinations of active materials for SRCs is lithium vanadate (Li_3VO_4, LVO) as the negative electrode and lithium vanadium phosphate ($Li_3V_2(PO_4)_3$, LVP) as the positive electrode, denoted as LVO//LVP. LVO has attracted significant attention as a negative electrode material because of its lower reaction potential and higher theoretical capacity compared with those of typical Ti-based negative electrode materials, such as $Li_4Ti_5O_{12}$ (LTO) (*ca*. 1.55 V *vs.* Li/Li^+, 175 mAh g^{-1}).[7-9] The redox reactions of LVO (V^{5+}/V^{3+}) lies in a safe potential range of 0.4–1.3 V *vs.* Li/Li^+ and show reversible lithiation/delithiation with a capacity of 197 mAh g^{-1} (equivalent to 1.0 Li insertion) and 394 mAh g^{-1} (equivalent to 2.0 Li insertion).[10-12] LVP is a polyanionic positive electrode material characterized by strong PO_4 bonds, which confer excellent thermal stability compared with other common positive electrode materials, such as $LiCoO_2$.[13] The inductive effect of PO_4 increases the LVP reaction potential (3.6−4.1 V *vs.* Li/Li^+), where the reversible insertion/deinsertion of 2.0 Li occurs with a theoretical

capacity of 131 mAh g^{-1}.[10-12] The three dimensional diffusion of Li^+ in LVP results in a higher lithium-ion diffusion coefficient (10^{-10} cm^2 s^{-1}) than those of other polyanion-type positive materials, such as $LiFePO_4$ (10^{-13} cm^2 s^{-1}).[12, 14] Nevertheless, both LVO and LVP have inherent disadvantages that prevent them from achieving high power capabilities, including low electrical conductivity (LVO < 10^{-10} Ω^{-1} cm^{-1}, LVP = 10^{-7}–10^{-8} Ω^{-1} cm^{-1}) and large charge–discharge potential hysteresis (LVO < 500 mV).[8] To overcome such inherent disadvantages and enhance the power capability of LVO negative and LVP positive electrodes, several approaches have been reported, such as nanosizing (5–100 nm), carbon coating, and metal doping.[9, 15-18] Previously, Naoi *et al* successfully synthesized nanocomposites of LVO and LVP with multi-walled carbon nanotubes (MWCNTs) *via* a unique ultracentrifugation (uc) treatment, which can produce highly dispersed metal oxide nanoparticles within a nanocarbon matrix.[8, 12] Both uc-treated LVO and uc-treated LVP showed excellent power capability (> 50% capacity retention even at a high current density of 20 A g^{-1}) and high cyclability (90% capacity retention of the initial cycle over 4000 cycles).[8, 12]

In a full cell composed of an LVP positive electrode, an important issue to consider is the limited cycling performance because the small amount of eluted vanadium from LVP can be deposited on the opposite anodic electrode, and the deposited vanadium may catalytically accelerate electrolyte reductive decomposition. The mechanism of capacity degradation attributed to the eluted vanadium was elucidated for full cells composed of LVP, namely LTO//LVP,[19] by directly detecting the vanadium species on the LTO negative electrode surface *via* inductivity coupled plasma (ICP) and X-ray photoelectron spectroscopy (XPS). Similar degradation mechanisms may be predicted for LVO//LVP full cells; however, the detection of such vanadium species becomes difficult when the

negative electrode is composed of the same vanadium-based material as that of LVP. Therefore, in this study, charge–discharge cycle simulation was utilized as an "indirect" analysis method [20-21] and as an alternative to the direct detection of vanadium species.

In this study, to elucidate the capacity degradation mechanism of LVO//LVP full cell cycling, simple charge–discharge simulations were applied based on the difference in Coulombic efficiency (*CE*) between the negative and positive electrodes with/without capacity decay at the electrode materials. Prior to the simulation, experimental data were collected of full cell cycling at different values of the negative and positive electrode capacity ratio (N/P capacity ratio). Then, different simulation patterns were performed and compared with experimental data. Here, the focus was simply the direction of potential shift in the simulated charge–discharge curves. After successfully identifying the capacity decay of LVO as a factor for the capacity degradation of full cells, additional experimental data, such as scanning electron microscopy (SEM) images, were collected to support the assumptions derived from the simulation. Furthermore, vinylene carbonate (VC) was chosen as an electrolyte additive to mitigate LVO capacity decay by facilitating the formation of a stable film on the LVO negative electrode, thus demonstrating the credibility and effectiveness of the developed simple cycling simulation. These findings can assist with the elucidation of the degradation mode of full cell cycling and provide insights for the development of strategies that mitigate capacity degradation.

4.2 Experimental

4.2.1 Electrode preparation

LVO/MWCNTs (60:40 wt.%) were used as the negative electrode and LVP/MWCNTs (70:30 wt.%) were used as the positive electrode; they were prepared

using the method developed in previous studies.[8, 12] Successful synthesis of both active materials was verified based on their diffraction peaks, carbon weight, and electrochemical properties by using X-ray diffraction, thermogravimetric analysis, and charge–discharge tests in half-cells, respectively. The LVO/MWCNTs negative electrodes were prepared by mixing 94 wt.% of the composite and 6 wt.% of polyvinylidene difluoride (PVdF, Kureha Industries) in *n*-methylpyrrolidone (NMP, FUJIFILM Wako Pure Chemical Co.), and the mixture was then coated onto etched-Cu foil. The LVP/MWCNTs positive electrodes were prepared by mixing 90 wt.% of the composite and 10 wt.% of PVdF in NMP, and the mixture was then coated onto etched-Al foil. Both coated electrodes were dried at 80 °C under vacuum for 12 h. Prior to cell assembly, the electrodes were further dried at 80 °C for 3 h under vacuum. Three different loading masses of the LVO negative electrode were used to control the N/P capacity ratio. For the full cells with N/P capacity ratios of 1.1, 1.4, and 1.8, the LVO/MWCNTs loading masses were *ca*. 0.65, 0.80, and 1.1 mg cm^{-2} with thicknesses of *ca*. 12, 16, and 22 μm, respectively. The LVP/MWCNTs loading mass was approximately 1.15 mg cm^{-2} with a thickness of 15 μm. The variations in cell potentials with respect to the N/P capacity ratio are described in Section 4.2.3.

4.2.2 Cell assembly

The LVO//LVP full cells were assembled using the LVO negative electrode and LVP positive electrode in laminate-type cells with a Li metal reference electrode. The electrode areas of the half-cells (coin-type) and full cells (laminate-type) were 1.54 and 5.0 cm^2, respectively. The electrolyte was an EC:DEC (1:1 vol%) mixture containing 1.0 mol L^{-1} $LiPF_6$ (battery grade, Kishida Chemical Co.) with or without 5 wt.% VC (battery grade,

Kishida Chemical Co.), and a 25-μm-thick monolayer polypropylene separator (Celgard2400, Celgard Co.) was used. Prior to full cell cycling, electrochemical pre-conditioning (including Li^+ pre-doping) of the LVO negative and LVP positive electrodes was conducted through initial charge–discharge cycling. The cell capacity of the LVO//LVP full cells was LVP-limited, corresponding to 74 mAh g^{-1} per LVP composite (1C-rate = 74 mA g^{-1} per LVP composite). The 2032 coin-type half-cells (Li//LVO and Li//LVP) were assembled to check the exhibited capacity of the active materials. Both the laminated and coin-type cells were assembled in a dry room (dew-point temperature < −40 °C).

The pre-conditioning procedure was as follows: LVO was (i) charged and discharged in the CC mode between 2.5–0.1 V *vs.* Li/Li^+ for 20 cycles at 300 mA g^{-1} and then (ii) charged in the CC mode to 1.4 V (N/P = 1.1), 1.25 V (N/P =1.4), 1.1 V (N/P = 1.8) *vs.* Li/Li^+. Concurrently, LVP underwent pre-cycling using an additional Li metal in the cell as follows: LVP was (i) charged in the CC-CV mode with a cut-off potential of 4.3 V *vs.* Li/Li^+ and holding time of 1 h, (ii) rested for 24 h, (iii) discharged to 2.5 V *vs.* Li/Li^+ in the CC mode, and then (iv) charged and discharged in the CC mode between 2.5–4.3 V *vs.* Li/Li^+ for 10 cycles at 1C-rate (131 mA g^{-1}). After the electrochemical pre-conditioning process, the full cell packages were opened to remove the Li metal electrodes, and the re-sealed full cells were cycled thereafter.

4.2.3 Charge–discharge conditions

The charge–discharge conditions of the LVO//LVP full cells varied with respect to the N/P capacity ratios, as shown in Fig. 4-2. Here, N/P = 1 when the potential ranges of LVO and LVP lied within 0.6–2.5 V and 3.35–4.1 V *vs.* Li/Li^+, respectively. It should be

noted that the potential of LVO (2.5–0.6 V *vs.* Li/Li^+), corresponding to 1.5-electron reactions (145 mAh g^{-1}), was determined to reduce the effect of the charge–discharge hysteresis (from 100 to 250 mV), which gradually increased between the two-electron reaction (0.76–0.10 V *vs.* Li/Li^+) and the one-electron reaction (2.5–0.76 V *vs.* Li/Li^+). In these potential regions, the reaction of LVO can be described as follows:[7]

$$Li_3VO_4 + 1.5\ Li^+ + 1.5\ e^- \rightleftarrows Li_{(4.5)}VO_4 \quad (4\text{-}1)$$

The potential of the LVP positive electrode (3.35–4.1 V *vs.* Li/Li^+) with 74 mAh g^{-1} (per LVP composite) was determined to prevent the three-electron reaction (approximately > 4.5 V *vs.* Li/Li^+), which causes LVP degradation during full cell operation.[11, 22] For LVP, three-step plateau regions should be observed for the 0.5 Li^+ (3.60 V), 1.0 Li^+ (3.65 V), and 2.0 Li^+ (4.05 V) reactions according to Equations (4-2), (4-3), and (4-4), respectively:[23]

$$Li_{2.5}V_2(PO_4)_3 + 0.5\ Li^+ + 0.5\ e^- \rightleftarrows Li_3V_2(PO_4)_3 \quad (4\text{-}2)$$

$$Li_2V_2(PO_4)_3 + 0.5\ Li^+ + 0.5\ e^- \rightleftarrows Li_{2.5}V_2(PO_4)_3 \quad (4\text{-}3)$$

$$LiV_2(PO_4)_3 + Li^+ + e^- \rightleftarrows Li_2V_2(PO_4)_3 \quad (4\text{-}4)$$

The lower voltage changed to 1.90, 2.05, and 2.25 V when the N/P capacity ratio was respectively varied to 1.1, 1.4, and 1.8, whereas the upper voltage of the LVO//LVP full cell remained at 3.5 V. Accordingly, only the LVO upper limit potential (*LVO MaxV*) varied with different N/P capacity ratios, as shown in the inset table of Fig. 4-2 (a). An example of the potential curves at N/P =1.1 is shown in Fig.4-2 (b).

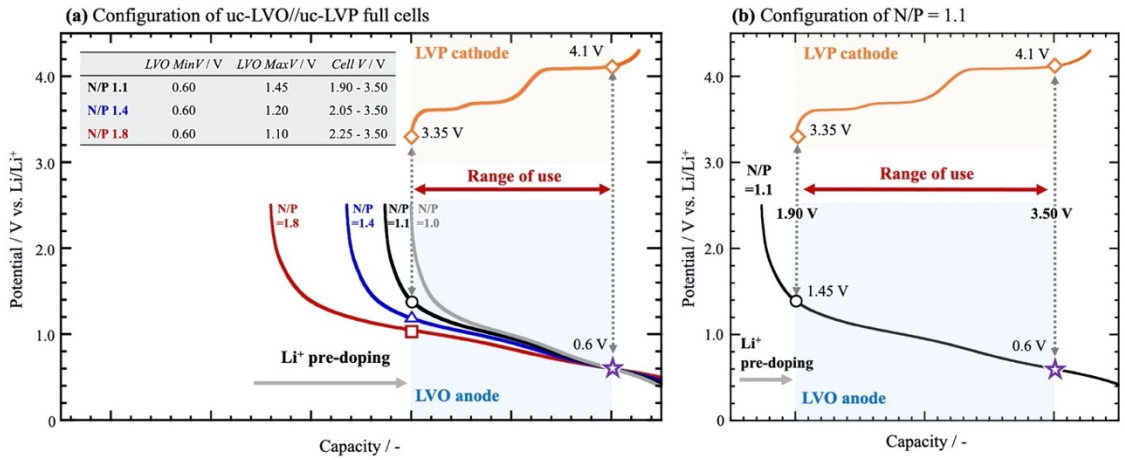

Fig. 4-2. (a) Potential curves of LVO and LVP in the LVO//LVP full cell configuration at N/P capacity ratios of 1.1, 1.4, and 1.8. **(b)** Potential curves of LVO and LVP at N/P = 1.1 LVO//LVP full cell. **[Inset table]** *LVO MinV* is the lowest potential of the LVO charge curve (☆: N/P = 1.1, 1.4, and 1.8), *LVO MaxV* is the highest potential of the LVO charge curve (○: N/P = 1.1, △: N/P = 1.4, and □: N/P = 1.8), and *Cell V* corresponds to the potential difference between the LVO and LVP in the LVO//LVP full cells at different N/P ratios (1.90–3.50 V: N/P = 1.1, 2.05–3.50 V: N/P = 1.4, 2.25–3.50 V: N/P = 1.8).

4.2.4 Concept of charge–discharge simulation

Cycling simulations of the charge–discharge profiles of the uc-LVO//uc-LVP full cell were conducted to investigate the effect of the N/P capacity ratio on the potential shifts of the uc-LVO anode and uc-LVP cathode during cycling (see Section 4.3.1). The simulated degradation conditions of the charge–discharge curves can be broadly divided into two patterns based on the *CE*: i) $CE_{LVO} > CE_{LVP}$ or ii) $CE_{LVO} < CE_{LVP}$. As shown in Fig. 4-3, such differences in *CE* lead to differences in the capacity fade mode of full cells, especially in the potential shift of each electrode. Each of the two i) and ii) patterns can be further categorized into three patterns (six patterns in total) depending on the capacity decay of the electrode: a) no capacity fade for both anode and cathode, *i.e.*, the decrease in full cell capacity is purely due to the difference in *CE*, b) capacity fade for the cathode,

and c) capacity fade for the anode.

The charge–discharge curves used in the simulation were calculated based on the results of half-cell cycling tests of uc-LVO and uc-LVP. Considering the simulation cost, we simplified the charge curves of uc-LVO//uc-LVP by approximating them using a linear expression (the LVO and LVP formulas consisted of 9 and 11 steps, respectively).

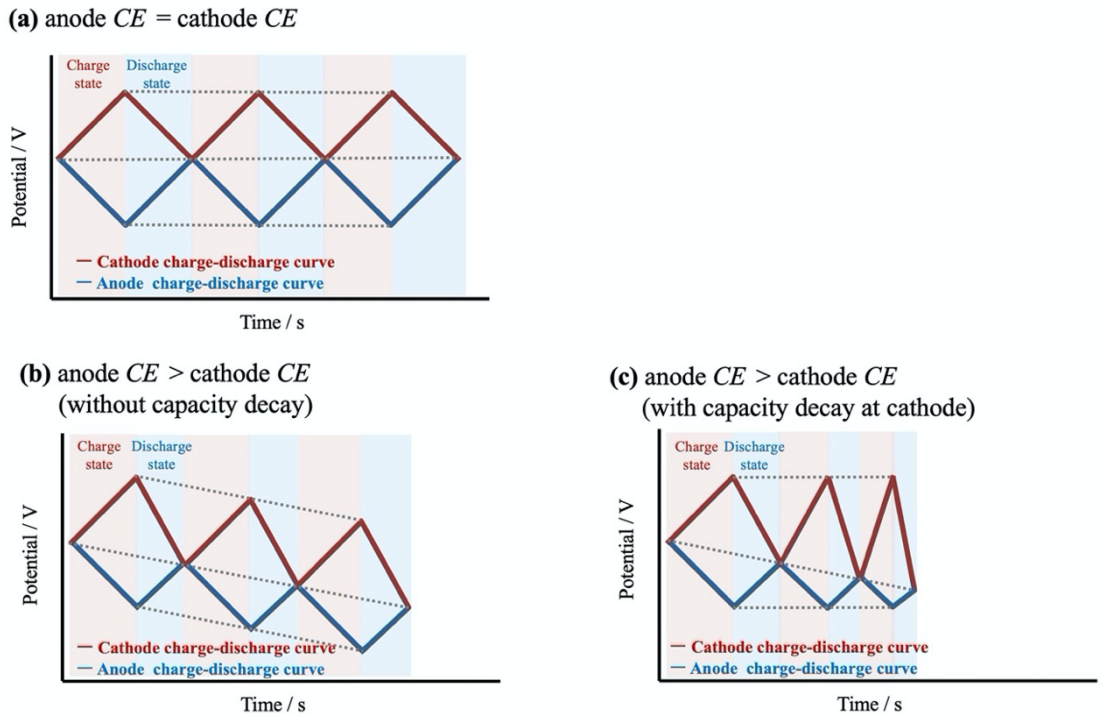

Fig. 4-3. Schematic illustrations of the degradation modes for the case that **(a)** anode *CE* = cathode *CE*, **(b)** anode *CE* > cathode *CE* without capacity decay, and **(c)** anode *CE* > cathode *CE* with capacity decay at cathode.

4.2.5 Simulation of charge–discharge behavior of Li_3VO_4//$Li_3V_2(PO_4)_3$ full-cells

Simulations of charge–discharge profiles of LVO//LVP full cell were conducted to investigate the effect of the N/P capacity ratio on the potential shifts of the LVO negative and LVP positive electrodes during cycling. Six different degradation patterns were simulated. First, the simulated degradation conditions of the charge–discharge curves were categorized into two patterns based on the discrepancy in *CE* between the LVO

negative electrode and LVP positive electrode: i) $CE_{LVO} > CE_{LVP}$ or ii) $CE_{LVO} < CE_{LVP}$. The potential curve shifts of LVO and LVP during cycling depends on their *CE* magnitude relation, *i.e.*, i) or ii). Each of the two i) and ii) patterns were further categorized into three patterns (six patterns in total) depending on whether the degradation is accompanied with the capacity decay of electrodes: a) no capacity fade for both the negative and positive electrodes, *i.e.*, the decrease in full cell capacity is purely due to the difference in *CE*, b) capacity decay for the LVP positive electrode, and c) capacity decay for the LVO negative electrode.

In advance of the cycling simulation, the potential curves of the LVO negative and LVP positive electrodes were simplified to decrease the simulation cost; the charge potential curves of the LVO negative and the LVP positive electrodes obtained for the Li metal half-cells were divided into 9 and 11 approximated lines, respectively (see Fig. 4-4). Note that, for the simplification, the discharge potential curves were assumed to be identical to the charge curves and the effects of internal resistance and potential hysteresis on the potential curves were disregarded. As the potential curves in the simulation are composed of approximated lines, the total capacity decrease can be expressed by changes in their slopes. Thus, by considering only the *CE* difference between the negative and positive electrodes without any capacity decay of the electrodes, the slope of the discharge potential profiles (S_{Dis}) can be expressed as follow:

$$S_{\mathrm{Dis}} = S_{\mathrm{Cha}} / CE \tag{4-5}$$

where S_{Cha} is the slope of the charge curve. Based on Equation (4-5), cycling simulations with Python code were conducted. The used operating potentials of the LVO negative and LVP positive electrodes for various N/P capacity ratios are listed in the inset table of Fig. 4-2. In the case that the degradation mode is accompanied with capacity decay of the

electrodes, the change in the slope of the charge ($S'_{\mathrm{Cha\_n}}$) and discharge ($S'_{\mathrm{Dis\_n}}$) potential curves at the designated cycle number of the LVO//LVP full cells (n) can be expressed as follows:

$$S'_{\mathrm{Cha\_n}} = S_{\mathrm{Cha}} / (F_{dec})^{n-1} \quad (4\text{-}6)$$

$$S'_{\mathrm{Dis\_n}} = S_{\mathrm{Dis}} / (F_{dec})^{n} \quad (4\text{-}7)$$

where F_{dec} is the capacity decay factor in which the exhibited capacity of the electrode decreases in proportion to the F_{dec} of each cycle. The operating voltages of LVO//LVP for various N/P capacity ratios were determined using the configuration described in Section 4.2.3. An example of the Python simulation code used to examine the charge–discharge cycling of the LVO//LVP full cells is provided below (N/P = 1.1 system corresponding to low *CE* with capacity decay at the LVO negative electrode).

```
# import library
import csv
import pandas as pd
import matplotlib as mpl
mpl.use('Agg')
import matplotlib.pyplot as plt

#Preparation of figures
fig = plt.figure()

# set values
maxV_p = 5.0 # max positive potential
minV_p = 2.5 # max positive potential
maxV_n = 2.5 # min negative electrode potential
minV_n = 0 # min negative electrode potential
dt = 0.0001 # time increment
n = 1 # cycle number
f = 1.1 # NP capacity ratio
x = 1 # LVP positive coulombic efficiency
y = 0.999 # LVO negative electrode coulombic efficiency
p = 1 # degradation factor of LVP positive
q = 0.9995 # degradation factor of LVO negative electrode

# starting values
V_p = 3.35 # positive potential
V_n = 1.45 # positive potential
```

```
t = 0 # time
datalist = [] # create blank list to store values
datalist2 = [] # create blank list to store values
datalist3 = [] # create blank list to store values
datalist50 = []
datalist51 = []

# capacity values
cha_cap = 0
dis_cap = 0
t1 = 0
t2 = 0

# loop over 50 cycles
while (n <= 50):
    t1 = t

  # 'charge' step
    while (maxV_p - V_p >= 0 and V_p - V_n <= 3.5 and V_n - minV_n >= 0) :
        t = t + dt
        # equations of charge curve for LVP positive with linear approximation
        a = p ** (n-1)
        c = f * q ** (n-1)
        if V_p >= 4.101300:
            V_p = V_p + (0.9530 / a * dt)
        elif V_p >= 4.07632:
            V_p = V_p + (0.0506 / a * dt)
        elif V_p >= 3.76306:
            V_p = V_p + (1.9805 / a * dt)
        elif V_p >= 3.70071:
            V_p = V_p + (0.9715 / a * dt)
        elif V_p >= 3.67612:
            V_p = V_p + (0.1133 / a * dt)
        elif V_p >= 3.60907:
            V_p = V_p + (0.8389 / a * dt)
        elif V_p >= 3.57512:
            V_p = V_p + (0.1275 / a * dt)
        elif V_p >= 3.51511:
            V_p = V_p + (2.0093 / a * dt)
        elif V_p >= 3.44298:
            V_p = V_p + (14.212 / a * dt)
        elif V_p >= 3.29282:
            V_p = V_p + (5.0024 / a * dt)
        else:
            V_p = V_p + (181.37 / a * dt)

        # equations of charge curve for LVO negative electrode with linear approximation
        if V_n >= 2.0226:
            V_n = V_n + (-30.812 / c * dt)
        elif V_n >= 1.5221:
            V_n = V_n + (-7.7328 / c * dt)
        elif V_n >= 1.2633:
            V_n = V_n + (-2.3232 / c * dt)
        elif V_n >= 1.1479:
```

```
        V_n = V_n + (-1.1635 / c * dt)
    elif V_n >= 0.8170:
        V_n = V_n + (-0.7213 / c * dt)
    elif V_n >= 0.6007:
        V_n = V_n + (-0.7634 / c * dt)
    elif V_n >= 0.4755:
        V_n = V_n + (-0.7294 / c * dt)
    elif V_n >= 0.1977:
        V_n = V_n + (-1.3326 / c * dt)
    else:
        V_n = V_n + (-0.7296 / c * dt)

    DV = V_p - V_n # cell voltage
    state = "C" # identification of charge step

    # data output conditions
    if n == 1:
        count_t = t - t1
        data = [count_t, n, state, DV, V_p, V_n]
        datalist.append(data)
        data3 = [count_t, DV, V_p, V_n]
        datalist3.append(data3)

    if n == 50:
        count_t = t - t1
        data = [count_t, n, state, DV, V_p, V_n]
        datalist50.append(data)
        data3 = [count_t, DV, V_p, V_n]
        datalist51.append(data3)

t2 = t

    # 'discharge' step
    while (maxV_n - V_n >= 0 and V_p - V_n >= 1.9 and V_p - minV_p >= 0):
    t = t + dt
    # equations of discharge curve for LVP positive with linear approximation
    b = x * p ** n
    d = f * y * q ** (n-1)
    if V_p >= 4.101300:
        V_p = V_p + (-0.9530 / b * dt)
    elif    V_p >= 4.07632:
        V_p = V_p + (-0.0506 / b * dt)
    elif V_p >= 3.76306:
        V_p = V_p + (-1.9805 / b * dt)
    elif V_p >= 3.70071:
        V_p = V_p + (-0.9715 / b * dt)
    elif V_p >= 3.67612:
        V_p = V_p + (-0.1133 / b * dt)
    elif V_p >= 3.60907:
        V_p = V_p + (-0.8389 / b * dt)
    elif V_p >= 3.57512:
        V_p = V_p + (-0.1275 / b * dt)
    elif V_p >= 3.51511:
        V_p = V_p + (-2.0093 / b * dt)
```

```
        elif V_p >= 3.44298:
            V_p = V_p + (-14.212 / b * dt)
        elif V_p >= 3.29282:
            V_p = V_p + (-5.0024 / b * dt)
        else:
            V_p = V_p + (-181.37 / b * dt)

        # equations of discharge curve for LVO negative electrode with linear approximation
        if V_n >= 2.0226:
            V_n = V_n + (30.812 / d * dt)
        elif V_n >= 1.52207:
            V_n = V_n + (7.7328 / d * dt)
        elif V_n >= 1.2633:
            V_n = V_n + (2.3232 / d * dt)
        elif V_n >= 1.1479:
            V_n = V_n + (1.1635 / d * dt)
        elif V_n >= 0.8170:
            V_n = V_n + (0.7213 / d * dt)
        elif V_n >= 0.6007:
            V_n = V_n + (0.7634 / d * dt)
        elif V_n >= 0.4755:
            V_n = V_n + (0.7294 / d * dt)
        elif V_n >= 0.1977:
            V_n = V_n + (1.3326 / d * dt)
        else:
            V_n = V_n + (0.7296 / d * dt)

        DV = V_p - V_n # cell voltage
        state = "D" # identification of discharge step

        # data output conditions
        if n == 1:
            count_t = t - t1
            data = [count_t, n, state, DV, V_p, V_n]
            datalist.append(data)
            data3 = [count_t, DV, V_p, V_n]
            datalist3.append(data3)

        if n == 50:
            count_t = t - t1
            data = [count_t, n, state, DV, V_p, V_n]
            datalist50.append(data)
            data3 = [count_t, DV, V_p, V_n]
            datalist51.append(data3)

    t3 = t
    cha_cap = t2 - t1
    dis_cap = t3 - t2
    data2 = [n,cha_cap,dis_cap]
    datalist2.append(data2)

    n += 1

dl = pd.DataFrame(datalist,columns=['count_t','n','state','DV','V_p','V_n'])
```

```
dw = pd.DataFrame(datalist2,columns=['n','cha_cap','dis_cap'])
df = pd.DataFrame(datalist3,columns=['count_t','DV','V_p','V_n'])
dc = pd.DataFrame(datalist50,columns=['count_t','n','state','DV','V_p','V_n'])
dd = pd.DataFrame(datalist51,columns=['count_t','DV','V_p','V_n'])
dd = dd.drop(columns='count_t')
de = pd.concat([df,dd],axis=1)
```

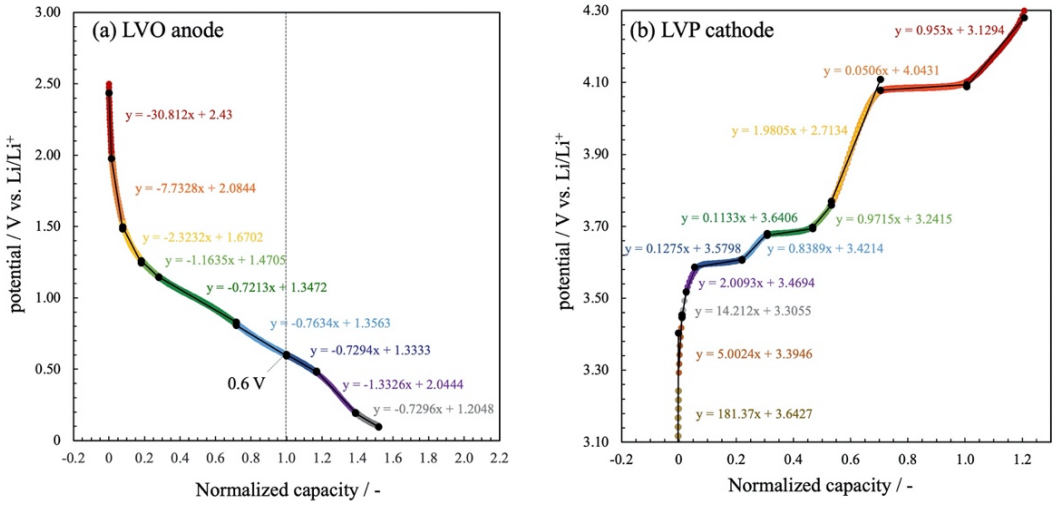

Fig. 4-4. Approximated equations for the charge–discharge curves of the **(a)** LVP positive and **(b)** LVO negative electrodes.

4.2.6 Surface analysis of Li_3VO_4//$Li_3V_2(PO_4)_3$ full cells using XPS and SEM

The surface morphology of the LVO and LVP electrodes were examined before and after cycling in the LVO//LVP full cell *via* scanning electron microscopy (SEM; Hitachi model S5500) and XPS (JEOL Ltd., JPS-9200). Prior to the SEM and XPS measurements, the cycled electrodes were rinsed with dimethyl carbonate and dried under vacuum overnight. All the samples were prepared in a glove box to minimize any possible contamination and XPS was performed using Al Kα (hν = 1486.6 eV) radiation under ultra-high vacuum. The XPS spectra were collected at a voltage of 12 kV and emission current of 10 mA. All the XPS spectra were energy calibrated to the hydrocarbon peak with a binding energy of 284.8 eV.

4.3 Results and Discussion

4.3.1 X-ray diffraction and thermogravimetric analysis of the uc-treated Li_3VO_4/MWCNTs and $Li_3V_2(PO_4)_3$/MWCNTs nanocomposites

The uc-LVO and uc-LVP were synthesized through uc treatment,[8, 12] as anode and cathode materials, respectively. The details of the synthesis processes are described in our previous reports.[8, 12] The successful synthesis of the uc-LVO and uc-LVP were confirmed with X-ray diffraction (XRD) and thermogravimetric (TG) data. As indicated in the obtained XRD patterns (Figs. 4-5 (a) and (b)), all the Bragg peaks of uc-LVO and uc-LVP were indexed to the crystalline structure of orthorhombic LVO and monoclinic LVP, respectively. The broad peak (2θ = 20 to 30º) was assigned to MWCNTs. The TG curves under synthetic air (Figs. 4-5 (c) and (d)) were used to calculate the weight ratio of LVO:MWCNTs and LVP:MWCNTs, which were determined to be 60:40 and 70:30, respectively.

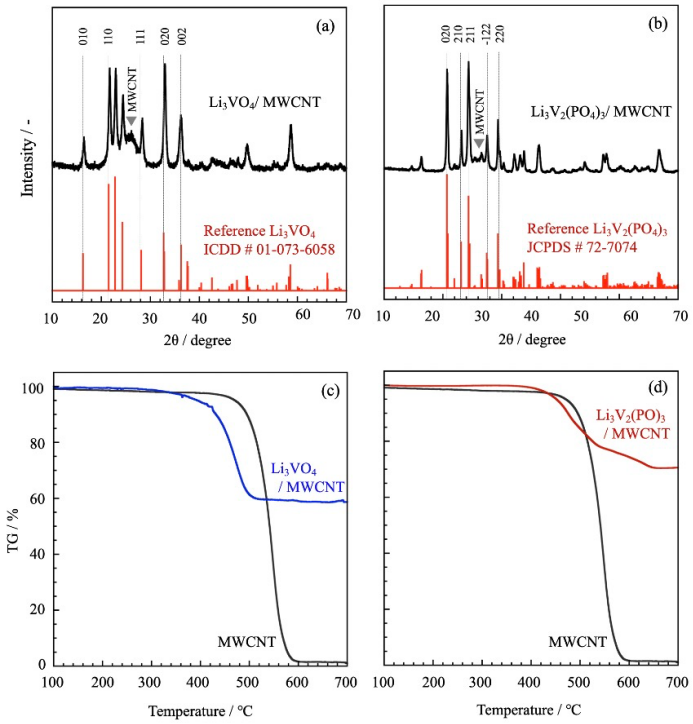

Fig. 4-5. XRD patterns of uc-treated **(a)** Li_3VO_4/MWCNTs and **(b)** $Li_3V_2(PO_4)_3$/MWCNTs. TG curves of **(c)** Li_3VO_4/MWCNTs and MWCNTs and **(d)** $Li_3V_2(PO_4)_3$/MWCNTs and MWCNTs.

4.3.2 Cyclability of Li_3VO_4//$Li_3V_2(PO_4)_3$ full cells with various N/P capacity ratios

Prior to the charge–discharge cycle tests of the LVO//LVP full cells, the cyclability of the LVP positive and LVO negative electrodes were measured at 25 °C for 1000 cycles using the half-cells (coin-type cells). Fig. 4-6 presents the results of the half-cell cycle tests, demonstrating that the capacity retention of the LVP positive and LVO negative electrodes after 4000 cycles was 90% and 93%, respectively. These results suggest that the cyclability of the LVO//LVP full cells was high because of the high cyclability of the positive and negative electrodes in the half-cells.

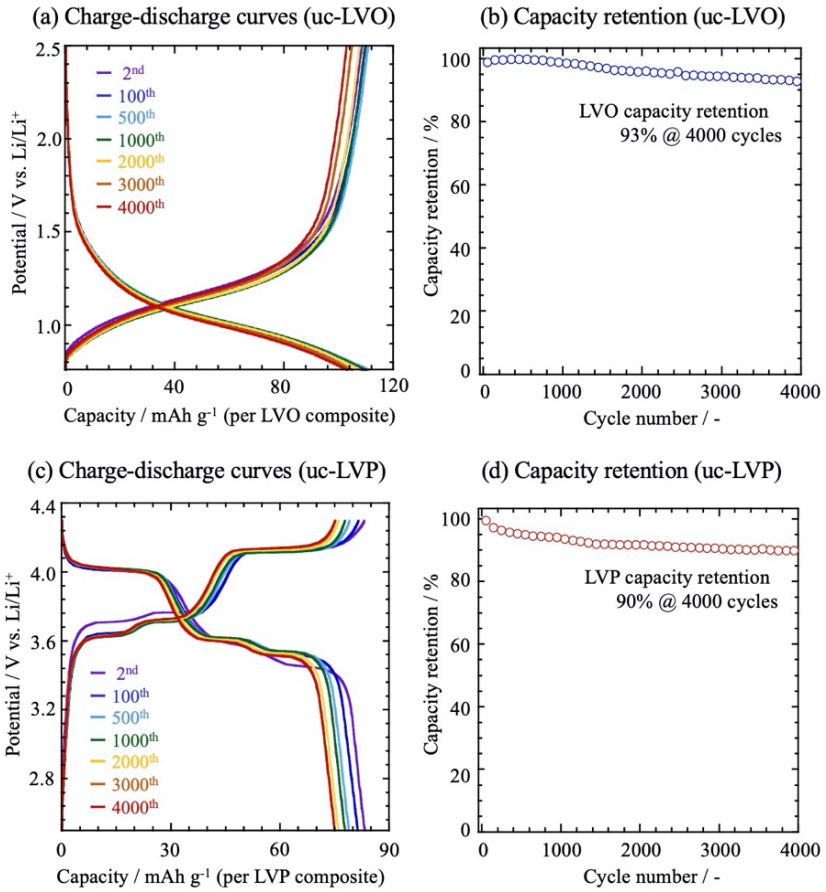

Fig. 4-6. Capacity plots over 4000 cycles using half-cells at 25 °C. **(a)** charge–discharge curves and **(b)** capacity retention for the LVO negative electrode at 1 A g^{-1} (per LVO composite, *ca*. 10C-rate). **(c)** charge–discharge curves and **(d)** capacity retention for the LVP positive at 0.9 A g^{-1} (per LVP composite, *ca*. 10C-rate).

4.3.3 Rate capability of Li_3VO_4//$Li_3V_2(PO_4)_3$ full cells

Nanocomposites of Li_3VO_4 (LVO) and $Li_3V_2(PO_4)_3$ (LVP) were separately synthesized with multiwalled carbon nanotubes (MWCNTs) *via* our unique ultracentrifugation (uc) treatment.[8, 12] Using the synthesized uc-LVO and uc-LVP, the uc-LVO//uc-LVP full cells were assembled and their power capability was tested. Charge–discharge curves for the uc-LVO//uc-LVP full cells in which the N/P capacity ratio equals 1.1 are presented in Fig. 4-7. In both the discharge-rate (Fig. 4-7 (a)) and charge-rate (Fig. 4-7 (b)) capability tests, the full cells exhibited excellent rate capabilities; specifically, 80% of the capacity at 1C-rate (1C-rate = 74 mAh g^{-1} (per uc-LVP composite)) was maintained even at a high rate of 100C-rate. The full cells at higher N/P capacity ratios (N/P = 1.4 and 1.8) showed similarly high rate capabilities for both discharging and charging at rates up to 100C-rate, as shown in Figs. 4-7 (c) and (d).

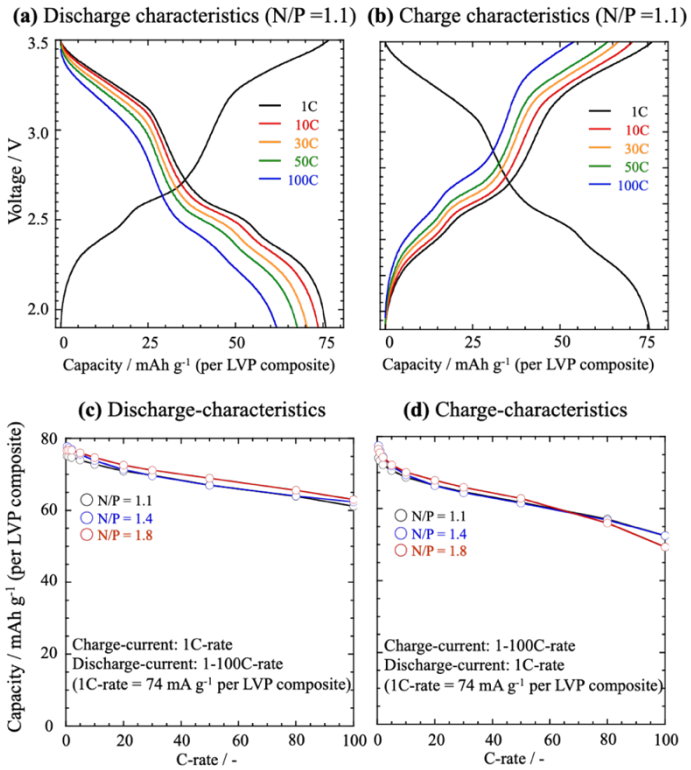

Fig. 4-7. (a–b) Charge–discharge curves of the uc-LVO//uc-LVP full cells (N/P = 1.1) at 25 °C: **(a)** different discharge C-rates from 1 to 100C-rate and a fixed charge C-rate of

1C-rate and **(b)** different charge C-rates from 1 to 100C-rate and a fixed discharge C-rate of 1C-rate. (1C-rate = 74 mAh g^{-1} per uc-LVP composite) **(c–d)** Capacity retention of the discharge/charge characteristics at different C-rates in the uc-LVO//uc-LVP full cells at three N/P ratios (1.1, 1.4, and 1.8).

The charge–discharge curves up to the 1000th cycle for the uc-LVO//uc-LVP full cells with three different N/P ratios (1.1, 1.4, and 1.8) are shown in Figs. 4-8 (a)–(c). Note that all the cyclability tests shown in Fig. 4-8 were conducted at 50 °C to accelerate the capacity degradation of the uc-LVO//uc-LVP cells. The capacity retention at room temperature (25 °C) did not show any degradation and differences at the three N/P capacity ratios over 1000 cycles (Fig. 4-9).

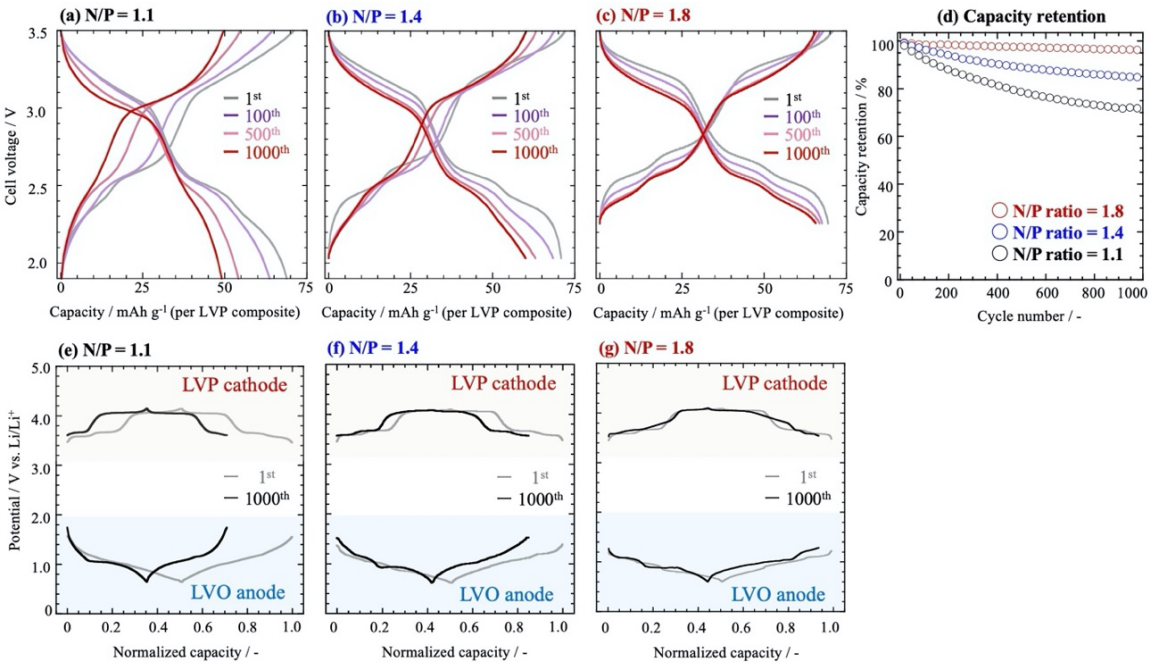

Fig. 4-8. (a–c) Charge–discharge curves of the LVO//LVP full cells at 50 °C for the 1st, 100th, 500th, and 1000th cycle at 0.74 A g^{-1} (per LVP composite, *ca*. 10C-rate). **(d)** Capacity retention plots of the LVO//LVP full cells. **(e–g)** Charge–discharge potential curves of the individual LVP and LVO electrode at the 1st and 1000th cycle. The corresponding N/P capacity ratios are 1.1 for **(a, e)**, 1.4 for **(b, f)**, and 1.8 for **(c, g)**.

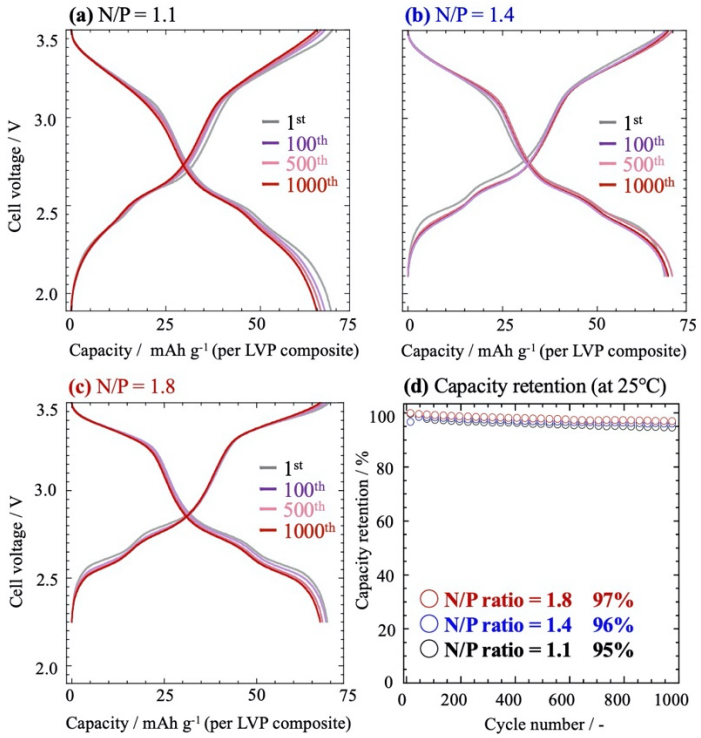

Fig. 4-9. Charge–discharge behavior and capacity retention of the uc-LVO//uc-LVP full cells at N/P = 1.1, 1.4, and 1.8 at 25 °C; **(a–c)** Charge–discharge curves for the 1st, 100th, 500th, and 1000th cycle at 0.74 mA g^{-1} (per uc-LVP composite, ca. 10C-rate) and **(d)** capacity retention over 1000 cycles.

As shown in Fig. 4-8, at the 1st cycle, all the LVO//LVP cells exhibited a similar overall shape for the charge–discharge curves with a capacity of ~ 70 mAh g^{-1} (per LVP composite). This shape reflects the combined characteristics of the charge–discharge profiles of the two electrodes, *i.e.*, the slope of LVO (Fig. 4-4 (a)) and the inflection points at approximately 3.60, 3.65, and 4.05 V *vs.* Li/Li^+ due to the three-step plateau of LVP (Fig. 4-4 (b)). However, with an increase in cycle numbers, the difference among the three cells became obvious. The charge–discharge curves for the LVO//LVP cell with N/P = 1.1 became distorted and the cut-off voltage of the full cell (1.9–3.5 V) occurred earlier than at the 1st cycle, resulting in a low capacity retention of 72% (decreased from 68 to 49

mAh g^{-1}). By increasing the N/P capacity ratio (1.4 and 1.8), the shape of the charge–discharge curves after the 1000th cycle became less distorted, resulting in a better capacity retention compared with that of N/P =1.1. The capacity retention of the full cells increased with an increase in the N/P capacity ratio (72% at N/P = 1.1, 85% at N/P = 1.4, and 96% at N/P = 1.8), as shown in Fig. 4-8 (d). Considering the excellent cyclability of LVO and LVP (Fig. 4-6), the degradation of the active materials may be responsible for the capacity degradation of the LVO//LVP full cells.

The potential curves versus the lithium reference electrode of the LVO negative and LVP positive electrodes during LVO//LVP full cell cycling are shown in Figs. 4-8 (e)–(g). In the LVP charge–discharge profile at N/P = 1.1 (Fig. 4-8 (e), upper portion), the first plateau region (0.5 Li^+) at *ca*. 3.60 V *vs.* Li/Li^+ disappeared and the length of the second plateau region (1.0 Li^+) at *ca*. 3.65 V *vs.* Li/Li^+ shortened to 65% of the 1st cycle after 1000 cycles. Consequently, the termination potential of the LVP discharge curve (LVP *MinV*) increased from 3.46 to 3.61 V *vs.* Li/Li^+ (by 0.15 V) after 1000 cycles, whereas LVP *MaxV* remained almost the same (changed from 4.14 to 4.15 V). The LVO *Max*V and *Min*V values corresponded to those of the LVP positive electrode; namely, LVO *MaxV* changed from 1.51 V to 1.66 V, while LVO *MinV* remained almost the same. By increasing to N/P capacity ratio to over 1.4 (Figs. 4-8 (f) and (g)), the second plateau of the LVP positive electrode was retained after 1000 cycles and the length of the remaining first plateau became longer (60% and 85% at N/P = 1.4 and 1.8, respectively). Consequently, the shift in LVP *MinV* and LVO *MaxV* after 1000 cycles became smaller: 0.10 V and 0.06 V at N/P = 1.4 and 1.8, respectively. To provide a reasonable explanation for such potential shift changes with different N/P capacity ratios during cycling, the degradation behavior of the negative and positive electrodes was analyzed by simulating

the charge–discharge curves of the LVO//LVP full cells.

4.3.4 Elucidation of degradation mechanism in the Li_3VO_4//$Li_3V_2(PO_4)_3$ full cells

Simulations of the charge–discharge profiles of the LVO//LVP full cell were conducted to investigate the effect of the N/P capacity ratio on the potential shifts of the LVO negative and LVP positive electrodes during cycling (Section 4.3.1). Fig. 4-10 presents the experimental results (potential curves) of the LVO negative and LVP positive electrodes during full cell cycling at N/P =1.1 (Fig. 4-10 (a), reproduced from Fig. 4-8 (e)) and the results of six simulated degradation patterns (Figs. 4-10 (b)–(g)). To reduce calculation cost, the simulation cycle numbers were limited to 50 by adjusting the values of *CE* and F_{dec}. The arrows in each figure indicate the direction of the potential shift after cycling, *e.g.*, for the experimental data at N/P = 1.1 (Fig. 4-10 (a)), LVO *MinV* and LVP *MaxV* remained constant (green arrows), while LVO *MaxV* and *LVP MinV* shifted to higher potentials (red arrows). By focusing on these arrow directions, one can easily identify the factors responsible for capacity degradation during LVO//LVP full cell cycling. Among the six simulated conditions, only one condition, $CE_{LVO} < CE_{LVP}$ with capacity decay of LVO (Fig. 4-10 (g)), showed the same arrow directions observed in the experimental result (Fig. 4-10 (a)). The obtained results indicated that the decrease in LVO *CE* with capacity decay was responsible for the observed LVO//LVP full cell degradation.

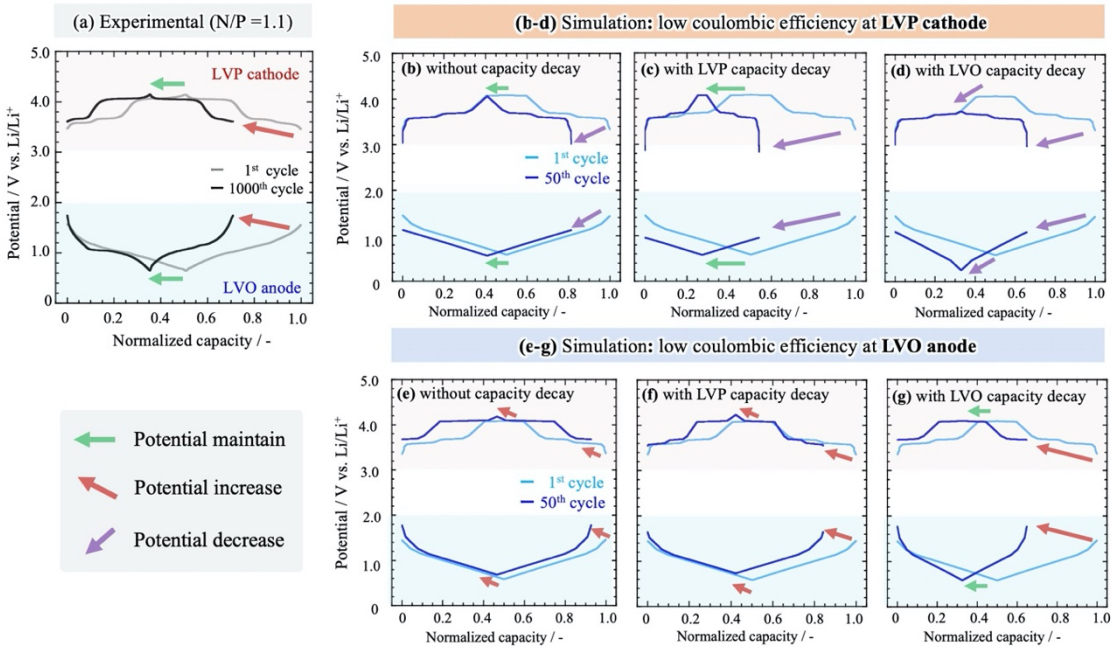

Fig. 4-10. (a) Observed LVP and LVO potential at N/P = 1.1 (Fig. 4-8 (e)). **(b–e)** Simulations of the charge–discharge behavior of LVO and LVP over 1000 cycles at N/P =1.1 and low coulombic efficiency (C_{eff}): Without capacity decay at **(b)** LVO C_{eff} = 100% and LVP C_{eff} = 99.9% and **(c)** LVO C_{eff} = 99.9% and LVP C_{eff} = 100%. With capacity decay corresponding to capacity decay factor (F_{dec}) (see Section 4.2.4) at **(d)** LVO F_{dec} = 100% and LVP F_{dec} = 99.95% and **(e)** LVO F_{dec} = 99.95% and LVP F_{dec} = 100%.

To validate the reliability of the simulated results, the simulated charge–discharge curves were compared with the experimental results, as mentioned in Figs. 4-11 (a)–(c) (initial cycle). As shown in the figure, the simulation results at the 1st cycle agreed with the experimental results at all N/P capacity ratios. The charge–discharge curves after cycling (observed results: after 1000 cycles; simulation: after 50 cycles) were generally consistent, as shown in Figs. 4-11 (d)–(f).

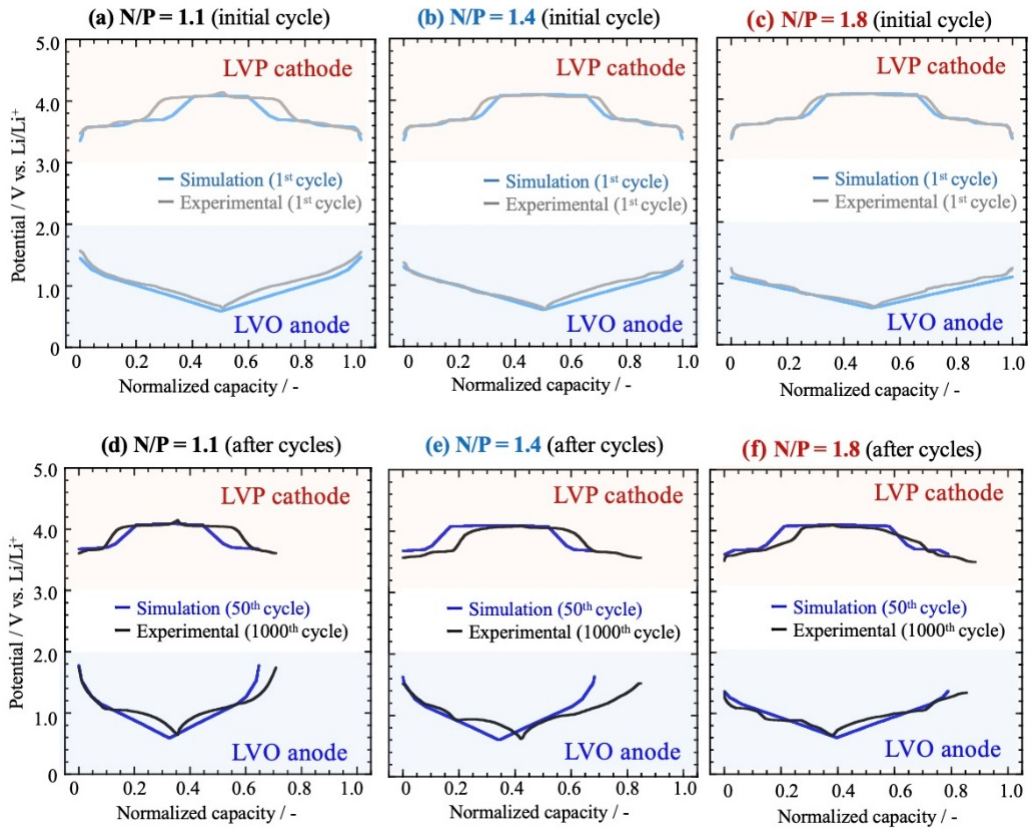

Fig. 4-11. Comparison of simulated and experimental charge–discharge curves: Initial cycle (1st cycle) at N/P capacity ratios of **(a)** 1.1, **(b)** 1.4, and **(c)** 1.8. After cycling (observed: 1000th cycle; simulated: 50th cycle) at N/P capacity ratios of **(d)** 1.1, **(e)** 1.4, and **(f)** 1.8 at LVO *CE* = 99.9 %, LVP *CE* = 100 %, LVO F_{dec} = 99.95 %, and LVP F_{dec} = 100 %.

As described in the Fig. 4-10, the results of the charge–discharge simulations in uc-LVO//uc-LVP full cell cycling indicate that the capacity degradation of the uc-LVO//uc-LVP full cells full may be due to an increase in the *CE* misfit between the anode and cathode ($CE_{LVO} < CE_{LVP}$) accompanied with a capacity decay of the uc-LVO anode. To support these simulated results, we conducted charge–discharge tests using the anode and cathode, which were cycled in full cell configurations. First, the uc-LVO//uc-LVP full cells were disassembled after cycling over 1000 cycles at 50 °C. The cycled uc-LVO

anode and uc-LVP cathode were punched out in the dry room (dew-point temperature < −40 °C), and then Li//uc-LVO and Li//uc-LVP half-cells were reassembled using new electrolytes. As shown in Fig. 4-12 (a), the reassembled Li//uc-LVO half-cells exhibited only 76% of the capacity before full cycling, while no degradation was observed for the Li//uc-LVP half-cells (Fig. 4-12(b)). By decreasing the current density from 300 mA g^{-1} (per uc-LVO composite, ca. 3C-rate) to 30 mA g^{-1} (per uc-LVO composite, *ca.* 0.3C-rate), the capacity in reassembled Li//uc-LVO half-cells recovered to 91%. These results support the simulation results presented in the Fig. 4-10 and indicate that the capacity decay of uc-LVO after full cell cycling may be mainly due to the increased resistance of LVO reactions. In fact, the SEM images of the cycled LVO negative electrode in the LVO//LVP full cell configuration revealed that the degraded LVO negative electrode was covered with a polymeric film (Figs. 4-13 (a) and (b)), while the LVP surface was not significantly different before and after full cell cycling. This polymeric film formation, arising from electrolyte solvent decomposition, may be responsible for the increased resistance to LVO reactions. Electrolyte decomposition at the LVO surface may be caused by the catalytic vanadium species deposited on the LVO negative electrode, which originally diffused from the LVP positive electrode after dissolution as previously reported for the LTO//LVP full cell.[19] The negligible capacity decay of the re-assembled Li//LVP half-cells (Fig. 4-12) suggested that only a small amount of vanadium species was eluted. In fact, in a previous study on the LTO//LVP full cell,[19] the percentage of eluted vanadium species over the entire LVP was approximately 0.2 wt.% (0.8 μg over 4.5 mg evaluated by ICP measurements) after 1000 cycles, where similar results (no detectable capacity degradation) were obtained for the re-assembled Li//LVP full cells.

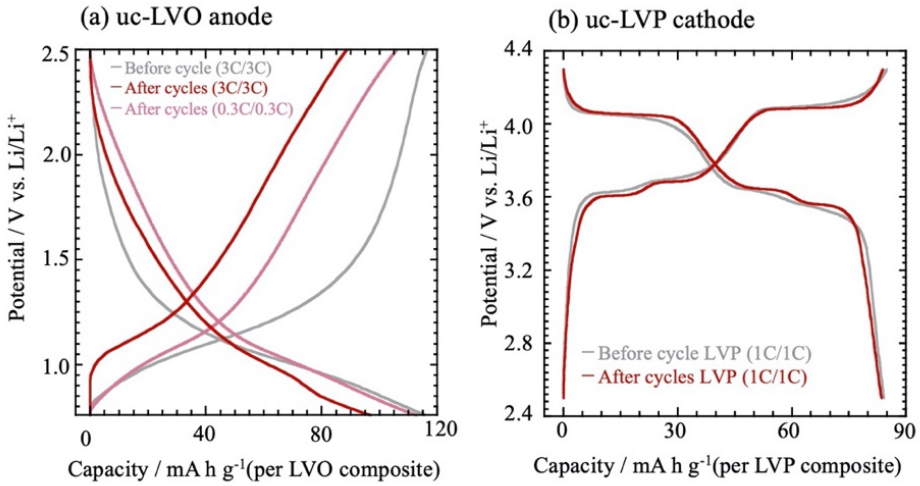

Fig. 4-12. Charge–discharge curves of the Li metal half-cells reassembled by using the electrodes removed from the LVO//LVP full cells before and after 1000 cycles: **(a)** LVO negative electrode at 300 mA g^{-1} (per LVO composite, *ca*. 3C-rate) and 30 mA g^{-1} (per LVO composite, *ca*. 0.3C-rate) cycles and **(b)** LVP positive at 90 mA g^{-1} (per LVP composite, *ca*. 1C-rate) cycles.

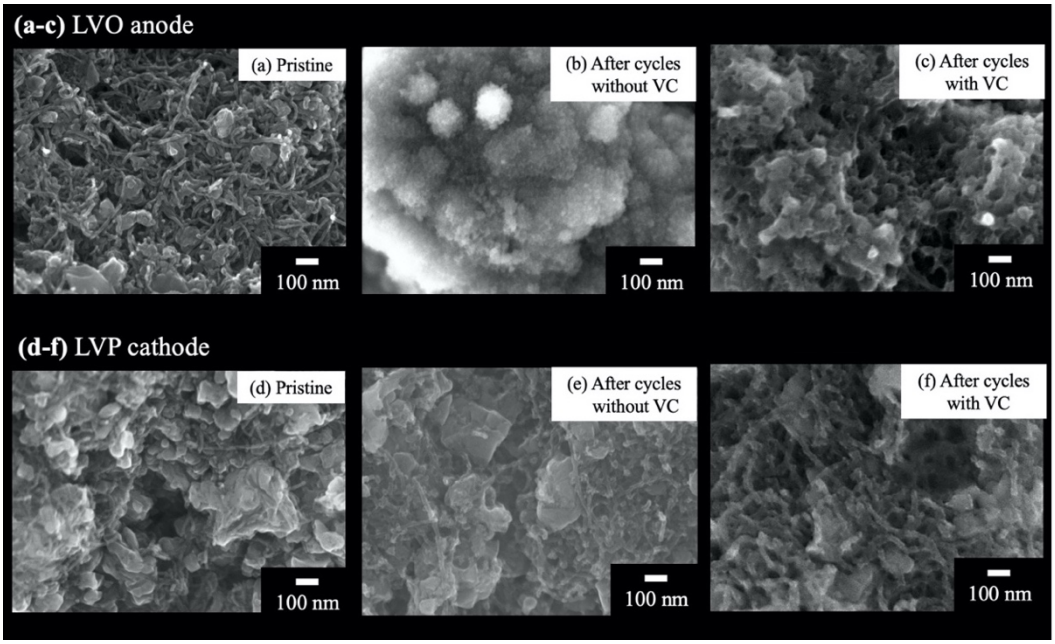

Fig. 4-13. **(a–c)** SEM images of the LVO negative electrode: **(a)** Pristine and **(b–c)** after cycling (1000th cycle, 50 °C) **(b)** without VC and **(c)** with VC in the LVO//LVP full cells. SEM images of the LVP positive electrode: **(d)** Pristine and **(e–f)** after cycling (1000th cycle, 50 °C) **(e)** without VC and **(f)** with VC in the LVO//LVP full cells.

By considering the cycling simulation results and the events occurring at the LVO electrode, the degradation mechanism of the LVO//LVP full cell is proposed to proceed as follows (Fig. 4-14): (I) During the charge process, aside from the lithiation of LVO, electrolyte reductive decomposition on the LVO negative electrode surface leads to the formation of resistive polymeric surface films. (II) Consequently, the slope of the potential profiles in the LVO discharge curve becomes steeper due to its resistance increase. (III) The steeper LVO discharge curve reaches the discharge cut-off voltage at a higher potential than the one at the previous cycle, resulting in an increase in LVO *MaxV* and LVP *MinV*. Then, as soon as LVP *MinV* reaches the potential of the first plateau of LVP, the discharge capacity of the LVO//LVP full cell immediately decreases due to the state-of-charge shift of LVP. (IV) During the re-charge, the lost capacity during the discharge never recovers as the LVO *MinV* and LVP *MaxV* values remain almost unchanged compared with those of the previous charge process. The repetition of (II), (III), and (IV) continuously shifts LVO *MaxV* and LVP *MinV* towards higher values, and the first and second plateaus of LVP become shorter, leading to a pronounced capacity loss. As the N/P capacity ratio increases, the influence of the increased resistance to LVO negative electrode reactions is mitigated because the slope of the LVO potential curves becomes gentle, which suppresses the increase in LVO *MaxV* and LVP *MinV* and thus capacity decay.

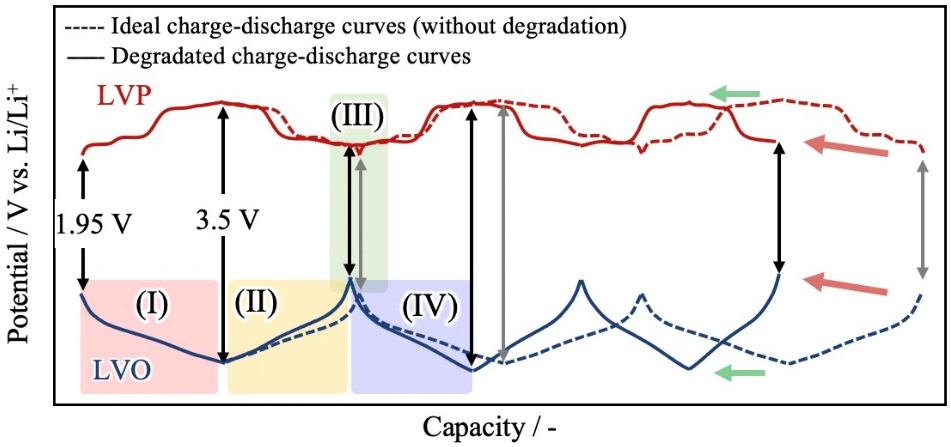

Fig. 4-14. Schematic of the capacity degradation model in LVO//LVP full cells.

4.3.5 Suppression of side reactions at the surface of the Li_3VO_4 negative electrode

As discussed in Sections 4.3.1 and 4.3.2, a high N/P system in the LVO//LVP full cells reduces the impact of the increased resistance to LVO reactions on the potential shifts of LVO *MaxV* and LVP *MinV* and thus improves the capacity retention of the LVO//LVP full cells. However, a high N/P (1.4 and 1.8) system unavoidably sacrifices its specific capacity and thus energy density. Accordingly, an ideal full cell can be achieved with an N/P capacity ratio that is as close as possible to 1. As the N/P capacity ratio increases, the excess LVO capacity increases; specifically, the calculated energy density per gram of composite (LVP positive + LVO negative electrodes) was 135, 125, and 120 Wh kg^{-1} at N/P capacity ratios of 1.1, 1.4, and 1.8, respectively. To design a full cell with a low N/P capacity ratio, it is important that electrolyte decomposition and resistive polymeric formation are suppressed at the LVO negative electrode. Here, an improvement in the cyclability of LVO//LVP full cells at a low N/P capacity ratio (= 1.1), *i.e.*, the suppression of electrolyte decomposition at the LVO negative electrode was achieved by adding VC to the electrolyte. VC, which forms a protective layer, was chosen as the additive because it has been widely applied for other negative electrode materials, such

as graphite and Si.[24-26] As shown in the differential capacity (dQ/dV) plots of the Li//uc-LVO half-cell at the 1st cycle (Fig. 4-15) of pre-conditioning (Supporting Information: "Pre-conditioning procedure of the uc-LVO anode and uc-LVP cathode"), the peak potential attributed to reductive decomposition appeared at a higher potential with VC (0.74 V *vs.* Li/Li^+) than without VC (0.70 V *vs.* Li/Li^+). This difference indicates that electrolyte reductive decomposition on the uc-LVO anode surface may be different in the presence of VC.

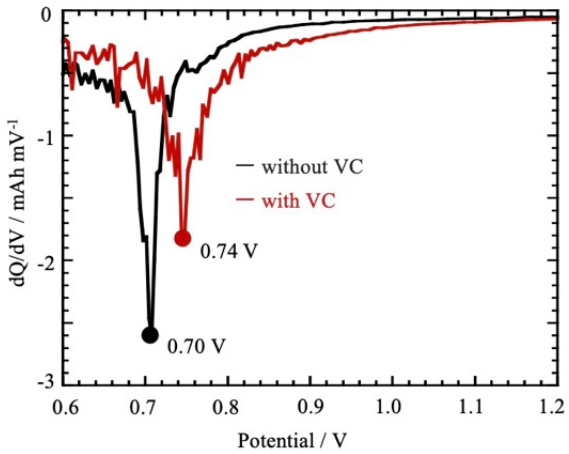

Fig. 4-15. dQ/dV plots of the first charge processes at the LVO negative electrode at 300 mA g^{-1} using the Li//LVO half-cell with or without VC additives (+5 wt.%).

XPS analysis was conducted for the pristine and pre-conditioned (Supporting Information: "Pre-conditioning procedure of the LVO anode and LVP cathode") electrodes, as shown in Figs. 4-16 (a)–(c) (uc-LVO anode) and Figs. 4-16 (d)–(f) (uc-LVP cathode), to examine the electrode surface with and without the VC additive. In the XPS spectra, the C1s and O1s, CO_3, C-O, and C=O peaks were observed for the uc-LVO anode without VC (Figs. 4-16 (a) and (b)), which were derived from Li_2CO_3 and $ROCO_2Li$. In the presence of VC, the C-O and C=O peaks were enhanced in the C1s and O1s regions,

suggesting that the uc-LVO anode was coated with the VC-derived polymeric film.[25] The disappearance of the V2p peak after cycling (Fig. 4-16(c)) further indicated that the surface of the uc-LVO anode was covered by decomposed electrolyte materials (such as Li_2CO_3 and $ROCO_2Li$) or the VC-derived polymeric film. In the case of the uc-LVP cathode (Figs. 4-16 (d)–(f)), there was no significant difference in C1s, O1s, and V2p before and after cycling with or without VC. The above results suggest that, unlike the uc-LVO anode, the uc-LVP electrode surface was not coated in the presence of VC.

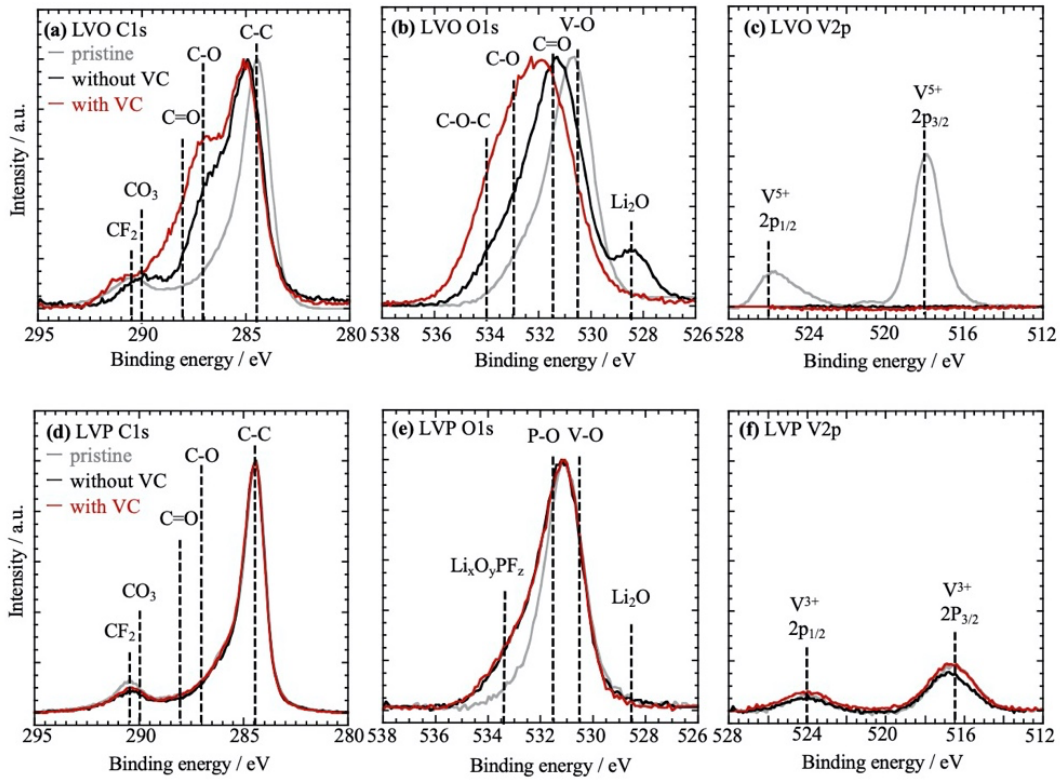

Fig. 4-16. XPS spectra of **(a–c)** the LVO negative electrode: **(a)** C1s, **(b)** O1s, and **(c)** V2p and **(d–f)** the LVP positive electrode: **(d)** C1s, **(e)** O1s, and **(f)** V2p. Pristine (before cycle, gray line) and after 20 cycles with or without VC (red and black lines, respectively) in LVO//LVP full cells.

Fig. 4-17 depicts the cycle performance of the LVO//LVP full cells using the VC-added electrolyte at a low N/P capacity ratio (N/P = 1.1) up to 1000 cycles at 50 °C. As

shown in Fig. 4-17 (a), the charge–discharge curves of these cells showed a slight decrease in capacity (86% of the initial cycle capacity), and the overall curves were maintained. By contrast, the curves were deformed in the absence of VC (Fig. 4-9 (a)). The potential curves of LVP and LVO in the full cells tested with VC (Fig. 4-17 (b)) indicated that the shift in LVP *MinV* and LVO *MaxV* after 1000 cycles were mitigated (0.08 V) in relation to the cells without VC (0.15 V). Accordingly, the second plateau region (1.0 Li^+ reaction) of LVP was maintained even after 1000 cycles, similar to the case of a high N/P capacity ratio without the VC additive. To determine the change in cell resistance of the uc-LVO//uc-LVP full cells with and without VC additives (5 wt.%), direct current internal resistances (DCIRs) were evaluated after the 3^{rd} and 1000^{th} cycle. The evaluated DCIR values are shown in the bar chart of Fig. 4-18. At the 3^{rd} cycle, the DCIR with VC (9.9 mΩ) was larger than that without VC (8.8 mΩ), which was attributed to the passivation film formed from decomposed VC on the LVO surface. After 1000 cycles, however, the DCIR with VC (14.7 mΩ) became smaller than that without VC (17.4 mΩ), indicating that electrolyte decomposition during long term cycling was suppressed owing to the existence of the VC-derived passivation film. The SEM images of the LVO anode surface (see Fig. 4-13) support the DCIR change with or without VC. These results suggest that the VC-derived passivation film formed on the LVO negative electrode during pre-conditioning may effectively suppress electrolyte decomposition (Figs. 4-13 (c) and (f)) and thus improve the *CE* of the LVO negative electrode, mitigating the potential shifts of LVP *MinV* and LVO *MaxV*. As shown in Fig. 4-17 (c), the capacity retention at N/P = 1.1 improved from 72% to 86% upon employing VC; the improved figure is comparable with those obtained for higher N/P capacity ratios (> 1.4). These results demonstrate that the developed simple cycling simulation can assist with the

elucidation of the degradation mode of full cell cycling with less experimental effort and provide insights for the development of strategies that mitigate capacity degradation.

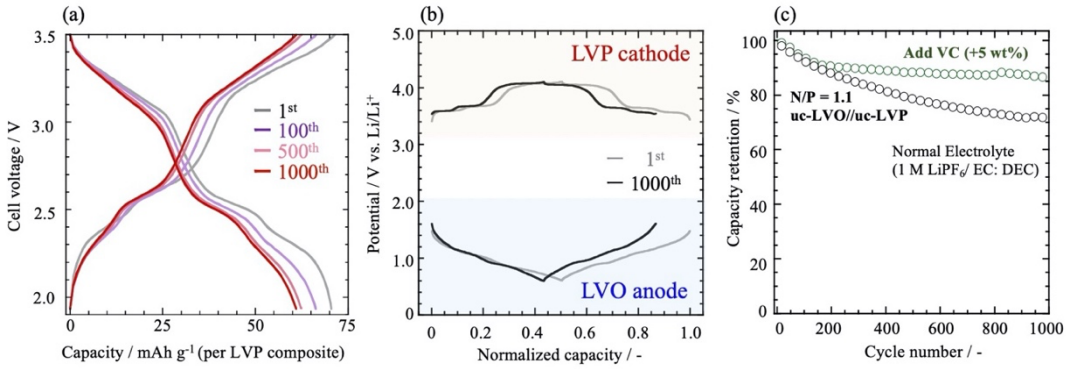

Fig. 4-17. Results of the LVO//LVP full cell cycle test at N/P = 1.1 with the addition of 5 wt.% VC. **(a)** Charge–discharge curves cycled at 50 °C for the 1st, 100th, 500th, and 1000th cycle at 0.74 A g^{-1} (per LVP composite, *ca*. 10C-rate). **(b)** Charge–discharge potential curves of LVP and LVO for the 1st and 1000th cycle. **(c)** Capacity retention plots with or without VC additive.

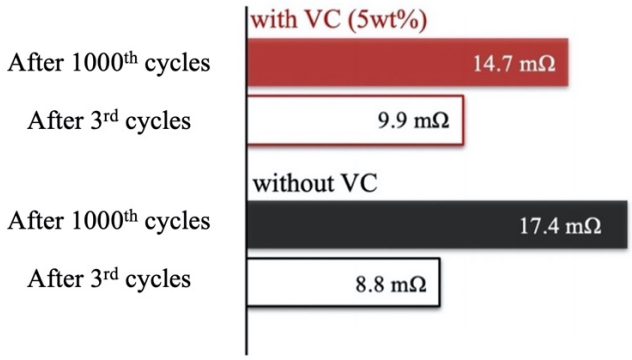

Fig. 4-18. Comparison of evaluated direct current internal resistance (DCIR) for the LVO//LVP full cells (N/P = 1.1) with or without VC additive (5 wt.%) after the 3rd and 1000th cycle. The DCIR values were calculated from the slope of the voltage plots over 10 seconds. 10-second voltage drops were measured at a cell voltage of 3.4 V, 25 °C, and different C-rates (1, 2, 3, and 5 C-rates).

4.4 Conclusion

In conclusion, to elucidate the capacity degradation mechanism of full cells, a simple cycling simulation method was applied and verified as an "indirect" method to predict the degradation factors without the need to dis-assemble the cells. First, the cyclability of the LVO//LVP full cells were evaluated at 50 °C under varying N/P capacity ratios, and the accelerated degradation of the cell capacity at N/P = 1.1 (capacity retention = 72% after the 1000^{th} cycle) was observed and compared with those at N/P ≥ 1.4 (85–96%). Then, cycling simulation based on the *CE* and F_{dec} of the negative and positive electrodes was applied to observe the potential shifts of LVO and LVP. By focusing on such potential shifts during cycling, we successfully found that the capacity decay of the LVO negative electrode was a factor that promoted the capacity degradation of the LVO//LVP full cells, especially at the low N/P capacity ratio of 1.1. These simulation results were supported by SEM images and the decreased capacity of the cycled LVO negative electrode. Furthermore, the results also indicated that the capacity decay of the LVO negative electrode was caused by an increase in its resistance due to electrolyte decomposition at the LVO negative electrode. The cyclability of the full cells was improved at N/P = 1.1 and by adding 5 wt.% of VC in the electrolyte, demonstrating that the passivation of the LVO negative electrode with the VC-derived film was effective in preventing electrolyte decomposition at the LVO negative electrode. Thus, the capacity decay of LVO was mitigated, validating the predictive capability of our simple simulation method. Although further verifications are certainly required, we believe that this simple simulation method can be applied to other full cell systems with combinations of different types of electrode materials and electrolyte compositions (*e.g.*, Li^+, Na^+, K^+, Mg^{2+}, Ca^{2+}, Al^{3+}). Furthermore, this simulation method may aid in reducing

the cost of time and resources for related studies.

4.5 References

1. Endo, M.; Takeda, T.; Kim, Y.; Koshiba, K.; Ishii, K., High power electric double layer capacitor (EDLC's); from operating principle to pore size control in advanced activated carbons. *Carbon science* **2001,** *1* (3-4), 117-128.
2. Fang, B.; Binder, L., A novel carbon electrode material for highly improved EDLC performance. *The Journal of Physical Chemistry B* **2006,** *110* (15), 7877-7882.
3. Naoi, K., 'Nanohybrid capacitor': the next generation electrochemical capacitors. *Fuel cells* **2010,** *10* (5), 825-833.
4. Augustyn, V.; Simon, P.; Dunn, B., Pseudocapacitive oxide materials for high-rate electrochemical energy storage. *Energy & Environmental Science* **2014,** *7* (5), 1597-1614.
5. Amatucci, G. G.; Badway, F.; Du Pasquier, A.; Zheng, T., An asymmetric hybrid nonaqueous energy storage cell. *Journal of The Electrochemical Society* **2001,** *148* (8), A930-A939.
6. Okita, N.; Iwama, E.; Naoi, K., Recent Advances in Supercapacitors: Ultrafast Materials Make Innovations. *Electrochemistry* **2020,** *88* (3), 83-87.
7. Li, H.; Liu, X.; Zhai, T.; Li, D.; Zhou, H., Li3VO4: a promising insertion anode material for lithium-ion batteries. *Advanced Energy Materials* **2013,** *3* (4), 428-432.
8. Iwama, E.; Kawabata, N.; Nishio, N.; Kisu, K.; Miyamoto, J.; Naoi, W.; Rozier, P.; Simon, P.; Naoi, K., Enhanced electrochemical performance of ultracentrifugation-derived nc-Li_3VO_4/MWCNT composites for hybrid supercapacitors. *ACS nano* **2016,** *10* (5), 5398-5404.
9. Shen, L.; Chen, S.; Maier, J.; Yu, Y., Carbon-Coated Li_3VO_4 Spheres as Constituents of an Advanced Anode Material for High-Rate Long-Life Lithium-Ion Batteries. *Advanced Materials* **2017,** *29* (33), 1701571.
10. Qiao, Y.; Tu, J.; Wang, X.; Zhang, D.; Xiang, J.; Mai, Y.; Gu, C., Synthesis and improved electrochemical performances of porous $Li_3V_2(PO_4)_3$/C spheres as cathode material for lithium-ion batteries. *Journal of Power Sources* **2011,** *196* (18), 7715-7720.
11. Membreño, N.; Park, K.; Goodenough, J. B.; Stevenson, K. J., Electrode/electrolyte interface of composite α-$Li_3V_2(PO_4)_3$ cathodes in a nonaqueous electrolyte for lithium ion batteries and the role of the carbon additive. *Chemistry of Materials* **2015,** *27* (9), 3332-3340.

12. Naoi, K.; Kisu, K.; Iwama, E.; Sato, Y.; Shinoda, M.; Okita, N.; Naoi, W., Ultrafast cathode characteristics of nanocrystalline- $Li_3V_2(PO_4)_3$/carbon nanofiber composites. *Journal of The Electrochemical Society* **2015,** *162* (6), A827.
13. Saıdi, M.; Barker, J.; Huang, H.; Swoyer, J.; Adamson, G., Electrochemical properties of lithium vanadium phosphate as a cathode material for lithium-ion batteries. *Electrochemical and Solid State Letters* **2002,** *5* (7), A149.
14. Yamada, A.; Chung, S.-C.; Hinokuma, K., Optimized $LiFePO_4$ for lithium battery cathodes. *Journal of The Electrochemical Society* **2001,** *148* (3), A224.
15. Wang, X.; Qin, B.; Sui, D.; Sun, Z.; Zhou, Y.; Zhang, H.; Chen, Y., Facile Synthesis of Carbon‐Coated Li_3VO_4 Anode Material and its Application in Full Cells. *Energy Technology* **2018,** *6* (10), 2074-2081.
16. Rui, X.; Sim, D.; Wong, K.; Zhu, J.; Liu, W.; Xu, C.; Tan, H.; Xiao, N.; Hng, H. H.; Lim, T. M., $Li_3V_2(PO_4)_3$ nanocrystals embedded in a nanoporous carbon matrix supported on reduced graphene oxide sheets: Binder-free and high rate cathode material for lithium-ion batteries. *Journal of Power Sources* **2012,** *214*, 171-177.
17. Zhang, L.; Xiang, H.; Li, Z.; Wang, H., Porous $Li_3V_2(PO_4)_3$/C cathode with extremely high-rate capacity prepared by a sol–gel-combustion method for fast charging and discharging. *Journal of Power Sources* **2012,** *203*, 121-125.
18. Wang, C.; Shen, W.; Liu, H., Nitrogen-doped carbon coated $Li_3V_2(PO_4)_3$ derived from a facile in situ fabrication strategy with ultrahigh-rate stable performance for lithium-ion storage. *New Journal of Chemistry* **2014,** *38* (1), 430-436.
19. Okita, N.; Iwama, E.; Tatsumi, S.; VÕ, T. N. H.; Naoi, W.; Reid, M. T. H.; Naoi, K., Prolonged Cycle Life for $Li_4Ti_5O_{12}$//[$Li_3V_2(PO_4)_3$/Multiwalled Carbon Nanotubes] Full Cell Configuration *via* Electrochemical Preconditioning. *Electrochemistry* **2019,** *87* (3), 148-155.
20. Aktekin, B.; Lacey, M. J.; Nordh, T.; Younesi, R.; Tengstedt, C.; Zipprich, W.; Brandell, D.; Edström, K., Understanding the Capacity Loss in $LiNi_{0.5}Mn_{1.5}O_4$–$Li_4Ti_5O_{12}$ Lithium-Ion Cells at Ambient and Elevated Temperatures. *The Journal of Physical Chemistry C* **2018,** *122* (21), 11234-11248.
21. Birkl, C. R.; Roberts, M. R.; McTurk, E.; Bruce, P. G.; Howey, D. A., Degradation diagnostics for lithium ion cells. *Journal of Power Sources* **2017,** *341*, 373-386.
22. Wang, L.; Xu, J.; Wang, C.; Cui, X.; Li, J.; Zhou, Y.-N., A better understanding of the capacity fading mechanisms of $Li_3V_2(PO_4)_3$. *RSC Advances* **2015,** *5* (88), 71684-71691.

23. Yin, S.-C.; Grondey, H.; Strobel, P.; Anne, M.; Nazar, L. F., Electrochemical property: structure relationships in monoclinic $Li_{3-y}V_2(PO_4)_3$. *Journal of the American Chemical Society* **2003,** *125* (34), 10402-10411.
24. Chen, L.; Wang, K.; Xie, X.; Xie, J., Effect of vinylene carbonate (VC) as electrolyte additive on electrochemical performance of Si film anode for lithium ion batteries. *Journal of Power Sources* **2007,** *174* (2), 538-543.
25. El Ouatani, L.; Dedryvère, R.; Siret, C.; Biensan, P.; Reynaud, S.; Iratçabal, P.; Gonbeau, D., The effect of vinylene carbonate additive on surface film formation on both electrodes in Li-ion batteries. *Journal of The Electrochemical Society* **2008,** *156* (2), A103.
26. Ota, H.; Sakata, Y.; Inoue, A.; Yamaguchi, S., Analysis of vinylene carbonate derived SEI layers on graphite anode. *Journal of The Electrochemical Society* **2004,** *151* (10), A1659.

Section 5. General conclusions

This thesis was focused on $Li_4Ti_5O_{12}$ (LTO)//activated carbon (AC) hybrid capacitors with LTO negative and AC positive electrodes as the second-generation capacitor and Li_3VO_4 (LVO)//$Li_3V_2(PO_4)_3$ (LVP) SuperRedox Capacitors (SRCs) with LVO negative electrode and LVP positive electrode as the third-generation capacitor. The aim was to improve the energy density and cyclability of these capacitors through the development of electrolytes.

In Section 1, two strategies for increasing the energy density of electrochemical capacitors, namely, higher voltage and higher energy density, were discussed along with the previous studies on the material and configuration of next-generation capacitors.

In Section 2, the energy density of thick LTO//AC hybrid capacitors (600 μm) was improved *via* high ionic conductivity electrolytes. The utilization of dual-cation electrolytes constructed with a Li-based electrolyte ($LiBF_4$) and an additional supporting electrolyte (quaternary ammonium salts or ionic liquids) was found to be a promising strategy toward simultaneously achieving thick-electrode (> 100 μm) lithium-based energy storage devices with high power and high energy densities. In partculary, 1-ethyl-3-methylimidazolium (EMI) tetrafluoroborate was suitable for the dual-cation electrolyte in an LTO//AC hybrid capacitor, showing 64% capacity retention at a high current density of 200 mA cm^{-2}. The EMI-based dual-cation system exhibited the highest ionic conductivity and output characteristics compared to other dual-cation systems even with lowered Li^+ transport in the bulk electrolyte. It was also demonstrated that the minimum σ_{Li+} (> 0.5 mS cm^{-1}) in dual-cation electrolytes is another important factor to assure the electrochemical performances in thick-electrode LTO//AC systems. These findings may avail a guideline for the design of high-energy-density Li-based energy storage devices

employing thick electrodes without sacrificing the power density and clarified the benefit of increasing the total ionic conductivity rather than improving only the acceleration of lithium ion diffusion.

In Section 3, the energy density was improved *via* high-voltage operation (3.2 V~) LTO//AC hybrid capacitors using dual-cation electrolytes. H_2 gas generation with associated swelling using LTO-based hybrid capacitors upon high-voltage operation over 3.2 V has been a major problem owing to catalytic reductive decomposition of solvent such as propylene carbonate (PC) and H_2O at the Lewis acid sites on the LTO surface. A method to suppress gassing behavior were achieved by adding spiro(1,1')-bipyrrolidinium tetrafluoroborate ($SBPBF_4$) to the lithium-based electrolyte [1 M lithium tetrafluoroborate ($LiBF_4$) in PC]. The dual-cation (Li^+/SBP^+) electrolyte, which has previously been reported as the electrolyte composition used for rate-capability enhancement, reduced the volume of generated H_2 to almost half of that generated using the single-cation (Li^+) electrolyte under high-voltage floating conditions (3.5 V, 60 °C). This behavior was attributed to the LTO surface passivated by the Lewis-based layer *via* Hofmann elimination of SBP^+. Dual-cation electrolytes simultaneously solve the problems of gas generation at high output power density and high-voltage operation, making them highly promising new electrolytes for LTO//AC.

In Section 4, long-term cyclability of LVO//LVP full cell was achieved for the new-generation capacitor devices *via* conducting simple cycling simulation method to predict the degradation factors and optimizing the electrolyte compositions. LVO//LVP full cell was found to be promising devices for high power and high cyclability as a result of these characteristics of the LVO negative electrode and LVP positive electrode. However, constructed LVO//LVP full cells exhibited a capacity decay over 1000 cycles at 50 °C

(72%) owing to a large state of charge shift. The cycling simulation based on the coulombic efficiency and capacity decay of the negative electrode and positive was applied to see the potential shifts of LVO and LVP. By focusing on such potential shifts during cycling, I successfully found out that the capacity decay of LVO negative electrode was a factor promoting the capacity degradation of LVO//LVP full cells. The cyclability improvement of full cells by adding 5 wt.% of vinylene carbonate (VC) in the electrolyte demonstrated that the passivation of LVO negative electrode with the VC-derived film was effective to prevent the electrolyte decomposition at LVO negative electrode and thus to mitigate the capacity decay of LVO, showing the credibility of prediction through developed simple simulation method.

In conclusion, this study's findings show that dual-cation electrolytes, which consisted of Li-salt and additional supporting electrolytes, were promising electrolyte systems for next-generation capacitors due to high power, cyclability, and safety, etc. Moreover, developed charge-discharge cycling simulation was useful for determining the degradation factor of positive- or negative- electrodes in less effort. Through this simulation and new electrolyte system, the researchers can quickly discover degradation factors and solved poor electric performance by changing electrolyte composition (electric salt, solvent, and additives). In the future, designed electrolyte system and developed simulation are expected to extend other full cell systems with a combination of any kinds of electrode materials and electrolyte compositions (Li^+, Na^+, K^+, Mg^{2+}, Ca^{2+}, Al^{3+}, etc.), and may aid to reduce the cost of time and resources for the related research topics.

Reference materials

List of publications

1. Yu Chikaoka, Etsuro Iwama, Tsukasa Ueda, Natsuki Miyashita, Shinici Seto, Masato Sakurai, Wako Naoi, McMahon Thomas Homer Reid, Patrice Simon, and Katsuhiko Naoi "Dual-Cation Electrolytes for High-Power and High-Energy LTO//AC Hybrid Capacitors", *Journal of Physical Chemistry C*, *124* (**2020**) 12230.
2. Yu Chikaoka, Etsuro Iwama, Shinichi Seto, Yuta Okuno, Tomohide Shirane, Tsukasa Ueda, Wako Naoi, McMahon Thomas Homer Reid, and Katsuhiko Naoi "Dual-Cation Electrolytes for Low H_2 Gas Generation in $Li_4Ti_5O_{12}$//AC Hybrid Capacitor System", *Electrochimica Acta*, *368* (**2021**), 137619.
3. Yu Chikaoka, Reiko Okuda, Etsuro Iwama, Masafumi Kuwao, Wako Naoi, and Katsuhiko Naoi "Strategy for Cyclability Prolongation of Li_3VO_4//$Li_3V_2(PO_4)_3$ Full Cells Based on Charge-Discharge Cycling Simulation", *Electrochemistry*, *89* (**2021**), 204.

List of publication (reference)

4. Yu Chikaoka, Etsuro Iwama, Masato Sakurai, Tsukasa Ueda, Tomohide Shirane, Wako Naoi, and Katsuhiko Naoi "Impact of Total Ionic- and Individual Li^+-Conduction in Dual-Cation Electrolytes on Power Performances for Thick Electrode $Li_4Ti_5O_{12}$//AC Hybrid Capacitors", *Journal of Physical Chemistry C*, accepted (Mar. 3, 2021).

Presentation list of international conferences

1. Yu Chikaoka, Etsuro Iwama, Masato Sakurai, Tsukasa Ueda, Wako Naoi, Patrice Simon and Katsuhiko Naoi, "Dual-Cation Electrolyte System Using Quaternary Ammonium Salts and Ionic Liquid for High Power and High Energy $Li_4Ti_5O_{12}$//AC Hybrid Capacitor System" *Pacific Rim Meeting on Electrochemical and Solid-State Science 2020*, Online, A03-0643, Oct. **2020**.
2. Yu Chikaoka, Tomohide Shirane, Yuta Okuno, Tsukasa Ueda, Etsuro Iwama, Wako Naoi, and Katsuhiko Naoi "Dual-Cation Electrolytes for Low Gas Generation of $Li_4Ti_5O_{12}$//AC Hybrid Capacitor system", *6th International Conference on Advanced Capacitors*, Ueda (JAPAN), P-18, Sep. **2019**.
3. Yu Chikaoka, Yuta Okuno, Tsukasa Ueda, Etsuro Iwama, Wako Naoi, and Katsuhiko. Naoi, "Mass Transfer Parameters of DualCation Electrolyte for High Power $Li_4Ti_5O_{12}$ / AC Hybrid Capacitor System", *International Symposium on Enhanced Electrochemical Capacitors*, Nantes (France), P22, May **2019**.

4. Yu Chikaoka, Tomohide Shirane, Yuta Okuno, Tsukasa Ueda, Etsuro Iwama, Wako Naoi, and Katsuhiko. Naoi, “Mass Transfer Parameters and Ionic Association of Dual-Cation Electrolyte for Hybrid Capacitor System”, *First International Conference on 4D Materials and Systems*, Yonezawa (JAPAN), M04-0253, Aug. **2018**.

List of awards

1. 近岡 優, 電気化学会第 87 回大会, 優秀学生発表賞, 2020 年 3 月.
2. Yu Chikaoka, *6th International Conference on Advanced Capacitors “Student Poster Award*”, 2019 年 9 月.

Presentation list of Japanese conferences

1. 近岡 優, 奥野雄太, 櫻井雅人, 上田 司, 岩間悦郎, 直井和子, 直井勝彦「ハイブリッドキャパシタ用デュアルカチオン電解液による H_2 ガス発生抑制メカニズムの解析」, 電気化学会第 87 回大会, 1L10, 名古屋, 2020 年 3 月 (Web 討論)
2. 近岡 優, 奥野雄太, 櫻井雅人, 上田 司, 岩間悦郎, 直井和子, 直井勝彦「LTO//AC ハイブリッドキャパシタ用デュアルカチオン電解液における物質輸送パラメータ解析」, 第 60 回電池討論会, 2H03, 京都, 2019 年 11 月（口頭発表）
3. 近岡 優, 奥野雄太, 上田 司, 岩間悦郎, 直井和子, 直井勝彦「ハイブリッドキャパシタ用デュアルカチオン電解液による $Li_4Ti_5O_{12}$ 負極反応の物質輸送パラメータ解析析」, 電気化学会第 86 回大会, 1I08, 京都, 2019 年 3 月（口頭発表）
4. 近岡 優, 白根朋英, 奥野雄太, 上田 司, 岩間悦郎, 直井和子, 直井勝彦「PGSE-NMR を用いたハイブリッドキャパシタ用デュアルカチオン電解液のイオン輸送挙動解析」, 第 8 回 CSJ 化学フェスタ 2018, P4-105, 東京, 2018 年 10 月（ポスター発表）
5. 近岡 優, 白根朋英, 上田 司, 岩間悦郎, 直井和子, 直井勝彦「ハイブリッドキャパシタ用デュアルカチオン電解液による $Li_4Ti_5O_{12}$ 負極反応の高速化メカニズム解析」, 電気化学会第 85 回大会, 1T16, 東京, 2018 年 3 月（口頭発表）

Acknowledgments

I am deeply grateful to Prof. Katsuhiko Naoi for useful suggestions and discussions on this study. Prof. Katsuhiko Naoi gives insightful comments and advice on all papers and presentations. I would like to thank to Prof. Takashi Yamazaki, Prof. Yoshinao Kumagai, Prof. Nobuhumi Nakamura, Prof. Etsuro Iwama, and visit Prof. Kenji Tamamitsu in the Department of Applied Chemistry at the Tokyo University of Agriculture and Technology for reviewing my dissertation. I also thank Ms. Wako Naoi (K&W Inc.) for SEM observation and life supports, Prof. Etsuro Iwama for a lot of discussions, teaching experiments and theories, Assistant Prof. Junichi Miyamoto for useful discussions and experimental support, and Ms. Yuki Nagano for grateful mental support and detailed check my all papers and presentation from Naoi Laboratory in the Tokyo University of Agriculture and Technology. For visiting professor, I am thankful to Prof. Patrice Simon (Université Paul Sabatier in France) for tremendously useful discussion and teaching logical configuration of my paper and Dr. McMahon Thomas Homer Reid (Simpetus LLC.) for teaching English writing.

I am grateful to the following laboratory members for outstanding contributions: in the electrolyte team members, Mr. Natsuki Miyashita, Mr. Shinichi Seto, Mr. Tomohide Shirane, Mr. Yuta Okuno, Mr. Masato Sakurai, Mr. Takaaki Ariga, and Mr. Shogo Matsuoka; in the Full cell team members, Mr. Masafumi Kuwao, Ms. Reiko Okuda, and Mr. Taiga Hashimoto. Special thanks to my family for life support. Finally, I am very grateful to all people who I have met.

November 17. Yu Chikaoka